SUPERCONDUCTIVTY IN REDUCED DIMENSIONS

A DISSERTATION
SUBMITTED TO THE DEPARTMENT OF PHYSICS
AND THE COMMITTEE ON GRADUATE STUDIES
OF STANFORD UNIVERSITY
IN PARTIAL FULFILLMENT OF THE REQUIREMENTS
FOR THE DEGREE OF
DOCTOR OF PHILOSOPHY

Julie A. Bert
July 2012

This dissertation is online at: http://purl.stanford.edu/yn530ff0275

I certify that I have read this dissertation and that, in my opinion, it is fully adequate in scope and quality as a dissertation for the degree of Doctor of Philosophy.

Kathryn Moler, Primary Adviser

I certify that I have read this dissertation and that, in my opinion, it is fully adequate in scope and quality as a dissertation for the degree of Doctor of Philosophy.

Harold Hwang

I certify that I have read this dissertation and that, in my opinion, it is fully adequate in scope and quality as a dissertation for the degree of Doctor of Philosophy.

Steven Kivelson

Approved for the Stanford University Committee on Graduate Studies.

Patricia J. Gumport, Vice Provost Graduate Education

This signature page was generated electronically upon submission of this dissertation in electronic format. An original signed hard copy of the signature page is on file in University Archives.

Abstract

This thesis covers three different superconducting systems. One dimensional aluminum rings, and two dimensional heterostructures of $LaAlO_3/SrTiO_3$ and δ-doped $SrTiO_3$. In all cases we studied the magnetic response of these superconductors using a scanning SQUID microscope.

In our study of 1D aluminum rings, we monitor the magnetic response of the persistent supercurrent to explore the impact of of phase fluctuations on the ring's ability to screen magnetic fields. The physical parameters of the rings were designed to reduce the superconducting phase stiffness. We observe a suppression of the susceptibility signal below the critical temperature, which we attribute to a thermodynamic sampling of metastable states with different phase winding number, termed fluxoid fluctuations. We find our data is well described by a simple theoretic model which accounts for a thermodynamic sampling of fluxoid states.

The next part of the thesis discusses two dimensional superconductors at the interface of complex oxides. In $LaAlO_3/SrTiO_3$, we discovered nanoscale patches of magnetism coexisting with inhomogeneous superconductivity. We analyze the magnetic field from the magnetic patches and find it is not large enough to be responsible for the inhomogeneity observed in the superconductivity. Instead, we found that a landscape of isolated paramagnetic spins is the driving source of the inhomogeneity. The gate tunable nature of the LAO/STO interface provides an additional avenue for studying the superconductivity. Our measurements of the temperature dependence of the superfluid density, taken at different gate voltages, collapse to a single curve characteristic of a full superconducting gap. This indicates that superconductivity

in this exotic system may be conventional in nature. Finally, we measured the temperature dependence of the superfluid density of δ-doped STO using two different techniques and show that it is also a conventional superconductor.

Acknowledgements

This thesis, like so many others, is a mishmash of topics that follows the twists and turns encountered over the course of six years in an experimental physics lab. In retrospect I found a consistent theme for the work I've done under the title *Superconductivity in reduced dimensions*, but this cohesiveness is more of the result of a happy accident than any purposeful plan. Yet, I've come to believe that it is the lack of a clear path that separates the experience of graduate school form most other endeavors in life. This lack of direction can cause unending months and sometimes years of frustration, but it also creates the freedom that leaves us open to make new discoveries.

I am very grateful to Kam for providing me with the opportunity to discover my own path through graduate school. These past six years have not always been easy, but they have helped me grow into a self-confident researcher with the courage to pursue my own ideas. Throughout grad school Kam would rarely ask me to study any specific problem or system. Instead she often would discuss problems she thought I might find interesting, leaving me to decide my own scientific path. It was one of these casual discussions that, eventually, led to my discovery of coexisting superconductivity and magnetism in LAO/STO. This work was the highlight of my graduate career and I am even more proud of it because it was originally my decision to study complex oxide systems.

I also owe a great degree of gratitude to the students and post-docs who came before me and spent countless hours teaching me the skills necessary to be an experimental physicist.

Hendrik Bluhm and Nick Koshnick passed Dilford, the dilfridge, on to me. They taught me the subtle secrets to running a dilfridge and scanning SQUID, as well as best practices for taking and analysing data. Although, Hendrik left the lab only a year after I joined his continued leadership in the low temperature physics community has been a ongoing source of support. Nick helped get me started on my first independent dilfridge measurement run. He fabricated the aluminum rings sample discussed in chapter 2 and did much of the theory work.

I faced a difficult challenge in my third year. Just as Nick was preparing to graduate the dilution refrigerator stopped behaving normally. It turned out there was oil in the mixing chamber. I disassembled, cleaned and reassembled the dilution unit. It was the first task I did as the new owner of the system. Throughout the process I got invaluable, help, advice, support, and commiseration from Ophir Auslaender and Sami Amasha. Sami runs the dilution refrigerator in the DGG group and Ophir ran a dilution refrigerator during his PhD work. After 4 years running one myself, I know all current and former dilfridge users share a special bond.

After the rings experiment I began work on the complex oxides. For this project I own a great deal of gratitude to the Hwang group, including Harold himself, who have all been wonderful collaborators. I especially want to thank Chris Bell and Minu Kim who made the first set of samples and shared them with me at the March Meeting in Portland. I also need to thank Beena Kalisky. She has studied every possible material that has come into our lab, and the complex oxides were no exception. It has been wonderful to have another member of the Moler lab, who was as intimately engaged in measuring the complex oxides as I was. By measuring in tandem on the 4K system and dilfridge we achieved significantly more that either of us could alone and really made a name for our group in the oxide community.

I couldn't have asked for a better community than I found in the Moler group. Tom Lippman and Lisa Qian have been in the group almost as long I have, and it's been wonderful making this journey with them. Lan Luan, Cliff Hicks, Hanshen Zhang, Katja Nowack, Ilya Sochnikov, Eric Spanton, Hilary Noad and Phil Kratz represent both the past and future of the Moler group. Andre Garcia, Daniel Harlow,

Katherine Luna, and Xiaowei Yu have been terrific friends in the greater physics community. It has been wonderful teaching and learning from all of you.

Finally, I want to thank my parents for their encouragement and support and for instilling in me a love of learning that I will carry throughout my life. And to Greg, for being there though every part of this journey. I truly believe I could not have made it to where I am today without his constant love and support.

Contents

List of Tables

List of Figures

Part I

Introduction

Chapter 1

Introduction

1.1 Superconductivity overview

This thesis covers superconductivity in many forms. We start with conventional superconductors in patterned structures and move on to examine superconducting states in oxide materials. In addition, all of the measurements presented in this thesis have been made with a superconducting sensor. Consequently it is natural to begin with an overview of the basic properties of superconductors.

Superconductivity is a phase of matter that is physically different from normal conductors. In a superconductor, at the critical temperature, electrons undergo a thermodynamic phase transition. This transition is accompanied by an abrupt change in physical properties. Most notably the resistance drops to zero.

In a normal metal resistance is caused by collisions between electrons and the crystal environment. This includes collisions with the lattice, impurities, and other electrons. In superconductors an attractive interaction, called the pairing mechanism, causes electrons to form pairs. The energy spectrum of the pairs has a gap. This means that adding a small amount of energy will not break the pairs into two separate electrons. Below the critical temperature, the pairing gap becomes larger than the temperature and the pairs are not scattered. The resistance is precisely zero and the pairs from a macroscopic quantum state with a single phase.

In addition to zero resistance a second defining characteristic of superconductivity is the Meissner effect. The Meissner effect describes a superconductor's ability to expel an applied magnetic field. In fact, a superconductor cooled in an equilibrium field will spontaneously expel that field at temperatures below its critical temperature. This property distinguishes superconductivity from a simple zero resistance state. Following Lenz's law, a material with zero resistance will expel an applied magnetic field because it can generate eddy screening currents that will not decay. However, a resistive metal in an equilibrium field will not spontaneously expel that field if the resistance suddenly disappeared, whereas a superconductor naturally does. The SQUID sensors used to make the measurements that are presented in this thesis use the Meissner effect to study superconductors. The SQUID applies a local magnetic field to the superconducting sample and is sensitive to the Meissner screening currents generated by the superconductor. The magnetic field does not instantaneously drop to zero in a superconductor but decays over a characteristic length scale called the magnetic penetration depth, λ. The screening currents flow in a region within λ of the surface.

A third attribute of superconductivity is quantization of magnetic flux. All the electrons in a superconductor form a single macroscopic quantum wave function that can be described by a complex number, $\psi = Ae^{(i\phi)}$, represented by an amplitude, A, and phase, ϕ. The phase must be single valued at any position in the superconductor. If we imagine a superconductor penetrated by a magnetic field, and we navigate about a path that encloses magnetic flux lines then the superconducting phase will wind. When we return to the starting point the phase must be the same. This is only possible if the phase wound by an integer multiple of 2π. Consequently the flux that penetrates a superconductor must be quantized to keep the phase single valued. Moreover, the complex number ψ, also known as the Ginzburg-Landau order parameters, is related to the cooper pair density, $|\psi|^2 = n_s$. We can now introduce the coherence length, ξ as the distance over which ψ can vary without an excess increase in energy [104].

The quantized flux bundles that penetrate a superconductor are called vortices.

Vortices occur in superconductors where $\xi < \lambda$, known as type II superconductors. In a type II superconductor, if we navigate about a path and the phase change is zero then our path enclosed only superconducting material. If the phase change is 2π then there was a single vortex enclosed in the path.

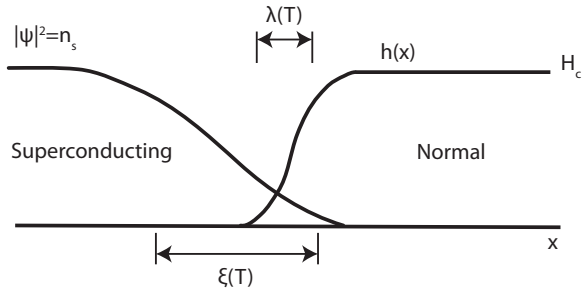

Figure 1.1: Interface between superconducting and normal domains in a type I superconductor. The superconducting order parameter, ψ decays on a length scale ξ in contact with a normal region. An applied magnetic field H_c decays on a length scale λ in the superconductor. From Tinkham [104].

To summarize, the most well know property of superconductors is their lack of electrical resistance. However, they are more complex than resistance free metals. Specifically, the superconductor's interaction with magnetic fields including the Meissner effect and flux quantization are properties not found in a hypothetical resistance free metal. Moreover a superconductor's special sensitivity to magnetic fields means that magnetic fields are an effective tool for studying superconductors and understanding their properties.

1.2 Reduced dimensions

This thesis covers measurements on two different superconducting systems: mesoscopic aluminum rings (Part 2) and the superconducting complex oxide heterostructures including the interface between $LaAlO_3$ and $SrTiO_3$ (LAO/STO) and Nb doped $SrTiO_3$ (Part 3).

In a superconducting system the relevant length scale is the coherence length ξ.

Reduced dimensional structure have a spatial extent that is smaller than ξ in at least one dimension. In rings both cross-sectional dimensions (width and thickness) are small compared to ξ. Rings are one dimensional objects that extend only along their circumference. The LAO/STO interface extends in two dimension with just the thickness being small compared to ξ.

1.2.1 One dimension: Destruction of long range order

At first glance measuring superconductivity in reduced dimensional structures may seem to be a contradiction. The long range order that is required to support a macroscopic phase ordered state (i.e. superconductivity) cannot exist in fewer than three dimensions [90].

A general theorem states that in any 1D system with short range forces there cannot be a phase ordered state at finite temperature [63]. In 1D the free energy can always be lowered by breaking the phase coherence of a long section into multiple sections of alternating phases [90].

As described in the previous section, a superconducting state can be described by an order parameter with a well defined amplitude and phase. However, Rice showed that thermodynamic fluctuations of the phase will destroy long range order in both 1D and 2D superconducting systems [90].

We may have to give up on perfect phase coherence in 1D, but is a persistent supercurrent still possible in 1D rings? Little found that in any system where the interaction force between electrons is finite an infinitely sharp resistive transition is only possible in three or more dimensions [67]. In 1D systems at finite temperatures the resistance is never absolutely zero, but at the critical temperature the resistance will still drop to a small fraction of the normal resistance.

The source of this small yet finite resistance in 1D rings is thermodynamic phase fluctuations, called phase slips. A phase slip will temporarily drive the order parameter to zero in order to transition between states with different phase winding number. See Fig. 1.2. During the phase slip, superconductivity is briefly suppressed in a section of the ring of length ξ, and subsequently recovers. Consequently we can

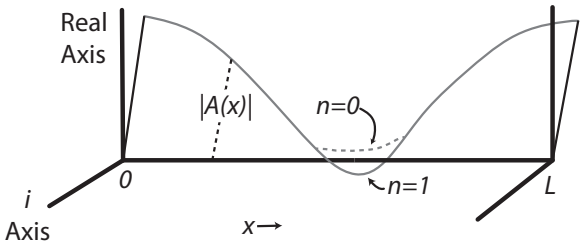

Figure 1.2: The evolution of the complex order parameter, shown in gray, in a 1D ring of length L. At 0 and L the order parameter is the same. However, in the $n = 1$ case the phase traveled a distance of 2π and in the $n = 0$ case the phase change was zero. To travel between these two states the amplitude A must go through zero. This destroys superconductivity in a section of the ring of length ξ, and is the cause of the finite resistance state in 1D rings. From Little [67].

still measure a persistent current in 1D superconducting rings, but the presence of thermodynamic fluctuations will cause it to decay over time. These fluctuations and their impact on superconductivity in rings will be discussed in detail in part II of this thesis.

1.2.2 Two dimensions: BKT transition

This argument may be extended to two dimensions. A resistive transition should be observed in 2D superconductors, but the presence of fluctuations never allows the resistance to be truly zero. Indeed, the onset of superconductivity in two dimensions is not accompanied by true long-range phase coherence. Instead it is described by a topological phase transition, called a BKT transition [61, 8]. At a specific temperature below the critical temperature, spontaneously formed vortex anti-vortex pairs unbind and delocalize. The unbound vortices contribute to a finite resistance in the superconductor and broaden the resistive transition. The vortex motion also leads to variations in the phase across the sample, destroying phase coherence.

The LAO/STO interface is a superconductor in the 2D limit. At temperatures below the BKT transition the phase of the superconducting state is sufficiently coherent to screen an applied magnetic field. In part III of this thesis we take advantage

of the Meissner effect to study superconductivity and magnetism in this system.

1.3 Making magnetic measurements

The majority of magnetic measurements of superconductors are done using bulk techniques, namely magnetotransport and magnetization. Magnetotransport involves attaching leads to a sample and measuring voltage as a function of the driving current and magnetic field. Bulk magnetization measurements apply a large field to a sample and detect how the sample, as a whole, responds to that field. These measurements are very common in characterizing superconducting samples because they are relatively simple to perform and can quickly diagnose growth problems. Additionally, with careful analysis such measurements can yield significant insight into the material properties. However, both magnetization and transport techniques will mask small scale inhomogeneity in the sample. Moreover, if the sample of interest is patterned on a substrate, bulk magnetization measurement have the added complication of separating the sample's signal from the background signal of the substrate. Finally, both of these techniques lack the magnetic sensitivity to observe very small magnetic features.

The Moler group has worked for years to develop ultra sensitive magnetic probes which we mount in micro-positioning assemblies to make local measurements across a large area of a sample. All the work in this thesis was done with a SQUID probe. SQUID stands for Superconducting QUantum Interference Device, and it is also the sensor used in bulk magnetometry measurements. Our SQUIDs have been specially designed and optimized to increase their spatial resolution and magnetic flux sensitivity [44].

A basic SQUID consists of a superconducting loop interrupted by two weak links (Josephson junctions), shown schematically in Fig 1.3a. A SQUID, driven above it's critical current, is a flux-voltage transducer. The voltage drop across the SQUID is

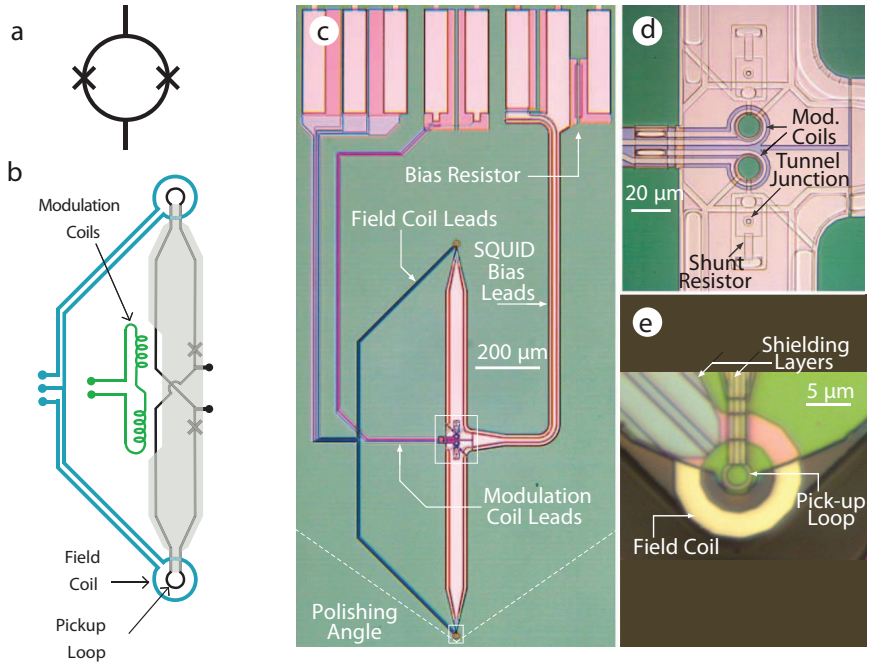

Figure 1.3: a) Schematic of a basic SQUID. b) Modified SQUID for use in a scanner. c) Optical image of the SQUIDs designed in the Moler group and used in this thesis. d) Close up of the modulation coils used for feedback. e) Close up of the pick-up loop and field coil. This is the part of the SQUID that will brought closest to the sample.

directly proportional to the flux that passes through the SQUID. We use a counter-wound gradiometric SQUID design (Fig 1.3b). A background field applied to a gradiometric SQUID results in zero net flux. Additionally we use superconducting shields to screen the SQUID. Only a 3 μm loop, the pick-up loop, remains unshielded. The pick-up loop is the sensitive area of the scanner. As shown in Fig 1.3c and Fig 1.4 we polish away the substrate near the pick-up loop so that it can be brought in contact with a sample.

Concentric with the pick-up loop in the SQUID tip is a single turn field coil. Driving a current in this coil creates a local magnetic field. The pick-up loop can then record the sample's susceptibility response to the locally applied field. If we make the susceptibility measurement in a lock-in configuration, by driving an AC current in

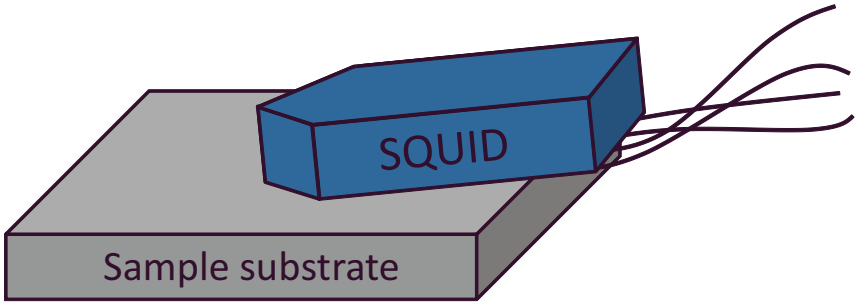

Figure 1.4: Cartoon of a SQUID brought near a sample.

the field coil, we can simultaneously measure the AC-susceptibility response (lock-in signal) and the DC-magnetometry response (low-pass filter).

The sensor is mounted on a piezo-resistive scanner [17]. Two pairs of s-benders allow the SQUID to move in an constant plane, while a cantilever piezo brings the sensor into and out of contact with the sample. This configuration results in a fine scan range of about 200 μm. The piezo scanner is mounted on a three axis stack of coarse positioners. Each positioner has a range of about 5 mm.

The scanner itself is rigidly mounted through a copper cage to the mixing chamber of a dilution refrigerator. The base temperature of the dilution refrigerator is 17 mK. When the z-cantilever piezo is moving the base temperature is 30 mK, and when the x-y s-bender stage is moving the base temperature is elevated further. The exact temperature depends on the size of the scan range with larger scan ranges resulting in higher temperatures. Such a set-up allows us to make spatially resolved magnetic measurements of superconductors with very low critical temperatures.

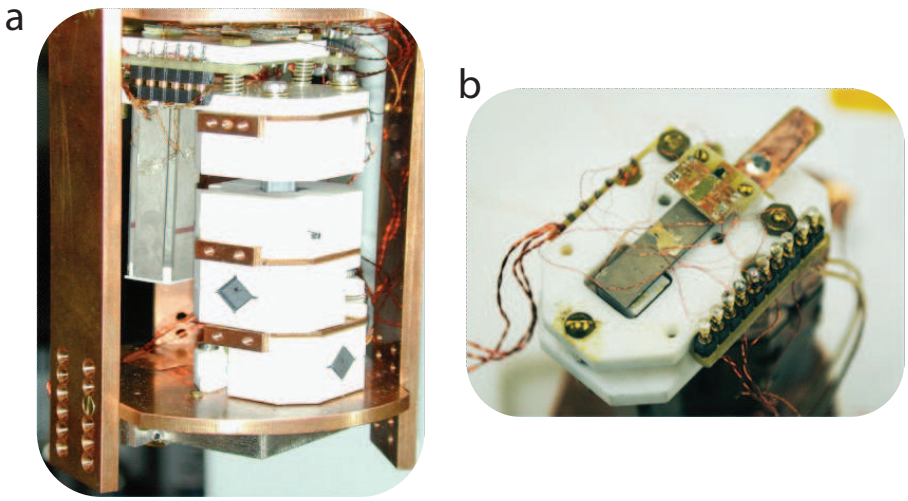

Figure 1.5: a) The piezo scanner mounted on the stack of coarse positioners. b) Close-up of polished SQUID mounted on the z-cantilever piezo.

Part II

Superconductivity in one dimension

Chapter 2

Fluxoid fluctuations

Julie A. Bert, Nicholas C. Koshnick, Hendrik Bluhm and Kathryn A. Moler "Fluxoid fluctuations in mesoscopic superconducting rings" *Physical Review B* **84** 134523 (2011).

2.1 Abstract

Superconducting rings are an ideal system for studying phase coherence in one dimension. We study the temperature dependence of the magnetic susceptibility of superconducting rings with a scanning superconducting quantum interference device (SQUID). The physical parameters of the rings were designed to reduce the superconducting phase stiffness. We observe a suppression of the susceptibility signal below the critical temperature, which we attribute to a thermodynamic sampling of metastable states with different phase winding number, termed fluxoid fluctuations [59]. We introduce a simple model [59] for the susceptibility of a ring affected by fluxoid fluctuations and compare it with one dimensional Ginzburg Landau (GL) theory including all thermal fluctuations. We find good agreement between our fluxoid model and the full 1D GL theory up to a shift in the critical temperature. Additionally our magnetic susceptibility data is well described by 1D GL theory.

2.2 Introduction

In this paper, we study the properties of superconducting 1D wires in a model system: uniform isolated aluminum rings. Superconducting rings have states with uniform phase windings that differ by integer multiples of 2π, called fluxoid states. Phase slips allow for transitions between fluxoid states. During a phase slip the order parameter phase loses or gains a twist by suppressing superconductivity in a portion of the ring. Phase slips are detected as jumps in measurable quantities such as the current. In contrast, fluxoid fluctuations represent the thermal occupation of different fluxoid states. Their impact on the ring's current is represented by a thermodynamic sampling of all energetically accessible fluxoid states. By generating a Boltzmann distribution of these fluxoid states, Koshnick formulated a new model [59] which predicts a suppression in the temperature dependence of the ring's zero field magnetic susceptibility. Complementing previous experiments that studied amplitude fluctuations in rings with long mean free paths, [60, 112] we present experimental data from short mean free path rings which exhibit a downturn in the susceptibility close to the critical temperature. Moreover we show our new fluxoid fluctuation model provides a good fit to the susceptibility data. This paper is not intended to be a complete review of superconducting fluctuations in reduced dimensions. We restrict our analysis to thermal fluctuations of the GL order parameter that are described by 1D GL theory. We do not treat quantum fluctuations or Langevin noise and we assume our rings are homogeneous.

Fluctuations play an important role in the superconducting behavior of samples of reduced dimensionality: [99] they can make electron pairing and long-range phase coherence occur at different temperatures in unconventional superconductors, [34] lead to the Berezinskii-Kosterlitz-Thouless transition [61] in two dimensions (2D), cause the destruction of long range phase order in infinitely long one-dimensional (1D) wires [90], and determine the resistive properties of 1D wires of finite length [64, 74, 38, 65].

The nature of superconducting fluctuations in rings has generated significant interest. Fluxoid dynamics in individual rings have been probed as a function of ring size [7, 13, 20], magnetic field [13, 81, 107], and temperature [72, 20, 41]. The occupation of metastable fluxoid states has also been measured to determine a crossover from 1D to 2D behavior in wide rings [76, 23]. Phase slip rates have been studied in both conventional low T_c [112] and unconventional high T_c [55] superconducting rings. Ring inhomogeneities, such as weak links or nonuniform widths, have been studied as phase slip sites that can impact the ring's current-phase relationship and fluxoid transitions [14, 48, 52, 108, 106, 107].

Transport measurements have long been used as a probe of superconducting fluctuations [78, 6]. Transport measures voltage, which is directly related to the phase slip rate. In contrast, we use a scanning SQUID to make a magnetic measurement that is sensitive to the thermodynamic equilibrium current in the ring. Specifically we measure the effects of superconducting fluctuations on the ring's equilibrium supercurrent, I, as a function of applied flux, Φ_a, measured in a temperature range near the critical temperature, T_c. Direct measurements of the ring current as a function of applied flux are useful because they provide access to the thermodynamic free energy through the derivative $I = -\partial F/\partial \Phi_a$. While there are also interesting features in the full flux dependence [60], in this paper we measure the ring's zero field susceptibility as a function of temperature, $dI(T)/d\phi|_{\phi=0}$, where $\phi \equiv \Phi_a/\Phi_0$ and $\Phi_0 \equiv h/2e$ is the superconducting flux quantum.

Theoretical work using Ginzburg-Landau (GL) theory has predicted the current in the presence of an applied flux threading the ring. Ambegaokar and Eckern applied a Gaussian approximation to GL to predict a mesoscopic persistent current driven by superconducting fluctuations above T_c [3, 2]. However, the Gaussian approximation, accurate far above T_c where the quadratic term in the GL free energy dominates, diverges as T approaches T_c. von Oppen and Riedel formulated a transfer matrix approach to GL theory that accounts for all thermal fluctuations to calculate the supercurrent and correct the divergence at T_c [109]. More recently, Schwiete and Oreg proposed a simplification of the full formulation by von Oppen and Riedel

(VOR) that makes an analytic prediction for the ring's susceptibility, $dI/d\Phi_a$, in the limit where the superconducting coherence length is of order the radius [96]. Schwiete and Oreg provide a simple alternative to solving the VOR model numerically. This model is applicable to long mean free path rings with a short circumference, rather than the short mean free path rings with long circumferences discussed in this paper.

A number of different experiments have used current and susceptibility measurements to study fluctuations in individual superconducting rings [112, 19, 20, 60, 48]. Zhang and Price studied the phase slip rate and susceptibility as a function of temperature in a single Al ring [112]. The ring's geometry and long mean free path favored amplitude fluctuations that were expected to support a susceptibility response above T_c. However, the observed susceptibility signal was an order of magnitude larger than predicted by GL theory. Koshnick *et al.* [60] measured the susceptibility of 15 individual rings with long mean free paths as a function of Φ_a. All rings showed a fluctuation induced susceptibility response above T_c, which agreed well with complete 1D GL theory [109].

This paper focuses on rings with shorter mean free paths and longer circumferences, which should exhibit fluxoid fluctuations. Instead of generating an enhancement in the susceptibility above T_c, fluxoid fluctuations can suppress the ring's superconducting response well below T_c. We start in Sec. 2.3.1 by describing the different thermal fluctuations experienced by our rings, and establish the physical conditions that support fluxoid fluctuations. We outline a model [59], derived from the 1D GL free energy functional, where a thermal distribution of fluxoid states suppresses the rings' diamagnetism (Sec. 2.3.3). Our theoretical analysis concludes by comparing our fluxoid model to a complete theory that includes all thermal fluctuations in the GL framework [109] (Sec. 2.3.4). We find good agreement between the models in rings with short mean free paths where fluxoid fluctuations dominate the response. Finally, we discuss our measurement technique in Sec. 2.4 and present data from two sets of ring samples, which are well described by our 1D GL models (Sec. 2.4.3).

2.3 Fluctuation theory

2.3.1 Types of fluctuations

GL theory introduces a complex order parameter, $\psi(\mathbf{r})$, with an associated amplitude and phase. Fluctuations are deviations in ψ from the mean field solutions corresponding to local minima of the GL free energy functional, which affect the order parameter's amplitude or phase. Fluctuations become significant when the thermal energy of the system allows multiple wavefunctions to contribute to the ring's response. When multiple fluxoid states are thermally accessible even at zero applied flux the ring fluctuates between its minimum energy fluxoid state and the metastable fluxoid states, a process we call fluxoid fluctuations. In addition to fluxoid fluctuations, 1D GL theory accounts for fluctuations in the amplitude of the superconducting order parameter, and phase fluctuations that are not uniform around the ring. The main difference between our fluxoid model presented in Sec. 2.3.3 and the full 1D GL theory formulated by Von Oppen and Riedel (Sec. 2.3.4) is the latter includes these amplitude and non-uniform phase fluctuations.

It is important at this point to emphasize the distinction between phase slips and fluxoid fluctuations. Fluxoid fluctuations represent equilibrium phenomena and will not be observable on measurement timescales if the ring is not experiencing phase slips which populate higher phase winding states. The next three sections will lay out and compare the energy scales for the onset of both fluxoid fluctuations and phase slips.

Fluxoid fluctuations

The ring geometry of our samples imposes a constraint on the order parameter phase. The order parameter phase must be single valued modulo 2π, therefore the cylindrical symmetry of the system results in a phase that winds by an integer multiple of 2π around the ring. Each fluxoid state, with free energy F_n and phase winding $2\pi n$, represents a stable local minima of the GL free energy functional.

We start by finding expressions for F_n. One dimensional Ginzburg-Landau theory

introduces the GL free energy functional in the presence of a magnetic field represented by the vector potential $\vec{A}$

$$F[\psi(x)] = \int \left[\alpha|\psi(x)|^2 + \frac{1}{2}\beta|\psi(x)|^4 + \frac{\hbar}{2m^*}\left|\left(\vec{\nabla} - \frac{ie^*\vec{A}}{\hbar}\right)\psi(x)\right|^2\right] d^3x. \tag{2.1}$$

α and β both depend on T, and $\alpha^2/\beta = B_c(T)^2/\mu_0$ is related to the superconducting critical field, $B_c(T)$. e^* and m^* are the charge and mass of the Cooper pairs and μ_0 is the permeability of free space.

We look for stable solutions that locally minimize the Ginzburg Landau free energy functional. In a homogeneous one dimensional ring fluxoid states have free energies

$$F_n(T,\phi) = -F_c(T)\left(1 - \frac{\xi(T)^2}{R^2}(\phi - n)^2\right)^2, \tag{2.2}$$

where the critical field, and the ring volume ($V = 2\pi Rwd$) determine the ring's total condensation energy ($F_c(T) = VB_c(T)^2/2\mu_0$). w is the ring width and d is the thickness. The dependence on $\xi(T)/R$ accounts for the suppression of the superfluid density by the phase gradient around the ring with coherence length $\xi(T)$ and radius R. The applied flux, $\phi = \Phi_a/\Phi_0$, can be transformed into a shift in the boundary conditions for a wave function in a ring [26], and therefore contributes to the energy in the same way as n.

We approximate the energy associated with each fluxoid state by expanding the mean field GL free energy expression, Eq. (2.2), to lowest order in $\xi(T)/R$. The energy difference between the lowest energy fluxoid states at zero applied flux,

$$\begin{aligned} \Delta F_{\pm1,0}(T,\phi=0) &= F_{\pm1}(T,\phi=0) - F_0(T,\phi=0) \\ &\approx 4\pi\xi wd\frac{B_c^2}{2\mu_0}\frac{\xi}{R}, \end{aligned} \tag{2.3}$$

is indicated with a red arrow in Fig (2.1). This energy barrier determines the onset of fluxoid fluctuations in our zero-field susceptibility measurements presented in Sec. 2.4.

Phase slips

A phase slip is the process of changing the fluxoid number by 2π by briefly driving the order parameter amplitude to zero in a coherence-length-sized section of the ring [99]. The phase slip activation energy is found by calculating the lowest energy pathway between two fluxoid states as defined by the energy barrier for the saddle point in wave function configuration space. The saddle point energies, $F_{\rm sn}$, being stationary points of the free energy, must also satisfy the GL equations; however, these solutions represent unstable configurations. We find an approximate condition for the onset of phase slips from calculations of the energy barrier.

Langer and Ambegaokar were the first to use 1D GL theory to calculate the saddle point free energy barrier between fluxoid states in 1D wires where the wire length was much greater than the superconducting coherence length [64]. Zhang modified Langer and Ambegaokar's solution for a ring geometry [111], and found the saddle point energy in rings where $L \gg \xi(T)$.

$$F_{sn}(T,\phi) = F_c(T)\left(\frac{8\sqrt{2\delta(T,\phi,n)}}{3}\frac{\xi(T)}{L} - \frac{(2+\delta(T,\phi,n))^2}{9}\right), \tag{2.4}$$

where $L = 2\pi R$ is the ring's circumference and $\delta(T,\phi,n)$ is the normalized difference between the square of the order parameter amplitudes near and far from a phase slip event. $\delta(T,\phi,n)$ is a real number between 0 and 1 that satisfies the relation

$$2\pi n = \sqrt{\frac{1-\delta}{3}}\frac{L}{\xi(T)} + 2\tan^{-1}\left(\sqrt{\frac{3\delta}{2(1-\delta)}}\right) + 2\pi\phi. \tag{2.5}$$

For $\phi = n + 1/2$, $\delta = 1$.

We are interested in a regime where $L \gg \xi(T)$, and δ remains close to one for moderate n. Using the substitution $\kappa = \sqrt{1-\delta}$ and expanding to lowest order in κ, we arrive at a simplified expression for δ.

$$\delta(T,\phi,n) = 1 - \left(\frac{\sqrt{3}\pi(2n - 2\phi - 1)}{\frac{L}{\xi(T)} - 2\sqrt{2}} \right)^2 \tag{2.6}$$

Extending the $L \gg \xi$ limit allows us to set $\delta \approx 1$. This approximation makes $F_{sn}(T,\phi) = F_{sn}(T)$ independent of flux. We can now calculate the free energy barrier for phase slips as a function of applied flux, $\Delta F_{s\pm1,0}(T,\phi)$, for a ring that starts in the $n = 0$ fluxoid state and transitions to the $n = \pm 1$ state.

$$\begin{aligned} \Delta F_{s\pm1,0}(T,\phi) &= (F_{s\pm1}(T) - F_0(T,\phi)) \\ &\approx \xi w d \frac{B_c^2}{2\mu_0} \left(\frac{8\sqrt{2}}{3} - 4\pi \frac{\xi}{R}\phi^2 \right) \end{aligned} \tag{2.7}$$

This energy barrier depends on the applied flux and is indicated by the gray shaded region in Fig 2.1. In the limit where $L \gg \xi$ the second term in Eq. (2.7) can be ignored, and the energy barrier no longer depends on flux.

Comparison of energy scales

In Fig 1, the energy expressions for the fluxoid states, Eq. (2.2) blue solid line, and the saddle point states, Eq. (2.4) green dashed line, for two rings with different L/ξ are plotted as a function of flux and fluxoid number n. The solid red arrow indicates the energy barrier for fluxoid fluctuations at $\phi = 0$, Eq. (2.3). It is the energy difference between consecutive fluxoid states. The shaded area shows the flux dependent energy barrier for phase slips between the $n = 0$ and the $n = \pm 1$ fluxoid states, Eq. (2.7). This is the energy difference between the fluxoid state and the saddle point state. The figure demonstrates how the energy barrier for phase slips decreases with increasing applied flux.

Our magnetic susceptibility data points are generated by extracting the slope at

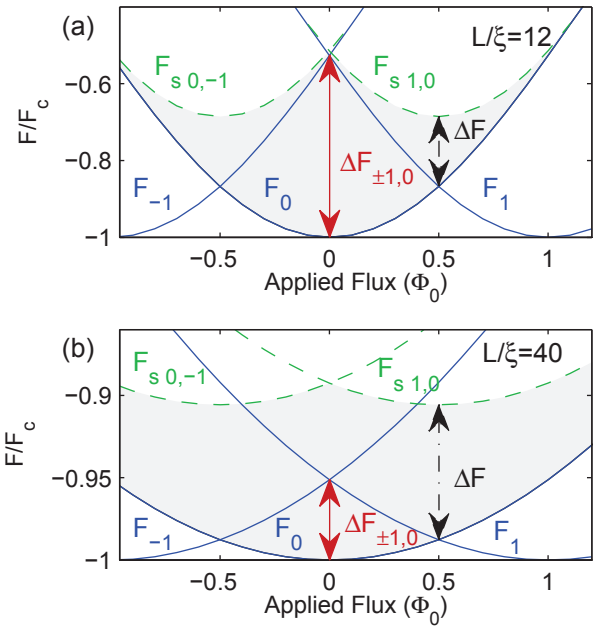

Figure 2.1: Fluxoid and saddle points energies versus applied flux. (a-b)Free energy of fluxoid states (blue solid line, Eq. (2.2)) and saddle point energies (green dashed line, Eq. (2.4)) as a function of applied flux, in units of the condensation energy, F_c. The energy barrier between adjacent fluxoid states at zero applied flux, $\Delta F_{\pm 1,0}$, is indicated by the solid red arrow. The saddle point energy barrier for phase slips is a flux dependent quantity indicated by the gray shaded region. The saddle point barrier at $\phi = 1/2$, indicated by the black dashed arrow, sets the condition for thermal equilibrium.

zero field of the current response of a ring threaded by magnetic flux, where the applied flux is swept through several flux quanta. We are interested in the energy barrier for fluxoid fluctuations at $\phi = 0$, because we expect those fluctuations to affect our zero field susceptibility signal.

Since fluxoid fluctuations represent a thermodynamic sampling of fluxoid states, this description is only valid in thermal equilibrium when frequent phase slips populate higher phase winding states. At low temperatures, if the applied flux is swept through the entire range presented in Fig 2.1, then the lowest saddle point energy barrier, found at the ends of the flux range, determines the onset of phase slips. In

this case the ring will be hysteretic, or even exhibit no transitions if the barrier for phase slips remains large compared to the thermal energy over the entire flux range.

In thermal equilibrium the ring has sufficient thermal energy to make a transition at every crossing of the phase winding state, and there is no hysteresis in the forward and backward field sweeps. Consequently phase slips must be energetically favorable at each value of $\phi = n + 1/2$. Therefore the condition for equilibrium requires the thermal energy to be greater than the energy barrier for phase slips at $\phi = 1/2$, indicated by the black dashed arrow in Fig 2.1(a&b). Fluxoid fluctuations will suppress the thermal equilibrium ring response if the energy barrier for fluxoid fluctuations is also small compared the temperature. For example, the ring in Fig 2.1(a) has a larger barrier for fluxoid fluctuations at $\phi = 0$ than phase slips at $\phi = 1/2$. As the temperature is increased, phase slips will drive the ring into thermal equilibrium before the temperature where fluxoid fluctuations suppress the response. The ring in Fig 2.1(b) is in the opposite limit, the barrier for fluxoid fluctuations at $\phi = 0$ is smaller than the thermal equilibrium barrier for phase slips. In this ring fluxoid fluctuations will not be apparent on the measurement time scale until phase slips allow the ring to enter thermal equilibrium.

2.3.2 Phase slips and equilibrium

The ring is in thermal equilibrium when the thermal energy is greater than the phase slip energy at $\phi = 1/2$, allowing phase slips to occur at a rate that is fast compared to experimental time scales. In our experiments we consider rings to be in thermal equilibrium when no hysteresis is observable in measurements of the ring current vs. applied flux. Langer and Ambegaokar's (LA) formula for the phase slip rate provides additional insight for estimating the onset of thermal equilibrium in our rings. LA theory predicts a phase slip rate, Γ, that depends exponentially on the temperature and the saddle point energy barrier [64], $\Delta F_{s\pm1,0}$, Eq. (2.7).

$$\Gamma \propto \exp\left(-\frac{\Delta F_{s\pm1,0}(T,\phi)}{k_B T}\right) \tag{2.8}$$

LA theory is only valid in the limit where $\Delta F_{s\pm1,0} \gg k_B T$, and phase slips are rare events. We will not make precise predictions for the onset of thermal equilibrium, because the condition for equilibrium, $\Delta F_{s\pm1,0}(T,\phi) \rightarrow k_B T$, occurs outside the limits of the model. Instead we focus on how the exponential dependence of the phase slip rate affects phase slips in our rings.

At low temperatures phase slips can still occur, but the exponential decrease of the phase slip rate with temperature makes it highly unlikely to encounter phase slips within the measurement time. As a result, when we record the current vs. applied flux in our rings at different temperatures, we expect to see no phase slips at the lowest temperatures as long as the applied flux remains low. The flux dependence of $\Delta F_{s\pm1,0}(T,\phi)$ shows that we could drive phase slips in rings even at the lowest temperatures by applying a larger flux. As the temperature increases we expect the phase slip rate to increase exponentially and eventually become fast compared to the measurement time, bringing our rings into thermal equilibrium.

The following sections explore the effects of fluctuations on the ring's response in thermal equilibrium. Each of the models presented below includes a different set of fluctuations. By comparing the model predictions for different ring parameters we can pinpoint the effect of different fluctuations on ring response and set a physical regime where each type of fluctuations will dominate. Specifically we find that in rings with weak phase stiffness a model including only fluxoid fluctuations accurately reproduces the ring response.

2.3.3 Fluxoid number distribution model

We start with a model derived from 1D GL expressions that includes only fluxoid fluctuations. In this model all variation around the ring is described by a single homogeneous phase winding number, n. This model is not complete because it does not include local variations in the amplitude or phase. Put another way this model includes only the large fluctuations between local minima in the GL free energy (see Fig. 2.1), and ignores all the small fluctuations about each local minimum as well as the saddle points and intermediate states. It is instructive to develop this model

because comparisons between this fluxoid only model and more complete models shed light on what portion of the fluctuation response of a ring is due to solely to fluxoid fluctuations.

We return to the mean field 1D GL free energy, Eq. (2.2), which is related to the ring current by $I = -\partial F/\partial \Phi_a$. Taking a derivative yields an expression for the ring current of the n fluxoid state.

$$I_n(T,\phi) = I^0(T)(\phi - n)\left(1 - \frac{\xi(T)^2}{R^2}(\phi - n)^2\right) \tag{2.9}$$

where

$$I^0(T) = \frac{2VB_c(T)^2\xi(T)^2}{\Phi_0\mu_0 R^2}. \tag{2.10}$$

$I^0(T)(\phi - n)$ is the Meissner response which decreases linearly with increasing temperature close to T_c. The cubic term arises from pair-breaking.

The energy associated with each fluxoid current state, $F_n(T,\phi)$, was given in Eq. (2.2). If phase slips occur at a high enough rate, so that the metastable fluxoid states are in thermal equilibrium as discussed in the previous section, we can model [19, 99] the resulting current response as a Boltzmann distribution of fluxoid states.

$$I_F(T,\phi) = \frac{\sum_n I_n(T,\phi)\exp\left(-F_n(T,\phi)/k_BT\right)}{\sum_n \exp\left(-F_n(T,\phi)/k_BT\right)}. \tag{2.11}$$

We label the total ring current generated by fluxoid states I_F to distinguish it from the total ring current including all fluctuation states presented in the next section. We study the susceptibility response of the ring at zero applied flux, $dI(T)/d\phi|_{\phi=0}$. In our rings $L \gg \xi$, so we expand $F_n(T,\phi)$ to lowest order in ξ/R to obtain $F_n(T,\phi) \approx I^0(T)\Phi_0/2(\phi - n)^2 - F_c(T)$. Ignoring the pairbreaking term in the current response yields $I_n(T,\phi) \approx I^0(T)(\phi - n)$. We use these expressions to find the derivative of the total ring current at $\phi = 0$.

$$\left.\frac{dI_F(T)}{d\phi}\right|_{\phi=0} = I^0(T)\left(1 - \frac{\sum_n 2\sigma n^2 \exp(-\sigma n^2)}{\sum_n \exp(-\sigma n^2)}\right) \tag{2.12}$$

where $\sigma \equiv I^0(T)\Phi_0/2k_BT$. Eq. (2.12) shows that including a distribution of fluxoid states reduces the ring's susceptibility response from the mean field value, $I^0(T)$. The second term in Eq. (2.12) is proportional to the RMS fluctuation of the fluxoid number, n. The magnitude of the reduction in susceptibility depends on σ. When σ is large, terms with $n \neq 0$ are small and the susceptibility is approximately equal to the mean field value. When σ is small, the $n = \pm 1$ terms begin to play a significant role. We define a criterion [59] when fluxoid fluctuations reduce the Meissner response by more than 5%

$$\frac{dI_F(T)}{d\phi} \approx I^0(T) < \frac{12k_BT}{\Phi_0}. \tag{2.13}$$

In plots of the susceptibility vs. temperature we observed a suppression below the mean field value for susceptibilities below this cutoff. This downturn in the susceptibility signal, which occurs at T less than T_c, is a hallmark of the suppression of the diamagnetic response by fluxoid fluctuations.

2.3.4 von Oppen and Riedel model

Thus far, we have considered a fluxoid model that predicts the existence of the downturn in susceptibility below T_c. In some rings, near $T = T_c$, the $L \gg \xi(T)$ assumption we made to obtain Eq. (2.12) is not valid because L is of order ξ. As a result, the energy between successive metastable states can no longer be approximated by expanding Eq. (2.2) to lowest order in ξ/R. When we include the quartic term from Eq. (2.2), the GL free energy vanishes rather than increasing indefinitely for $\phi - n > L/\xi(T)$. Thus, the Boltzmann distribution, Eq. (2.11), is not well defined because summing over all n leads to a divergent denominator. The numerator on the other hand remains finite since states with $\phi - n > L/\xi(T)$ do not contribute. Furthermore, our treatment thus far has ignored phase fluctuations that are not uniform around the ring and all amplitude fluctuations.

To address these issues, we compare our simple fluxoid model to complete 1D GL theory as formulated by von Oppen and Riedel [109] which generates numeric solutions for the susceptibility that include all thermal fluctuations within the GL

framework in homogeneous rings. Applying a harmonic oscillator approximation to the VOR model, as discussed in the next section, provides a direct mathematical connection between the VOR model and the fluxoid model discussed in the previous section.

Following von Oppen and Riedel [109], we begin with the expression for the GL energy functional given in Sec. 2.3 Eq. (2.1). In cylindrical coordinates (r, θ, z), we map the free energy onto a one dimensional ring geometry with no lateral variation of the order parameter. $\psi(r, \theta, z) = \psi(\theta)$ and $dx^3 = wdRd\theta$. We redefine $Rd\theta$ as dx.

We rewrite Eq. (2.1) using reduced variables $\psi(x) = \bar{\psi}(\bar{x})\sqrt{|\alpha|/\beta}$, $\bar{\nabla} = \xi\nabla$, and $\bar{x} = x/\xi$. $\xi(T)$ is the superconducting coherence length and is given by $\xi(T) = \hbar/\sqrt{2m^*\alpha}$.

$$
\begin{aligned}
F[\bar{\psi}(\bar{x})] = & \\
& E_0(T)k_BT \int_{-\Lambda(T)/2}^{\Lambda(T)/2} \left[\eta|\bar{\psi}(\bar{x})|^2 + \frac{1}{2}|\bar{\psi}(\bar{x})|^4 \right. \\
& \left. + \left| \left(\bar{\nabla} - \frac{2\pi i}{\Lambda(T)}\phi \right) \bar{\psi}(\bar{x}) \right|^2 \right] d\bar{x}
\end{aligned} \tag{2.14}
$$

η is $+1(-1)$ for temperatures above (below) the superconducting critical temperature T_c. $\Lambda(T)$ is the reduced circumference $\Lambda(T) = L/\xi(T) = \sqrt{8\pi k_B|T - T_c|/E_c}$ and $E_0(T)k_BT = wd\xi(T)B_c(T)^2/\mu_0$ is the condensation energy of a ring section of length $\xi(T)$. The correlation energy for the ring, $E_c = \pi^2\hbar v_f \ell_e/3L^2$, includes the mean free path, ℓ_e, and Fermi velocity, v_f, which is 2.03×10^6 m/s in aluminum. $E_0(T)$ can also be written as

$$
E_0(T) = \frac{(2\pi)^{5/2}}{21\zeta(3)} \left(\frac{k_B|T - T_c|}{E_c} \right)^{3/2} \frac{E_c M_{\text{eff}}}{k_BT}, \tag{2.15}
$$

where $\zeta(3) = 1.021$ is the Riemann zeta function. $M = k_f^2 wd/4\pi$ is the number of transverse channels. k_f is the Fermi wave vector, which for an aluminum ring is $k_f = 1.75 \times 10^{10}\,\text{m}^{-1}$. Including disorder results in an effective number of channels, $M_{\text{eff}} = M\ell_e/L$.

We obtain the thermodynamic expression of the current from the flux derivative of the ring's partition function.

$$I(T,\phi) = -k_B T \frac{1}{Z_{sc}} \frac{\partial}{\partial \Phi_a} Z_{sc} \tag{2.16}$$

The partition function is the path integral of the GL free energy.

$$Z_{sc} = \int [d\bar{\psi}(\bar{x})][d\bar{\psi}^*(\bar{x})] \exp\left(\frac{-F[\bar{\psi}(\bar{x})]}{k_B T}\right) \tag{2.17}$$

The VOR model uses a transfer matrix technique [93] to map the Ginzburg-Landau path integral partition function, Eq. (2.17), onto another partition function

$$Z = \sum_{l=-\infty}^{\infty} \exp(-i2\pi l\phi) \sum_{n=0}^{\infty} \exp(-2E_0(T)\Lambda(T)\mathscr{E}_{n,l}) \tag{2.18}$$

where $\mathscr{E}_{n,l}$ are the eigenvalues of the fictitious 2D single-particle Hamiltonian,

$$H = -\frac{1}{8E_0(T)^2}\nabla^2 + \frac{1}{2}\eta\vec{r}^2 + \frac{1}{4}\vec{r}^4. \tag{2.19}$$

We define $\vec{\rho} = (2E_0(T))^{1/3}\vec{r}$ and rewrite Eqs. (2.18) and (2.19) to emphasize the parameter $\gamma(T)$ [60].

$$Z = \sum_{l=-\infty}^{\infty} \exp(-i2\pi l\phi) \sum_{n=0}^{\infty} \exp(-\gamma(T)^{1/3}\mathscr{E}_{n,l}) \tag{2.20}$$

$$H = -\frac{1}{2}\nabla^2 + \frac{1}{2}\frac{\Lambda(T)^2}{\gamma(T)^{2/3}}\vec{\rho}^2 + \frac{1}{4}\vec{\rho}^4 \tag{2.21}$$

The temperature dependence is set by the coherence length through the relation $\Lambda(T) = L/\xi(T)$. The parameter

$$\gamma(T) \equiv \frac{\Lambda(T)^3}{2E_0(T)} = \frac{42\zeta(3)}{\pi}\frac{k_B T}{M_{\text{eff}} E_c} \tag{2.22}$$

determines the relative effect of fluxoid fluctuations on the ring's susceptibility response [60]. Gamma is related to the physical ring parameters as follows $\gamma \propto TL^3/wdl_e{}^2$. The $\gamma(T)$ parameter is also inversely proportional to the superconducting phase stiffness, K, which we express in terms of our parameters $K = L\Lambda(T)^2/w\gamma(T)$ [12]. For rings with larger $\gamma(T)$ as the temperature approaches T_c several phase winding states are thermally accessible and contribute to a suppress the susceptibility. The definition of γ introduced in Koshnick *et al.* [60] made the approximation $T = T_c$. The larger temperature range explored in this paper makes it necessary to reintroduce the T dependence. We use the relation $I^0(T) = 4\pi^2 k_B T L^2/\Phi_0 \xi(T)^2 \gamma(T)$ to compare the VOR model to the mean field and fluxoid models.

Eqs. (2.20) and (2.21) can be solved numerically. The Hamiltonian can be rewritten as a harmonic oscillator with a quartic perturbation. We write matrix elements in terms of the coefficients and diagonalize numerically to find the eigenvalues [111, 10]. The eigenvalues are used in the partition function, Eq. (2.20), and substituted into the thermodynamic equation for the current, Eq. (2.16), to generate the full current response. We find the zero-field susceptibility by taking a derivative with respect to applied flux at $\phi = 0$.

Analytic solutions can be instructive, and as a result it is useful to find approximations to the full VOR model that are valid over some set of ring parameters or temperatures. One such approximation is to ignore the quartic perturbation to the Hamiltonian, which then takes the form of a simple harmonic oscillator. Moreover, making this approximation provides a direct mathematical connection between our fluxoid model and the full 1D GL model of VOR.

2.3.5 Harmonic oscillator model

The harmonic oscillator (HO) approximation is valid at temperatures well below T_c, where the wave functions contributing to Eq. (2.20) only extend over a narrow region around the minimum of the Mexican hat potential of Eq. (2.21), so that the latter can be approximated by a quadratic expansion. In this case, fluctuations from the quartic nature of the potential should not play a significant role. We refer to the fluctuations

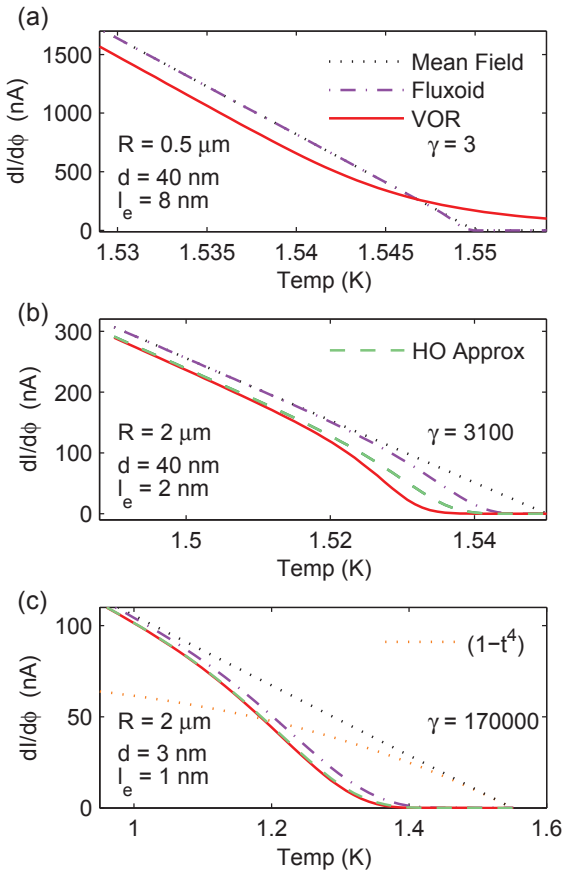

Figure 2.2: Theoretical response from mean field, fluxoid, von Oppen, and HO models. Theoretical susceptibilities calculated using the mean field model, black dotted line Eq. (2.10), the fluxoid model, purple dot-dash line Eq. (2.12), the VOR model, red solid line Eqs. (2.16, 2.20, 2.21), and its approximate HO solution, green dashed line Eqs. (2.16, 2.26), for rings with $w = 80\,\text{nm}$ and $T_c = 1.55\,\text{K}$. For all values of $\gamma(T = T_c)$, the VOR and HO response well below T_c only match the mean field and fluxoid predictions if T_c is renormalized. a) $\gamma(T = T_c) = 3$. The VOR model predicts a susceptibility above T_c. b) $\gamma(T = T_c) = 3100$. A downturn occurs at $dI/d\phi \approx 12k_BT/\Phi_0 \approx 120\text{nA}$, $T \approx 1.52\,\text{K}$. The fluxoid, HO and VOR models reproduce the overall lineshape of the downturn, up to an offset in T_c. However, the three models predict downturns of different sizes with the largest predicted by the VOR model. c) $\gamma(T = T_c) = 170,000$ Fluxoid fluctuations dominate the response over a wide temperature range and the fluxoid and HO models become increasingly accurate predictors of the full fluctuation theory.

in this model as quadratic fluctuations, rather than Gaussian fluctuations, to avoid confusion with small order parameter fluctuations above T_c, which are often referred to as Gaussian fluctuations.

We can quantify the range of validity for the HO model using the Ginzburg parameter. The Ginzburg parameter is $G_i = |T_{LG} - T_c|/T_c$, where T_{LG} is the temperature where the heat capacity due to fluctuations is equal to the heat capacity jump at the critical temperature. We can rewrite the Ginzburg parameter with respect to $\gamma(T)$, $T_c/E_c G_i \propto \sqrt{(}\gamma)$ [60]. At temperatures below the limit set by the Ginzburg parameter, fluctuations are small and approximated as quadratic fluctuations from GL theory and the HO model is valid. At temperatures close to T_c the quartic term becomes significant and a non-perturbative approach, presented in the previous section is required to capture the fluctuation response.

Eigenstates of the Hamiltonian given in Eq. (2.21) have the form $\vec{r} = |r| \exp(il\phi)$, so the Hamiltonian can be written as a 1D problem, $H = -\frac{1}{2}\frac{d^2}{dr^2} + V(r)$ where

$$V(r) = \frac{l^2}{2r^2} + \frac{1}{2}\frac{\Lambda(T)^2}{\gamma(T)^{2/3}} r^2 + \frac{1}{4} r^4. \tag{2.23}$$

Expanding $V(r)$ about its minimum at $R_{\mathrm{m}}(l)$ leads to the eigenvalues

$$\mathscr{E}_{n,l} = \frac{l^2}{2R_{\mathrm{m}}(l)^2} + \frac{R_{\mathrm{m}}(l)^4}{4} + \omega(n + 1/2) \tag{2.24}$$

where $\omega = \sqrt{\Lambda(T)^2/\gamma(T)^{2/3} + 3R_{\mathrm{m}}(l)^2 + 3l^2/R_{\mathrm{m}}(l)^4}$.

Only terms that change with l, the angular momentum coordinate in the fictitious Hamiltonian, contribute to the flux dependence of the partition function, thus only these terms contribute to the thermodynamic ring-current. If we make an approximation and only include the $l^2/2R_{\mathrm{m}}(0)^2$ terms, where $R_m(0)$ is the value for r that minimizes $V(r)$ when $l = 0$, the current from Eq. (2.16) is

$$I_{HO}(T, \phi) =$$

$$\frac{k_B T}{\Phi_0} \frac{\sum_{l=1}^{\infty} 4\pi l \sin(2\pi l\phi) \exp(l^2\gamma(T)/2\Lambda(T)^2)}{1 + \sum_{l=1}^{\infty} 2\cos(2\pi l\phi) \exp(l^2\gamma(T)/2\Lambda(T)^2)}, \tag{2.25}$$

which is exactly equivalent the fluxoid current Eq. (2.11). Through this approximation we are able to show a direct link between the harmonic oscillator approximation to the VOR model and the fluxoid model. Including the second two terms of Eq. (2.24), which account for the angular momentum dependence of ω and $R_{\rm m}(l)$, we get

$$\begin{aligned} Z = & \sum_{l=-\infty}^{\infty} \exp(-i2\pi l\phi) \exp(-\gamma(T)^{1/3} V(R_{\rm m}(l))) \\ & \times \frac{\exp(-\gamma(T)^{1/3}\omega/2)}{1 - \exp(-\gamma(T)^{1/3}\omega)}. \end{aligned} \tag{2.26}$$

Using this simplified partition function we can find the ring's current and consequently its susceptibility in the limit where we ignore only quartic fluctuations.

2.3.6 Comparison of models

We have presented the theoretical basis for four models including: the mean field model, the fluxoid model, the harmonic oscillator model and complete 1D GL theory formulated by von Oppen and Riedel. We now compare the physics captured by each model in Fig. 2.2 by plotting the theoretical susceptibility response as a function of temperature for rings with three different $\gamma(T = T_c)$ parameters.

The mean field model is our baseline. It gives the ring response in the absence of all superconducting fluctuations. At the other extreme, the VOR model incorporates all thermally activated GL fluctuations into the ring response. In between we have the fluxoid model, which includes only fluxoid fluctuations and the harmonic oscillator model which ignores only quartic fluctuations. By comparing these models for rings

with different $\gamma(T = T_c)$ we determine how fluctuations contribute to the response.

One striking feature in all three Fig. 2.2 plots is that both the VOR model and its HO approximation have an offset in the linear regime, far below T_c, compared to the mean field and fluxoid models. This downshift reflects a renormalization in T_c due to consideration of all possible fluctuation modes.

Fig. 2.2(a) shows a ring with $\gamma(T = T_c) = 3$. The low gamma parameter means it has strong phase stiffness, making fluxoid fluctuations unlikely. The temperature range where we expect to encounter fluctuations is very close to T_c. The two models that include only quadratic fluctuations, the HO model and the fluxoid model, both fail to reproduce the lineshape of the VOR model for this ring. We are clearly within the temperature range prescribed by the Ginzburg parameter where quartic fluctuations must be taken into account. Susceptibility enhancing amplitude fluctuations at and above T_c overwhelm the susceptibility reduction expected from fluxoid fluctuations. A downturn is not observable, instead the small $\gamma(T = T_c)$ leads to a susceptibility signal above T_c.

When $\gamma(T = T_c) = 3100$, as shown in Fig. 2.2(b), the fluxoid induced downturn becomes visible below T_c starting at $T \approx 1.52\,\mathrm{K}$ and 120 nA, as predicted by our fluxoid criterion, Eq. (2.13). All three fluctuation models qualitatively reproduce the shape of the susceptibility suppression. As expected, the VOR model predicts a greater susceptibility suppression than the fluxoid or HO models, because only the VOR model includes all thermal fluctuations. The excess suppression between the fluxoid and VOR models is presumably due to contributions from non-homogeneous phase winding solutions, amplitude fluctuations, or both. While the excess suppression between the HO and VOR models is due to fluctuations caused by the quartic nature of the potential.

For $\gamma(T = T_c) = 170,000$, shown in Fig. 2.2(c), the susceptibility response is dominated by fluxoid fluctuations, shown by the almost identical lineshape shared by the fluxoid model and the VOR model. The total response is also well represented by the harmonic oscillator approximation showing that in this region nearly all fluctuations are quadratic in nature.

Fig. 2.2(c) shows a larger temperature range than the previous panels, and the GL approximation that T is close to T_c is not valid over the whole plot. GL theory is valid in the range of temperature where the linear mean field response approximates a temperature dependence that goes as $(1-t^4)$, $t = T/T_c$, shown as an orange dotted line. An alternative criterion is that $T > \Delta(T)$, where $\Delta(T)$ is the superconducting gap. These both result in approximately the same range of validity. GL theory has been applied with success at temperatures far from T_c, but interpretation of results in this regime should be treated with caution. The $(1-t^4)$ dependence is not included in panels (a) and (b) because all plotted temperatures lie within the valid range.

In the next section we describe our measurement of ring susceptibility for rings with different $\gamma(T = T_c)$. We find good agreement between our data and the fluctuation response predicted by the fluxoid model and full 1D GL theory.

2.4 Sample and measurement technique

2.4.1 Sample preparation

We measured quasi-one-dimensional superconducting rings in a dilution refrigerator [17] with a scanning SQUID susceptometer [44] that was specifically designed for this purpose. We focus on data from two different samples expected to exhibit fluxoid fluctuations. Sample I's rings were fabricated and measured previously [19]. The rings were narrow and dirty with $T_{c\mathrm{I}} \approx 1.5$ K. They were made by depositing a 40 nm thick aluminum film by e-beam evaporation at a rate of about 1 Å/s and a pressure of approximately 10^{-6} mBar on a Si substrate patterned with poly(methyl methacrylate) (PMMA) resist. During the deposition, the rate temporarily dropped to a negligible level for about 10 min and subsequently recovered. This unintentional delay caused the formation of two superconducting layers separated by an AlOx tunneling barrier. The coupling between the two Al layers depended on the width of the rings with narrow rings ($w \leq 190\,\mathrm{nm}$) and wide rings ($w \geq 250\,\mathrm{nm}$) showing a single order parameter. Intermediate widths showed evidence of weak interactions

between the two layers leading to two order parameter effects [19]. In this work we only present data from the narrow rings which showed no two order parameter behavior. However, due to the oxidization process we suspect the thinnest rings have a large oxidized layer that reduces the thickness of the superconductor. Consequently we expect that these rings have an effective height that is less than 40 nm. We can test this prediction by extracting the ring's cross-section from fits to the VOR model.

The rings on sample II were fabricated specifically for this paper. The fabrication process was almost identical to the rings from sample I except the evaporated film was thinner, $d = 15\,\text{nm}$, and there was no interruption in the evaporation. The deposited rings were wide and dirty with $T_{c\text{II}} \approx 2.1\,\text{K}$. Of the many fabricated rings of different widths and radii, only the widest rings, $w \approx 850\,\text{nm}$, had a diamagnetic response. The next widest rings, $w \approx 450\,\text{nm}$, showed no signs of superconductivity indicating that they were oxidized throughout. This evidence makes it difficult to predict with certainty what portion, if any, of the 850 nm rings are oxidized. For each sample we used Ginzburg Landau models [104, 112, 19] to fit a zero temperature penetration depth $\lambda_{\text{I}}(0) \approx 800$ nm, $\lambda_{\text{II}}(0) \approx 1.5$ μm, and coherence length $\xi_{\text{I}}(0) \approx 80$ nm, $\xi_{\text{II}}(0) \approx 30$ nm.

The agreement with theory is perhaps surprising given that our rings may not be in the 1D limit. We note that finding agreement between the data and the model is not sufficient to prove the correctness of the theory. Zhang applied finite width corrections to 1D GL theory and found close agreement in the susceptibility response of 1D and 2D rings [111]. Despite the large width of the rings, Abrikosov vortices are not expected to be present in our rings at low applied fields [7, 55], and thus will not impact our zero field susceptibility measurements.

2.4.2 Measurement

Measurements were done with a voltage biased DC SQUID susceptometer amplified by a series-array SQUID preamplifier [45]. The SQUID is mounted on a piezo-resistive scanning assembly [17], which is connected to the mixing chamber of a dilution refrigerator through a single copper braid. The temperature of the scanner and sample

is controlled with sub-millikelvin precision through feedback. The SQUID sensor's counter-wound geometry, with on-sensor modulation coils for feedback, enable cancellation of an applied field to one part in 10^4 [44]. The ring current is measured by positioning the SQUID about $1\,\mu$m above the ring and recording the flux induced by the ring's current in the SQUID's $4.6\,\mu$m diameter pick-up loop. During the measurement, the applied flux threading the ring is varied by several flux quanta at a few Hertz by an on-sensor field coil. This measurement is repeated $13\,\mu$m above the ring and the ring signal is computed as the difference between the two positions for each value of applied flux. This procedure allows us to achieve an additional three orders of magnitude of background cancellation. A more detailed description of the measurement system was given by Koshnick *et al* [60].

We plot the flux induced in the SQUID's pick-up loop as a function of the flux applied by the field coil in Fig. 2.3 for two different rings. The measurement is repeated to record the full temperature dependence of the ring's response. The ring current, I, is coupled as flux into the SQUID pick-up loop through their mutual inductance, M. $\Phi_{\rm SQUID} = MI$. We estimate the mutual inductance between the SQUID pick-up loop and a ring by calculating the mutual inductance between two on axis rings with radii r_1 and r_2 a distance z apart.

$$M = \pi\mu_0 r_1 r_2 \int_0^\infty d\kappa e^{-\kappa|z|} J_1(\kappa r_1) J_1(\kappa r_2) \tag{2.27}$$

J_1 is a Bessel function of the first kind. For all our mutual inductance calculations we assume a ring-pick-up loop separation of $1\,\mu$m. Through a separate fitting technique [19] we estimate the actual distance between the pick-up loop and the ring to range from $0.75 - 1.1\,\mu$m. Ring currents and susceptibilities quoted later in this paper have error bars that reflect this systematic uncertainty in the coupling factor which would shift the entire data set.

The ring response curves plotted in Fig. 2.3 evolve from cubic and non-hysteretic at low temperatures through a hysteretic regime to periodic and non-hysteretic near T_c. At low temperatures the current response is well described by the GL current

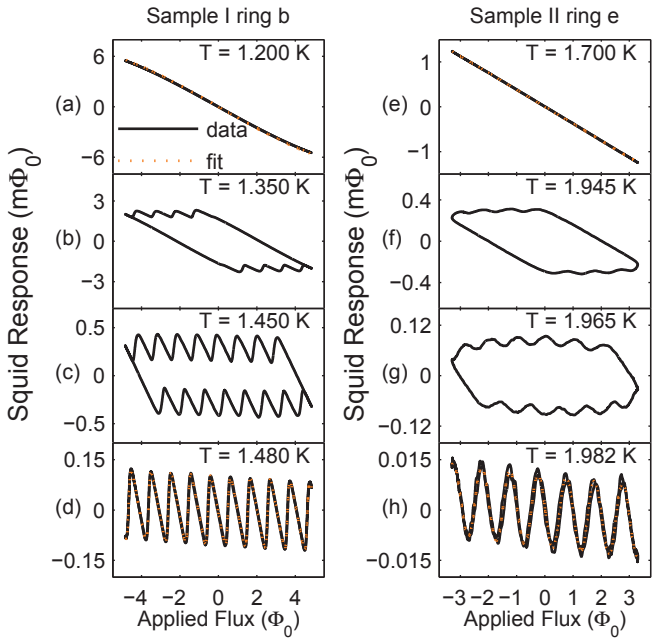

Figure 2.3: $\Phi - I$ Curves at different temperatures. Plots of SQUID response vs. applied flux at different temperatures for a ring from each of the two samples. Rings b and e refer to specific rings plotted in Fig. 2.4. Ring b $T_c = 1.56\,\mathrm{K}$ and ring e $T_c = 2.08\,\mathrm{K}$. The curves evolve from non-hysteretic with no fluxoids at low temperatures, through a hysteretic regime, to non-hysteretic with a change in fluxoid number at every applied flux quantum near T_c. The orange dotted lines are fits to the GL current, Eq. (2.9), at low temperatures and to the Boltzmann distribution, Eq. (2.11), at high temperatures. We extract the ring's susceptibility at each temperature by taking the derivative at $\phi = 0$.

with no phase windings, Eq. (2.9) with $n = 0$, shown as a orange dotted line in panels (a) and (e) of Fig. 2.3. Due to the low temperatures and small applied flux the energy barrier for phase slips is large compared to $k_B T$. As a result, no phase slips occur on the scale of the measurement time and the ring remains in the $n = 0$ fluxoid state. As the temperature increases and approaches the saddle point energy barrier phase slips begin to occur, which allows the ring to transition to higher fluxoid states; however, the phase slip rate is still slow compared to the measurement time leading to a hysteretic response.

Finally, as the temperature approaches T_c the phase slip rate becomes fast and the ring relaxes to thermal equilibrium. As the flux is swept phase winding transitions occur within some range of $\phi = n + 1/2$. The ring's response is no longer hysteretic and can be modeled as a Boltzmann distribution of all fluxoid states, Eq. (2.11), shown as a orange dotted line in panels (d) and (h) of Fig. 2.3. We extract the magnetic susceptibility of the ring at each temperature where the ring is in thermal equilibrium by fitting a low order polynomial to obtain the slope at $\phi = 0$.

2.4.3 Susceptibility data

We measured thirty-eight rings on sample I and twelve rings on sample II. Sample I was fabricated and measured primarily for a different experiment [19]. As a result only eight of the rings measured have sufficient susceptibility data over a wide enough temperature range to make comparisons with the models presented in the previous section. Two representative rings were selected from Sample I for this paper. The three rings from Sample II were chosen to show a variety of ring parameters, and because they had the most dense susceptibility data over the important temperature range. The set of five rings allows us to explore the effects of ring size and mean free path on the fluctuation response. Fig. 2.4 shows the susceptibility vs. temperature data for the five rings. Each ring's physical parameters are given in table 2.1. We extracted the ring radii from the flux periodicity of the ring's response in thermal equilibrium and confirmed the measurement though SEM imaging. The ring thicknesses were measured with AFM, and the width with SEM. Fitting to the VOR model allowed us to estimate values for the ring's cross-section and mean free path. We used the measured ring width and thickness plus an additional error factor as an upper limit on the cross-section parameter in the VOR model for rings (c-e). No lower limit was enforced due to the possibility that oxidation may have reduced the superconducting cross-section.

Fig. 2.4 plots the susceptibility vs. temperature curves for five rings. The blue susceptibility data points represent the slope at $\phi = 0$ of the SQUID response at different temperatures scaled by the ring-SQUID mutual inductance to obtain the

	Directly Measured			Extracted from VOR fits			
	R (μm)	w (nm)	d (nm)	wd (nm^2)	95% CI	ℓ_e (nm)	95% CI
a(I)	0.50	123	40	1598	1140- 2314	6.4	4.3 - 9.4
b(I)	1.97	90	40	583	492- 1177	8.5	4.4 -10.4
c(II)	1.21	840	15	13319	2811-14790	0.11	0.09- 0.48
d(II)	1.75	850	15	14790	11896-14790	0.08	0.07- 0.11
e(II)	1.82	850	15	13602	9172-14790	0.08	0.07- 0.12

Table 2.1: Values for the cross-section and mean free path, extracted from fits to the VOR model, are given with their 95% confidence interval. An upper limit of 14790 nm^2 was enforced on the ring cross-section to constrain the fits for rings (c-e).

ring current. The error bars represent height errors in our calculation of the mutual inductance, Eq. (2.27). This error is systematic and expected to be the same for all points in a panel. Using T_c, and the temperature independent portions of $\gamma(T)$ and $E_0(T)$ as the free parameters, the red line is a fit of the data to the VOR model, Eqs. (2.16, 2.20, 2.21). The fit results used to generate the red curves are given in table 2.2. We report values for $\gamma(T)$ at T_c and $E_0(T)$ at $T = 0$. The reported T_c represents the nominal mean field T_c entering the VOR model [109]. The fitted values of $\gamma(T = T_c)$ are also listed on each of the plots. The black dotted line is the mean field ring response, Eq. (2.10), which is the expected response if no fluctuations were present. Deviations in the data from the black dotted line show the influence of fluctuations on a given ring. Finally, the gray region of the curve is the 95% confidence interval (CI) obtained from bootstrapping.

Using the fit results from table 2.2 along with the known values of the ring radii given in table 2.1 we can extract values for the ring's cross-section and mean free path from expressions for $E_0(T)$, Eq. (2.15), and $\gamma(T)$, Eq. (2.22). The ring parameters obtained in this way are given along with their 95% confidence intervals in table 2.1. We note that the mean free paths extracted from VOR fits for rings (c-e) are extremely small, $\ell_e \sim 1$Å. Physically the mean free path is the distance electrons

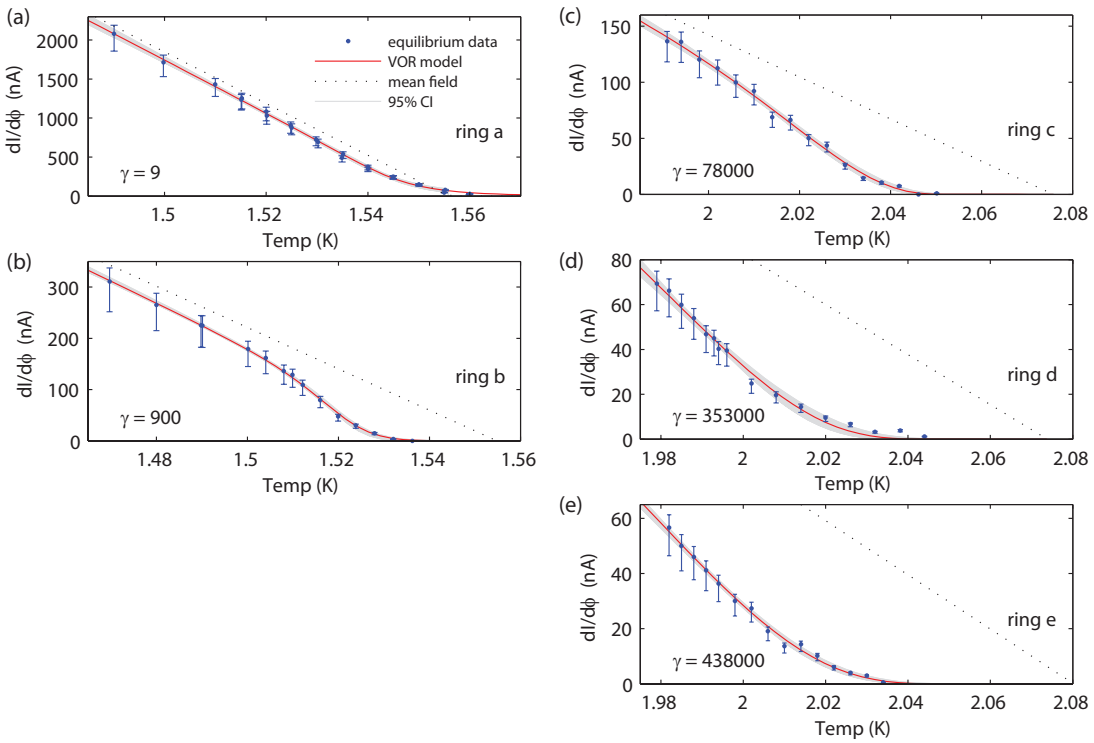

Figure 2.4: Fluxoid fluctuations reduce the ring's diamagnetic susceptiblity near T_c. Zero field susceptibility (blue dots) vs. temperature plotted for five different rings. In all plots the solid red line is a fit to the VOR model, Eqs. (2.16, 2.20, 2.21). The dotted black line is the expected mean field susceptibility given by $I^0(T)$, Eq. (2.10), using the VOR fit parameters. The gray shaded area represents the 95% confidence interval from bootstrapping. The error bars represent the systematic uncertainty in the SQUID-ring mutual inductance.

travel before scattering, which should be limited to the lattice constant of 4Å in aluminum. However, as a fit parameter these low values are consistent with mean free paths extracted from measurements of H_{cII} in thin aluminum films [40]. Alternatively these small mean free paths may indicate that we are reaching the limits of the validity of 1D GL theory for rings with especially large widths or that the fit is under-constrained as described below.

Due to the evaporation conditions discussed previously, we're not confident that the entire cross-section of each ring is superconducting. For the two rings on sample

	T_c (K)	95% CI	$\gamma(T=T_c)$	95% CI		$E_0(T=0)$	95% CI
a(I)	1.556	1.554-1.557	9.20	6- 14		2138	1850-2550
b(I)	1.555	1.550-1.556	899	760-1660		898	820-1300
c(II)	2.076	2.072-2.086	78×10^3	(18- 95)	$\times 10^3$	2650	1180-2870
d(II)	2.074	2.066-2.083	353×10^3	(261- 443)	$\times 10^3$	2590	2280-2730
e(II)	2.080	2.075-2.086	438×10^3	(294- 536)	$\times 10^3$	2370	1910-2550

Table 2.2: Table of fitted values. We used the temperature independent portions of $\gamma(T)$ and $E_0(T)$ as fit parameters in the VOR model. This table reports values for $\gamma(T=T_c)$ and $E_0(T=0)$ as well as the limits of the 95% confidence interval obtained from bootstrap analysis for the data presented in Fig. 2.4.

I the fitted cross-sections are smaller than the values found using AFM/SEM, which confirms our suspicion that a portion of the ring is oxidized. The data from the three sample II rings is within the downturn region, i.e. the decrease in the susceptibility is not linear even at the lowest plotted temperatures. Practically we are limited on the low end of the temperature range by the point where the SQUID response curves go hysteretic. A three parameter fit is under-constrained and it is consequently difficult to get accurate VOR fits without susceptibility data at lower temperatures including the point where the data is reduced from the linear response. As a result, for rings (c-e) we put a strict upper limit of $w \times d = 14790\,\text{nm}$ on the cross-section which acted as an additional constraint on the VOR fits. The cross-sections extracted from fits to the constrained VOR model for the rings on sample II agree well with the AFM/SEM cross-section indicating little oxidation. A similar limit was not applied to rings (a-b) because data in the linear susceptibility region kept the fit from being under-constrained. We find good agreement between the susceptibility data and fits to the VOR model for all rings except ring (d), where it is clear that the VOR model does not capture the shape of the data at high temperatures. It is unclear why the VOR model provides a poor fit for this ring. It is possible that errors from extracting the susceptibility near T_c, errors that are not accounted for in the error bars, are particularly large for measurements on this ring.

Looking at the sequence of five rings it is clear that the extent of the suppression

of superconductivity increases as $\gamma(T = T_c)$ increases. This is just what we expect for a series of rings where fluxoid fluctuations play a larger and larger role.

Ring (a) shows an enhancement of the superconducting response above T_c. This response is caused by amplitude fluctuations and has been studied by Koshnick *et al.* [60] and Zhang and Price [112]. As we showed in our description of the theoretical models, only the VOR model can correctly reproduce the upturn in susceptibility above T_c.

The remaining four rings in Fig. 2.4 show a suppression of the susceptibility signal below the mean field response (black dotted line). However, of the plotted rings only ring (b) has a large enough temperature range to observe a downturn from the linear regime. The downturn for ring (b) occurs at $T \approx 1.52\,\mathrm{K}$ and $120\,\mathrm{nA}$, which corresponds to the criterion for fluxoid fluctuations given in Eq. (2.13). Such agreement validates our criterion for the onset of susceptibility suppression driven by fluxoid fluctuations. The free energy configuration space for ring (b) resembles Fig. 2.1(a) where phase slips onset and bring the ring into thermal equilibrium before fluxoid fluctuations at zero applied flux are energetically accessible. The full temperature range plotted for rings (c-e) is already deep in the suppression region. This is due to the fact that for rings (c-e) fluxoid fluctuations and phase slips onset at approximately the same temperature as shown in Fig. 2.1(b). In the next section we expand the temperature range by adding susceptibility data from lower temperature hysteretic ring response curves. The additional data confirms that the response is suppressed from the mean field value.

We have shown that the VOR model, based on 1D GL theory, describes the temperature dependence of the susceptibility. To get a feeling for the type of fluctuations that play a role in the ring response we plot the fluxoid model and the HO model in addition to the VOR model and mean field model for ring (c) in Fig. 2.5. It is clear that fluxoid fluctuations cause the majority of the suppression. Quadratic fluctuations of a non-fluxoid nature described by the HO model contribute to the renormalization of T_c and quartic fluctuations described by the VOR model play only a minor role. In fact the fluxoid model would fit the data equally well with just

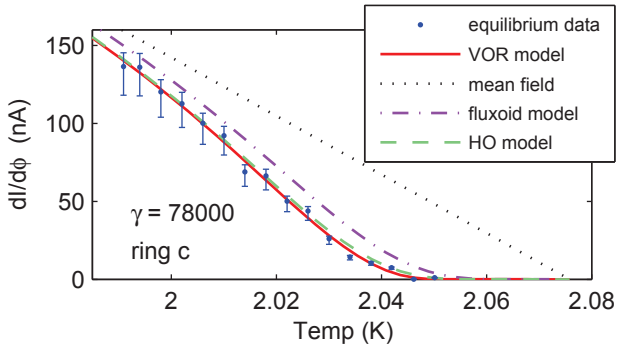

Figure 2.5: Comarparison of ring data with theoretical models. Comparison of the four models plotted using parameters obtained from fitting the data from ring (c) to the VOR model. Fitting to the fluxoid model would yield an equally good fit with a slightly different T_c.

a shift in the T_c.

The data set, taken as a whole, confirms the points we made throughout this paper. Fluxoid fluctuations not only suppress the rings superconducting response but play an increasingly large role in the suppression as $\gamma(T = T_c)$ increases. We showed that our susceptibility vs. temperature data is well described by a GL model for homogeneous rings, formatted by von Oppen and Riedel [109], that includes all thermally activated fluctuations. The largest gamma rings can be equally well described by our simple fluxoid only model. Furthermore we can use fits to the VOR model to reproduce some of the rings' physical parameters including the cross-section and mean free path. Finally, by using VOR fit parameters we can employ our two approximate models, the fluxoid model, and the harmonic oscillator model, to determine the how much of the suppression is due to either fluxoid fluctuations or quartic fluctuations, shown for ring (c) in Fig. 2.5.

2.4.4 Hysteretic susceptibility data

For rings (c-e) in Fig. 2.4 we expect the onset of the downturn induced by fluxoid fluctuations to occur in a temperature range where the SQUID response curves are

hysteretic, as shown in Fig. 2.3. This is due to the fact that in these longest, dirtiest rings $L \gg \xi(T)$ and fluxoid fluctuations are already energetically favorable at the temperature when phase slips begin to occur, as discussed in Sec. 2.3.1. Fluxoid fluctuations are never energetically favorable for ring (a) and they onset well after phase slips in ring (b). From the ring (b) susceptibility data we see that phase slips onset at $\sim 1.3\,\mathrm{K}$ while fluxoid fluctuations onset at $\sim 1.51\,\mathrm{K}$.

To demonstrate that the data presented represents a real reduction in the ring response we examine the susceptibility signals at lower temperatures that fall in the hysteretic regime. We extract susceptibility data by taking the slope at zero current on the long continuous sides of the hysteretic curves.

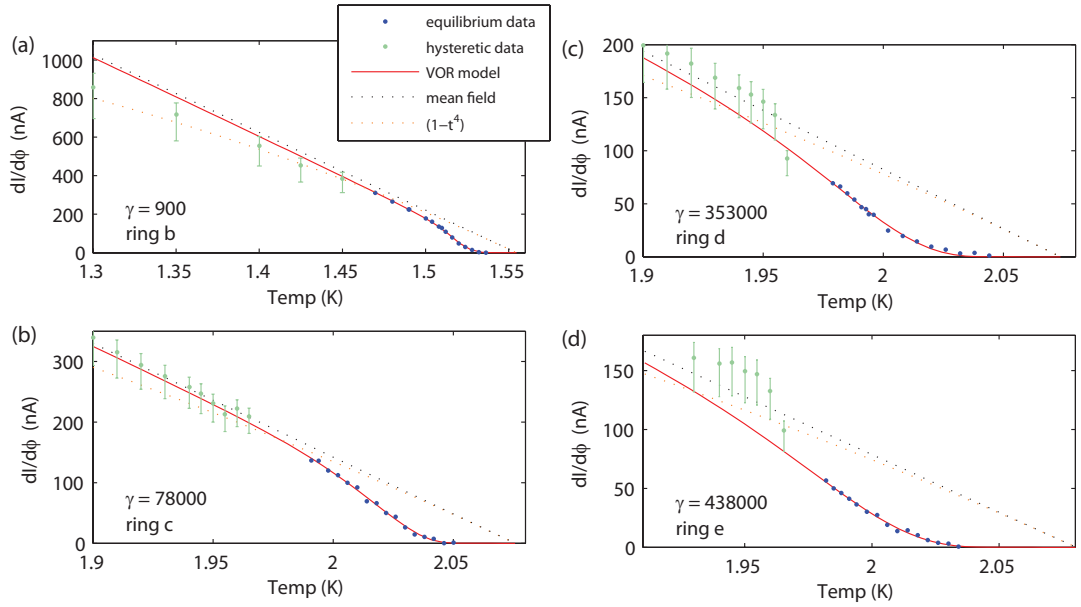

Figure 2.6: Hysteretic Data. Susceptibility data from rings (b-e). The green points are the slopes of the hysteretic curves, which estimate the susceptibility in the hysteretic regime. The error bars account for a systematic error in the coupling constant that would shift all points together. The blue points are reproduced from Fig. 2.4, which plots the susceptibility of the ring's response in thermal equilibrium. The red solid line is a fit of the blue non-hysteretic data to the VOR model and the black dotted line is the mean field response, both are reproduced from Fig. 2.4. Also plotted is the $(1 - t^4)$ temperature dependence which limits the validity of GL theory.

Fig. 2.6 shows susceptibility data in the hysteretic regime (green points) and reproduces the susceptibility data and fits from the non-hysteretic regime (blue points and solid red line) from rings (b-e) in Fig. 2.4. Fig. 2.6 also shows the $(1 - t^4)$ dependence, plotted as an orange dotted line, that sets the validity of our GL based models.

The hysteretic data points in rings (c-e), panels (b-d), follow the mean field curve until a crossover point when they line up with the VOR model and the higher temperature susceptibility data. This provides evidence that the susceptibility measured from the SQUID response curves in thermal equilibrium is suppressed from the mean field value. The drop in susceptibility from the mean field value occurs when the phase slip rate is sufficiently high and multiple fluxoid states compete to suppress the response.

2.5 Conclusions

Superconducting phase slips in one dimensional rings and wires have been the subject of theoretical and experimental interest for decades. While phase slips in 1D structures determine the onset of resistance, the fluxoid processes we described here cause the loss of another hallmark of superconductivity, the ability to screen magnetic fields. In this paper we have outlined four models that describe the effects of superconducting fluctuations on the susceptibility response in rings. We have shown that the responses of rings with various physical parameters can be characterized by 1D GL theory as described by von Oppen and Riedel for uniform rings that includes all thermal fluctuations. By comparing the models we can determine the types of fluctuations that contribute to the response of a given ring. We found that for rings with weak phase stiffness the ring response can be described using a fluxoid only model, indicating that these types of fluctuations are the dominant cause of suppression of the susceptibility signal. One could imagine extending this ring system to a weakly connected grid, linking our results to the field of percolation superconductivity. Additionally, achievable experimental conditions allow fluxoid fluctuations to occur at

temperatures down to 50 mK. Such a setup could provide experimental conditions for examining the quantum mechanical behavior of a 1D ring [73].

Part III

Superconductivity in two dimensions

Chapter 3

Introduction

Complex oxides are a class of materials with a crystal structure made up of oxygen and metallic ions. Typically the constituent compounds are abundant, stable and tunable making them exciting candidates for the basis of future technologies.

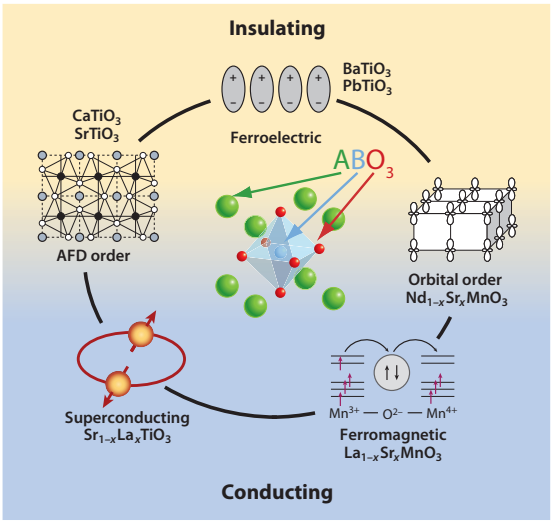

Figure 3.1: The perovskite crystal family include a diverse array of properties. Figure adapted from [113].

The perovskite crystal structure is one of the most common in the complex oxide family and includes compounds of the form ABO_3. A and B are transition metals

ions in an oxygen lattice. Both lanthanum aluminate and strontium titanate have a perovskite crystal structure.

As shown in Fig 3.1 the perovskite-oxide structure supports many different physical behaviors simply by changing and doping the metallic ion sites. Moreover the combination of structural compatibility and recent advances in deposition techniques allow for precise growth of complex oxide thin films, interfaces and supercells.

An interface between two complex oxides tunes different degrees of freedom in the parent compounds including the charge, orbital, spin and lattice parameters. These atomic scale changes can generate new phenomena at the interface that are not observed in either constituent material. One example is the interface between $LaAlO_3$ and $SrTiO_3$ (LAO/STO). LAO/STO will be the focus of chapters 4-6.

3.1 Electronic reconstruction

LAO and STO are both band insulators. (LAO band gap: 5.6 eV and STO band gap: 3.2 eV) Yet, when at least four unit cells of LAO are grown on a TiO_2 terminated STO substrate the interface between them is conducting [103] and superconducting below 300 mK [89].

The polar/non-polar interface causes a potential to grow in the LAO as more layers are added to the structure. At a thickness of 4 uc, electrons from the valence band of the LAO move from the surface to populate the conduction band of the STO at the interface. Electronic reconstruction predicts a population of 1/2 electron per unit cell or $3.2 \times 10^{14}\,\mathrm{cm}^{-2}$ [79]. In reality only about one tenth of the electrons predicted by electronic reconstruction appear in transport measurements [103, 30, 9]. This inconsistency raises some questions about the validity of the electronic reconstruction scenario. Defects, oxygen vacancies, and intermixing may also play a role in generating an electron population at the interface.

Our measurements, discussed in detail in (chapter 4), have helped resolved this open question. Our magnetic susceptibility measurements revealed a paramagnetic

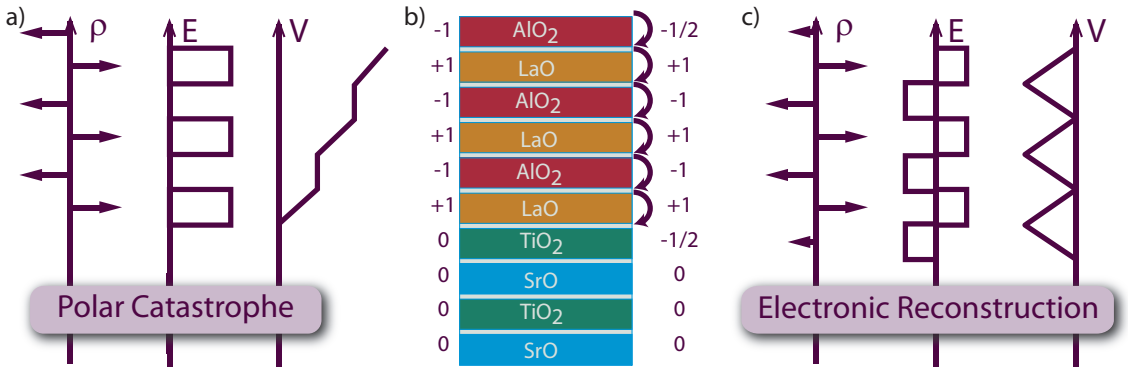

Figure 3.2: a) An electrostatics diagram showing the charge (ρ), electric field (E), and electric potential (V) at each layer in the LAO. The polar catastrophe is the unchecked growth of the internal potential with each additional layer in the LAO. b) Cartoon of the layers in LAO and STO with the charge of each layer before electronic reconstruction labeled on the left and after electronic reconstruction on the right. c) The revised electrostatics diagram after electronic reconstruction. Charge from the surface of the LAO has moved to the interface to balance the potential.

signal with a $1/T$ temperature dependence. This behavior suggested that the paramagnetism is generated by a population of localized electrons. The density of these spins is the correct size to account for the electrons missing from hall effect measurements. Additionally, we believe it is the spatial distribution of these localized electrons that dives the inhomogeneity in the superconducting response discussed in chapter 5.

3.2 Gate tunability

The density of electrons at the LAO/STO interface can be tuned with a back-gate and even driven through a superconductor-insulator transition [30].

Figure 3.3 a) shows the measurement set-up for controlling the carrier density with a back-gate voltage. The data from Caviglia *et.al* is reproduced in Figure 3.3 b-c). The data shows that both the normal resistance and the superconducting critical temperature are modulated by the gate. Moreover, on the underdoped side of the

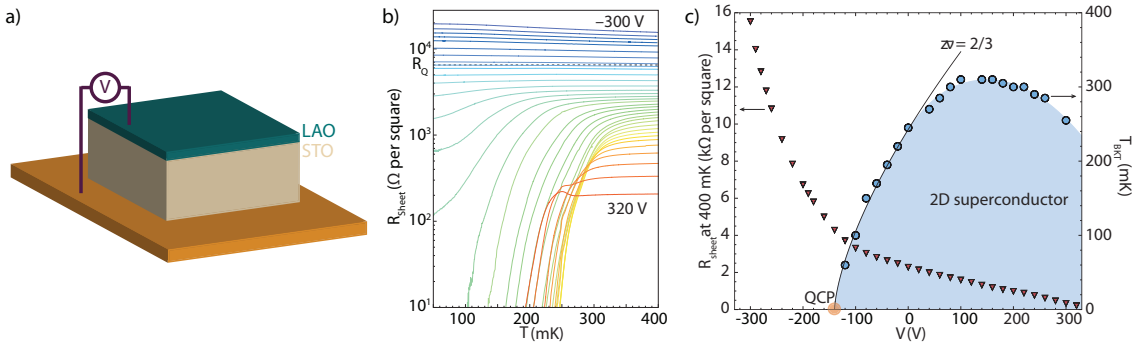

Figure 3.3: a) Cartoon of measurement arrangement. Gate voltage is applied between a metallic back-gate and the conducting interface. b) Resistance vs. temperature curves plotted for various back-gate voltages. c) Critical temperature vs back-gate voltage showing a superconducting dome with a quantum critical point on the underdoped side. b) and c) adapted from [30].

dome (the side with fewer carriers) there is a superconductor-insulator transition and quantum critical point. A quantum critical point is a point at zero temperature where the system can undergo a phase change by tuning a separate physical parameter. In this case tuning the carrier density at zero temperature transitions the systems from a superconductor to an insulator. Figure 3.3 b) shows that the transition in LAO/STO is not quite a superconductor-insulator transition but rather a superconductor-metal transition. An insulator should show a resistance that increases at the lowest possible temperatures. In LAO/STO, even at the lowest gate voltages, the resistance upturn is very weak.

Gate tuning a superconductor-metal transition provides experimentalists with a unique opportunity. Other systems that undergo superconducting transitions usually tune fixed sample parameters such as thickness in amorphous Bi films [69] or chemical doping in the cuprates. In both of these cases a new sample must be grown and measured to map out each point on the dome. The need for multiple samples makes these experiments significantly more difficult. It is comparatively easy to use a gate voltage that can be tuned *in. situ*. Additionally, chemical doping affects both the carrier density and the disorder. A gate voltage more effectively separates these two

effects. In a gate tuned sample the carrier density is modulated by the back-gate but the underlying crystal structure with any associated disorder remains unchanged.

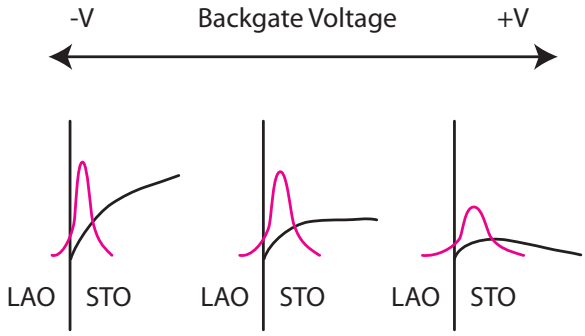

Figure 3.4: Sketch shows the asymmetric potential well confining the electrons at the interface of LAO/STO. The electron wave function is shown in pink. As a more positive gate voltage is applied the electrons are allowed to extend further into the STO.

A caveat to the last statement is the potential well that confines electrons at the LAO/STO interface is asymmetric, Fig. 3.4. Applying a gate voltage to the interface not only changes the number of carriers at the interface, but also changes how far the electrons extend into the STO. The disorder landscape may be different at different depths of the STO crystal. Consequently, the back-gate does change the disorder landscape accessible in the STO, but it will be a much smaller effect than in chemically doped samples.

Given the ease of tuning LAO/STO with a back-gate *in. situ*, we decided to use our scanning SQUID to locally map the evolution of the metal-superconducting transition. Dubi, Meir and Avishai showed, using numerical simulations, that on the insulating side of the transition, superconductivity actually persists in isolated superconducting islands [33]. The diamagnetic susceptibility response from islands should be easily visible to our SQUID even if the islands are sufficiently isolated to prevent a zero resistance state. Searching for these islands or other structure in the superconductor insulator transition was our original motivation for studying the

LAO/STO system. However, our first set of measurements (chapter 4), revealed even more exciting behavior: coexistence of superconductivity and magnetism. Chapter 5 discusses the correlation and interaction between the magnetism and superconductivity, and chapter 6 covers our results from gate tuning the superconducting state of LAO/STO.

3.3 Magnetism in LAO/STO

The original paper showing evidence for magnetism in LAO/STO heterostructures measured magnetoresistance in a series of samples grown in different oxygen partial pressures [22]. The authors found that samples grown at a high oxygen partial pressure ($> 1 \times 10^{-3}$ mbar) showed hysteresis in their magnetotransport characteristics but were not superconducting. Samples grown at a lower oxygen partial pressure between 1×10^{-4} mbar and 3×10^{-5} mbar showed the expected 2D superconducting interface, but no evidence of magnetism in transport.

This result showed that magnetism was possible in LAO/STO. A surprising result in itself since neither LAO or STO are magnetic. However, the magnetism and superconductivity were observed at very different growth conditions and were not show to coexist in a single sample.

Figure 3.5 illustrates why coexistence of superconductivity and magnetism is rare. In the class of superconductors that we understand (BCS Theory), pairs form between electrons with opposite spin. An applied magnetic field is strongly pair-breaking, because it favors one electron spin over the other. In fact superconductors have an upper-critical field beyond which the superconductor cannot survive.

Within a material, ferromagnetism describes the aligning of electron spins to form a bulk magnetic moment. Clearly ferromagnetic order is at odds with conventional BCS pairing. For both of these orders to exist in a single material either we need a new pairing mechanism for the superconducting electrons or the two order must be phase separated. Our SQUID measurements discussing our discovery of coexistence of magnetism and superconductivity are presented in chapter 4.

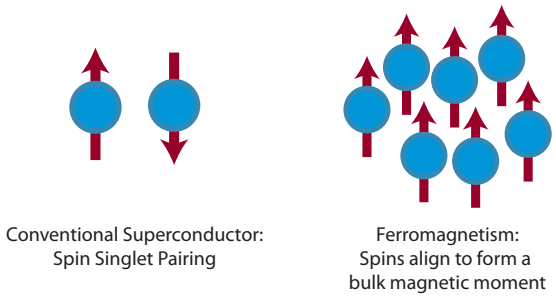

Figure 3.5: Cartoon of electron spin interactions in a conventional (singlet-pairing) superconductor and a ferromagnet. In the superconductor opposite spins pair to form cooper pairs. In a ferromagnet all the spins align to form a bulk magnetic moment. Clearly, a ferromagnetic interaction between electrons will break superconducting pairs.

3.4 δ-doped STO

A second complex oxide system that we studied alongside LAO/STO is δ-doped STO. Doped STO is a well studied bulk superconductor with a very low carrier density [58]. δ-doped heterostructures are grown on an STO substrate. Niobium dopants are confined in a thickness of a few nanometers. Then an STO capping layer is grown on top to protect the doped layer [62].

δ-doped STO heterostructures show 2D superconductivity below 350 mK [62]. Measurements on δ-doped STO serve as a nice comparison to LAO/STO because superconductivity in both systems depends on the population of the STO conduction bands. The difference is that electrons in LAO/STO come from electronic reconstruction rather than dopants. Additionally the potential well confining electrons is symmetric in δ-doped STO and asymmetric in LAO/STO. We compare measurements on LAO/STO and δ-doped STO in chapter 4 and discussion measurement of the penetration depth of δ-doped STO in chapter 7.

Chapter 4

Ferromagnetism and superconductivity

Julie A. Bert, Beena Kalisky, Christopher Bell, Minu Kim, Yasuyuki Hikita, Harold Y. Hwang, and Kathryn A. Moler "Direct imaging of the coexistence of ferromagnetism and superconductivity at the LaAlO3/ SrTiO3 interface" *Nature Physics* **7** 2079 (2011).

4.1 Abstract

$LaAlO_3$ and $SrTiO_3$ are insulating, nonmagnetic oxides, yet the interface between them exhibits a two-dimensional electron system with high electron mobility [79], superconductivity at low temperatures [89, 30, 11, 32, 9], and electric-field-tuned metal-insulator and superconductor-insulator phase transitions [30, 9, 103, 31]. Bulk magnetization and magnetoresistance measurements also suggest some form of magnetism depending on preparation conditions [32, 22, 5, 97] and suggest a tendency towards nanoscale electronic phase separation [5]. Here we use local imaging of the magnetization and magnetic susceptibility to directly observe a landscape of ferromagnetism, paramagnetism, and superconductivity. We find submicron patches of ferromagnetism in a uniform background of paramagnetism, with a nonuniform,

weak diamagnetic superconducting susceptibility at low temperature. These results demonstrate the existence of nanoscale phase separation as suggested by theoretical predictions based on nearly degenerate interface sub-bands associated with the Ti orbitals [85, 82]. The magnitude and temperature dependence of the paramagnetic response suggests that the vast majority of the electrons at the interface are localized [98], and do not contribute to transport measurements [30, 9, 103]. In addition to the implications for magnetism, the existence of a 2D superconductor at an interface with highly broken inversion symmetry and a ferromagnetic landscape in the background suggests the potential for exotic superconducting phenomena.

4.2 Indroduction

Coexistence of ferromagnetism and superconductivity in nature is rare [4, 92, 24, 25, 102]. The $LaAlO_3/SrTiO_3$ interface is a new system for studying this coexistence. $LaAlO_3$ (LAO) and $SrTiO_3$ (STO) are both perovskite band insulators with no magnetic order in their bulk form. For LAO grown on the TiO_2 terminated STO substrate, a high mobility electron gas was observed at the interface [79]. Electronic reconstruction, driven by the polar/nonpolar interface, is thought to move charge from the LAO layers across the interface into the STO causing an effective electronic doping responsible for the observed conductivity [79]. The interplay of this effect with oxygen vacancies and structural changes [46], and the relative contribution of these three effects to the carrier concentration, remains a subject of debate. Significant variability in the physical properties in similar samples indicates that the ground state of this interface system is sensitive to small changes in growth conditions. Superconductivity [89, 30, 11, 32] and features interpreted as interface magnetism [32, 22, 5] have been independently observed at the LAO/STO interface via transport and bulk magnetization measurements. One recent study inferred the existence of both ferromagnetism and superconductivity in the same sample from hysteresis in magnetoresistance transport measurements [32].

4.3 Experiment

We use a scanning superconducting quantum interference device (SQUID) with micron-scale spatial resolution to image three samples down to 20 mK (See methods). Our SQUID sensor can concurrently measure the static magnetic fields generated by the sample (magnetometry) and the susceptibility of the sample to a small locally applied ac magnetic field (susceptometry). Fig 1 a&b show magnetometry and susceptometry images of an LAO/STO interface. The ferromagnetic landscape appears as many static spatially separated dipoles that show no temperature dependence over the measured temperature range. The superconductivity is spatially inhomogeneous and weak, with a critical temperature $T_c = 100$ mK (Fig 1c), above which a temperature-dependent paramagnetic response is apparent (Fig 1c inset). In contrast, a delta-doped STO sample [62] has relatively uniform 2D superconductivity, no magnetic order, and no apparent paramagnetic response above Tc (Fig 1d,e,&f), although the expected paramagnetic signal at $T_c = 300$ mK is close to our noise floor.

The diamagnetic susceptibility from the LAO/STO interface is an order of magnitude smaller than that of the delta-doped $SrTiO_3$ or $(Ba_{0.9}Nb_{0.1}CuO_{2+x})_m/(CaCuO_2)_n$, another two-dimensional superconductor [100]. The susceptometry signal is generated by superconducting electrons which screen the local applied field and is related to the local density of electrons in the superconducting condensate. The superfluid density is usually quantified by the magnetic penetration depth, λ [71, 42]. In a 2D superconductor with thickness $d \ll \lambda$, the screening currents are confined in the vertical direction which generates a modified penetration depth known as the Pearl length, $\Lambda = 2\lambda^2/d$. The low temperature Pearl length in the delta-doped STO sample was 650 μm based on fits to formulas for the height dependence of the susceptometry from references [42, 56]. This formula should not quantitatively describe the data for the LAO/STO interface due to the lateral inhomogeneities, but the susceptibility signal from a uniform 2D superconductor scales as $1/\Lambda$ for large Λ, implying an ~ 8 mm Pearl length in the LAO/STO.

The T_c variation between two measurement positions on the LAO/STO sample

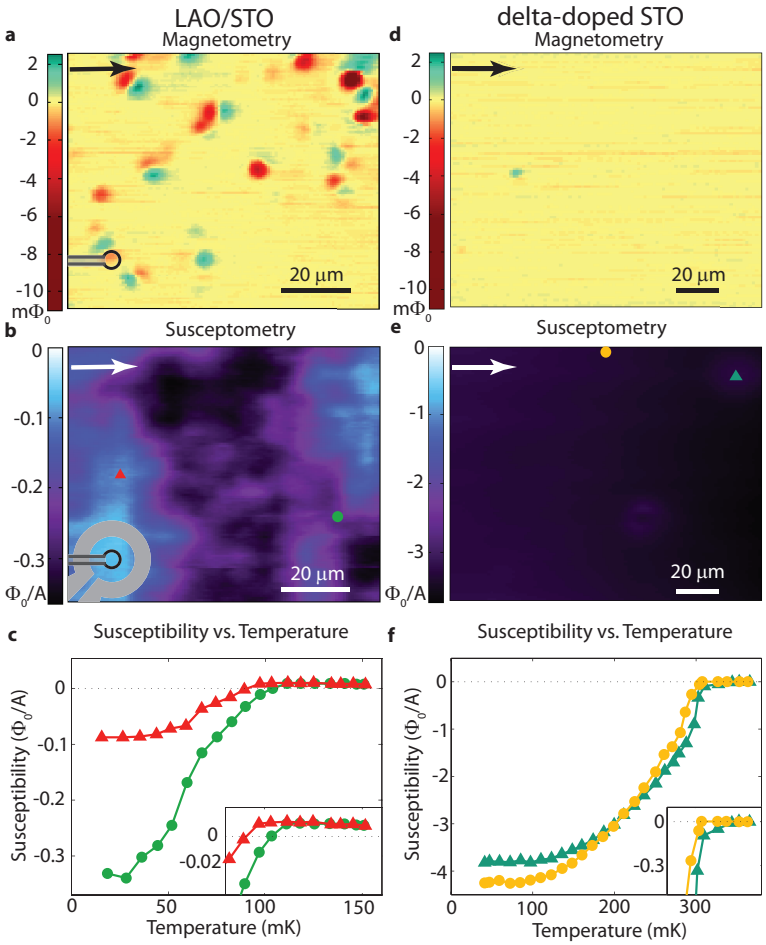

Figure 4.1: Comparison of SQUID images on LAO/STO and delta-doped STO samples. **a,** LAO/STO magnetometry image mapping the ferromagnetic order. Inset, scale image of the SQUID pick-up loop used to sense magnetic flux. **b,** LAO/STO susceptometry image mapping the superfluid density at 40 mK. Inset, scale image of the SQUID pick-up loop and field coil. **c,** The temperature dependence of the susceptibility taken at the two positions indicated in **b**. **d,** delta-doped STO magnetometry image showing no ferromagnetic order. **e,** delta-doped STO susceptometry image mapping the superfluid density at 82 mK. **f,** The temperature dependence of the susceptibility taken at the two positions indicated in **e**. The arrow on each scan shows the scan fast axis and the SQUID orientation.

(Fig 1c) is about 10%. However, the lateral variation of the susceptometry is large: 84% of the total response, compared to just 12% in the delta-doped STO, and less

than 1% in most bulk superconductors [51]. The largely inhomogeneous superconducting and ferromagnetic response may suggest proximity to a first order phase transition. Although both magnetism and superconductivity are present at the interface in the LAO/STO sample, Fig 1 a&b do not show a direct correlation between the inhomogeneity of the superconducting state and the distribution of magnetic regions.

The ferromagnetism appears as magnetic dipoles in Fig 1a and Fig 2a, mostly separated from each other by microns, with many additional dipoles that do not show up visually in these images but are still above our noise threshold (Fig 2a insets). We analyzed six 70x80 micron high resolution magnetometry scans, including the one shown in Fig 2a, finding 144 dipoles above our noise floor and fitting each one to a point dipole model to determine its total moment and orientation (Fig 2b-d). The histogram of the dipole moments shows a clear exponential distribution of dipole moments with a few large ($\sim 1 \times 10^8\,\mu_B$) dipoles and substantially more smaller dipoles down to the limit of our noise. This trend suggests that there are even more dipoles with moments below the sensitivity of our SQUID.

Most of the dipoles lie in plane, as expected from the shape anisotropy of the interface, with apparently randomly distributed azimuthal angles indicating no alignment or net magnetization. This observation is consistent with cooling the sample in zero field. The point dipole approximation is not as good for some dipoles, particularly the ones with the largest moments, indicating that they are not point-like but are instead ferromagnetic patches that extend over an area comparable to the SQUID's $3\,\mu$m pick-up loop. The dipoles were stable throughout the duration of the cooldown (about 1 month) and were insensitive to temperature changes from 20 mK through the superconducting critical temperature and up to 4.2 K. Additional SQUID measurements in a separate variable temperature cryostat showed that the dipole size and orientation remained unchanged between 4.2 K and our maximum measurement temperature of 60 K. In addition, we measured a second sample with 10 uc of LAO grown on a TiO_2 terminated surface that had patterned Hall bars (Methods). This second 10 uc LAO/STO sample had many fewer dipoles - none in some regions. The

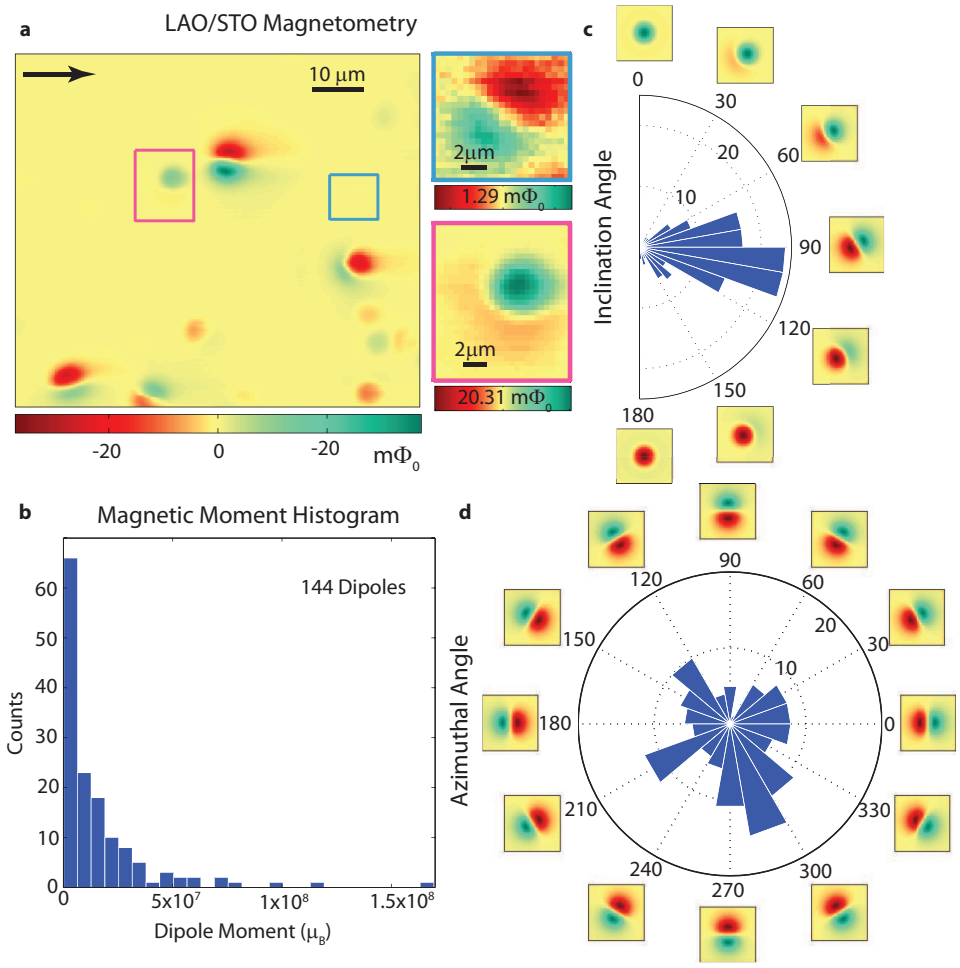

Figure 4.2: Analysis of the dipole distribution. **a,** Magnetometry scan showing ferromagnetic dipoles. The arrow shows the scan fast axis and the SQUID orientation. Insets: Individual dipoles from the areas indicated in the larger image. **b-d,** Histograms of the moment and orientation of 144 dipoles taken from six large area scans similar to the one show in panel **a**. **b,** The magnetic moment of each dipole in Bohr magnetons, μ_B. **c,** The inclination angle from the normal to the sample surface (an inclination angle of 90 degrees mean the dipole lies in the plane of the interface). **d,** The azimuthal angle with respect to the scan's x-axis.

variability in the size of the moment may be related to the variability of physical properties in nominally identical samples in this system.

We did not observe dipoles in the magnetometry signal on the delta-doped STO

sample (Fig 1d). Since both the delta-doped STO sample and the LAO/STO samples use the same commercially available STO substrates, the absence of dipoles on the delta-doped STO sample rules out magnetic impurities in the substrate. This observation is corroborated by the scan height extracted from the dipole fits indicating the dipoles are within a few microns of the surface.

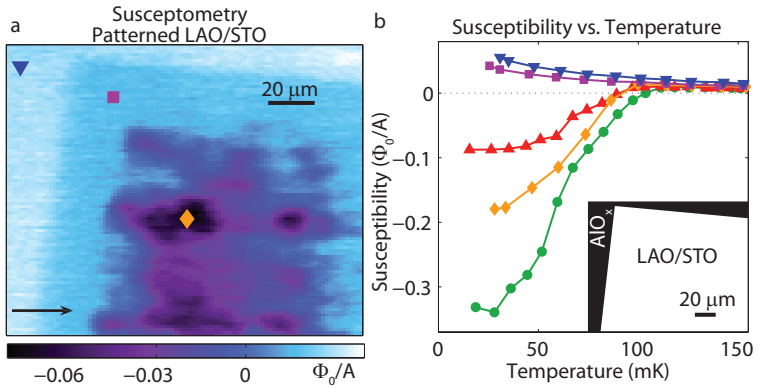

Figure 4.3: Paramagnetic signal on patterned LAO/STO sample. **a,** Susceptometry scan on the patterned sample at 87 mK. A suppression of the diamagnetic susceptibility is visible near the edge of the pattern. The susceptibility response in this area has a paramagnetic sign as indicated in the susceptibility vs. temperature plot. The arrow indicates the scan fast axis and the SQUID orientation. **b,** Susceptibility vs. temperature data from three positions on the patterned LAO/STO shown in panel **a**. The red triangles and green circles are data reproduced from the unpatterned LAO/STO sample show in Fig 1a. Inset: The outline of the AlO_x patterning associated with the susceptometry scan.

In addition to the ferromagnetic order, the two LAO/STO samples measured at low temperature show paramagnetism above the superconducting critical temperature T_c (Fig 1c inset, Fig 3). In the case of the patterned LAO/STO sample, which did not show many ferromagnetic dipoles, we observe regions near the hall bar edges where the superconductivity was suppressed and the paramagnetism remains down to the lowest measured temperatures. The paramagnetic signal decreases with increasing temperature suggesting a Curie law. The $1/T$ dependence and the paramagnetic sign indicate that the susceptibility signal originates from localized spins.

We can estimate the electron density associated with the ferromagnetic, diamagnetic, and paramagnetic signals. We determine the number of ferromagnetic electrons by adding the moments of all the dipoles in the histogram yielding $7.3 \pm 3.4 \times 10^{12}\,\mu_B/\mathrm{cm}^2$. This estimate is a lower bound, because any dipoles that are below the sensitivity of our sensor or whose moments canceled due to the random distribution of alignments have not been included in this total. We use the Pearl length to find the density of superconducting electrons,

$$n_s = \frac{2m^*}{\mu_0 e^2 \Lambda}, \tag{4.1}$$

where e is the elementary charge and μ_0 is the permeability of free space. Using $m^* = 1.45\,m_e$ [29] we find $n_s \approx 1 \times 10^{12}\,\mathrm{cm}^{-2}$ in the regions of high superfluid density and $n_s \approx 3 \times 10^{11}\,\mathrm{cm}^{-2}$ in the regions of low superfluid density. We quantify the paramagnetic signal by using an appropriate model for our sensor to convert our measured susceptibility, ϕ, to the dimensionless susceptibility, χ, for a layer of spins in a thickness d. Using $\chi d = 22\mu\mathrm{m} \cdot \mathrm{mA}/\Phi_0 \cdot \phi$ [18] and comparing χ to the Curie expression,

$$\chi = \frac{\mu_0 n_{3\mathrm{D}} (g\mu_B)^2 J(J+1)}{3k_B T} \tag{4.2}$$

with $g = 2$ and $J = 1/2$, yields a 2D spin density of $4.4 \times 10^{14}\,\mathrm{cm}^{-2}$, with large error bars due to uncertainty in the geometrical parameters. We compare our estimates with the electron densities predicted by the polar catastrophe, $3 \times 10^{14}\,\mathrm{cm}^{-2}$, and seen in hall measurements [30, 9, 103], $1 - 4 \times 10^{13}\,\mathrm{cm}^{-2}$ (Table 1). The densities of magnetic and superconducting electrons are respectively one and two orders of magnitude lower than the polar catastrophe density, but the paramagnetic spin density shows surprising agreement within error.

Density functional calculations of the electronic structure in LAO/STO predict the presence of multiple nearly degenerate subbands that result in separate charge carriers [85]. Magnetism was also predicted at the n-type LAO/STO interface from

	LAO/STO			δ-Doped STO
	Literature	Unpatterned	Patterned	Unpatterned
Polar Catastrophe[79]	3.2×10^{14}	-	-	-
Hall Effect[30, 9, 103]	$1 - 4 \times 10^{13}$	-	-	4.7×10^{13} [[62]]
Paramagnetic	-	$1 - 5 \times 10^{14}$	$1 - 5 \times 10^{14}$	-
Dipole Moment (μ_B)	-	$0.4 - 1.1 \times 10^{13}$	$< 2 \times 10^{11}$*	$< 1 \times 10^{11}$*
Superfluid Density	-	$0.3 - 2 \times 10^{12}$	$0 - 1 \times 10^{12}$	$1 - 1.4 \times 10^{13}$

* Dipoles were too sparse and inhomogeneously distributed to extract a statistically significant areal density.

Table 4.1: Table of electron densities. Electron densities extracted from hall measurements, and measurement of the ferromagnetic, superconducting and paramagnetic signals for all three samples. All quantities given in cm^{-2}. The gray shaded area indicates electron quantities accessible with our scanning SQUID technique. The - symbol means that measurement is not applicable.

alignment of additional electrons in the Ti orbitals [82]. Transport measurements, which probe delocalized electrons, have measured electron densities significantly lower than predictions from the polar catastrophe. Our measurements indicate that those missing electrons may be present but localized, and contribute to the magnetic signal.

The observation of ferromagnetism and superconductivity at the LAO/STO interface opens exciting possibilities for studying the interplay of these normally incompatible states. Tuning the carriers with a gate voltage may add even more richness to the system, by coincidentally studying how adding or removing carriers affect the superconducting, ferromagnetic and paramagnetic signals.

4.4 Methods

The two LAO/STO samples used in the low temperature study were prepared by growing 10 unit cells of $LaAlO_3$ on commercial TiO_2 terminated 001 STO substrates. The patterned sample had an AlO_x hard mask which defined hall bars. The $LaAlO_3$

was deposited at 800°C with an oxygen partial pressure of 10^{-5} mbar, after a pre-anneal at 950°C with an oxygen partial pressure of 5×10^{-6} mbar for 30 minutes. The samples were cooled to 600°C and annealed in a high pressure oxygen environment (0.4 bar) for one hour [9].

A delta-doped STO sample was also studied at low temperatures. It was grown in an atmosphere of less than 10^{-8} torr oxygen at 1200°C. Nb dopants were confined to a 5.9 nm layer and additional 100 nm cap and buffer layers of STO were grown above and below the doped region. The sample was annealed in situ at 900°C under an oxygen partial pressure of 10^{-2} torr for 30 minutes [62].

Measurements were done by scanning SQUID in a dilution refrigerator [44, 17]. The SQUID has a 3 μm pick-up loop, centered in a single turn field coil. Static magnetism (magnetometry) in the sample is probed by recording the flux through the SQUID pick-up loop as a function of position. Applying an ac current in the field coil produces a local magnetic field. The local susceptibility (susceptometry) of the sample to the applied field is detected by the pick-up loop in a lock-in measurement.

Chapter 5

Correlating magnetism and superconductivity

Given the surprising discovery of coexisting superconductivity and magnetism in LAO/STO, a natural follow-up question is how does the magnetism affect the superconductivity? Specifically, is the large inhomogeneity observed in the samples presented in the previous chapter due to the magnetic fields generated by the localized ferromagnetic moments?

5.1 Dipole fields

The first step in answering these questions is to model the magnetic fields near a ferromagnetic patch and compare it to the upper critical field of LAO/STO. We start this process by making some simple assumptions about the density and geometry of the ferromagnetic patches.

We assume a moment density of $1\,\mu_B$ per unit cell. This is a natural assumption because undoped STO has an empty d-shell. When STO is doped, either by dopants or through electronic reconstruction driven by the LAO, electrons enter the d-shell. Electronic reconstruction predicts that electrons from the valence band of LAO will populate the conduction band of STO at a density of 1/2 electron per unit

cell. Because the magnetism forms sporadic magnetic patches rather than producing a smooth magnetic background the moments cluster and form patches of ferromagnetism. We assume this clustering results in a local density of $1\,\mu_B$ per unit cell.

Fitting the moments in our magnetometry images yields the total magnetic moment of each individual ferromagnetic patches. A histogram showing a typical distribution of magnetic moments was plotted in the previous chapter in Figure 4.2. A more exhaustive study of the size and density distribution of magnetic patches in 14 LAO/STO heterostructures with different LAO thicknesses was done by Kalisky [50]. From these measurements we find that the total moment of the individual ferromagnetic patches varies between 10^6-$10^8\,\mu_B$. There are almost certainly smaller moments but their signal is below our measurement noise.

Knowing the total moment size and density we can now make assumptions about the shape and position of the ferromagnetic patches. We will investigate two cases: spherical regions and cylindrical regions. Using the moment density, total moment, and shape we can determine the size of a magnetic region. For example, a spherical dipole with $10^7\,\mu_B$ with have a radius of 52 nm. If instead the dipole was a cylinder with a thickness of just one unit cell of LAO the radius would be $0.7\,\mu$m. Given the 2D-nature of the interface, magnetic cylinders are the only option if we assume the entire magnetic patch exists only in the LAO layer.

We now calculate the magnetic field outside each of these shapes. The spherical case is simple. The magnetic field outside a uniformly magnetized sphere is identical to the field profile of a point dipole with the same magnetic moment.

$$\vec{B}(\vec{r}) = \frac{\mu_0 M}{4\pi}\frac{1}{|r|^3}(3(\hat{r}\cdot\hat{m})\hat{r} - \hat{m}) \tag{5.1}$$

μ_0 is the permeability of free space, M is the total magnetic moment in Bohr magnetons, $\hat{m}$ is the direction of the magnetic moment, and $\vec{r}$ is the vector connecting the magnetic moment to the point in space where we want to know $\vec{B}$.

For a cylinder we start from the magnetic scalar potential, ϕ. In the limit where

the cylinder thickness approaches zero,

$$\phi(\rho, \varphi, z) = \frac{M}{\pi R} \cos\varphi \int_0^\infty e^{-kz} J_1(kR) J_2(k\rho) dk. \tag{5.2}$$

R is the cylinder radius, ρ, φ, and z are the position in cylindrical coordinates. We numerically calculate the magnetic field from the gradient of the potential, $\vec{B} = -\mu_0 \vec{\nabla}\phi$. The field profile of each structure is plotted in Figure 5.1.

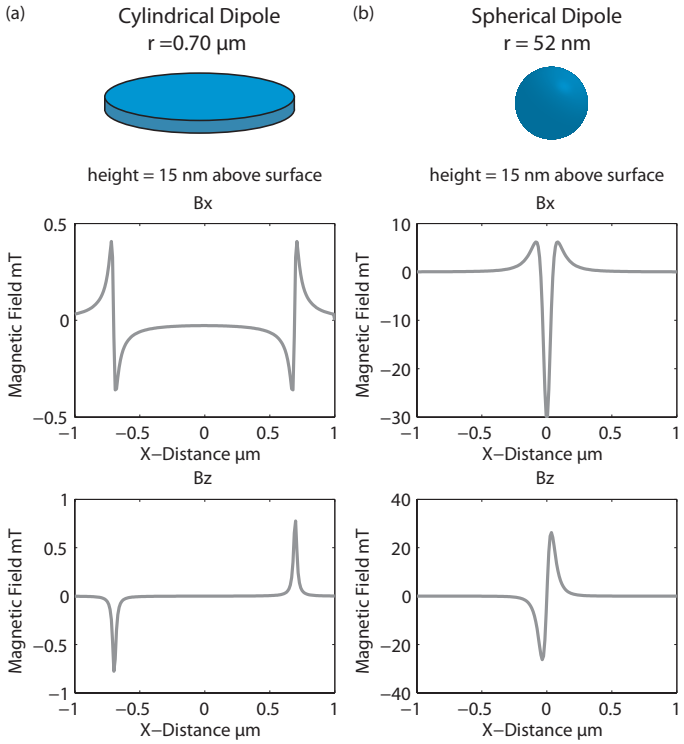

Figure 5.1: Field profiles in the x and z-direction at a height of 15 nm above the top surface for a cylindrical dipole (a) and a spherical dipole (b) with bulk magnetization in the x-direction.

The spherical dipole arrangement seems an unlikely candidate for describing the magnetism in LAO/STO. A moderately sized dipole with $10^7\,\mu_B$ has a diameter of 100 nm. For 10 uc of LAO grown on STO, the LAO is just 4 nm thick. Consequently a spherical dipole would need to extend deep into the STO. Since bulk STO is not magnetic, and the superconducting electrons penetrate just 10 nm into the STO, it seems

unlikely that the magnetism could penetrate 100 nm into the STO. Consequently, we conclude thin cylindrical patches are a more likely candidate for the shape of the magnetism.

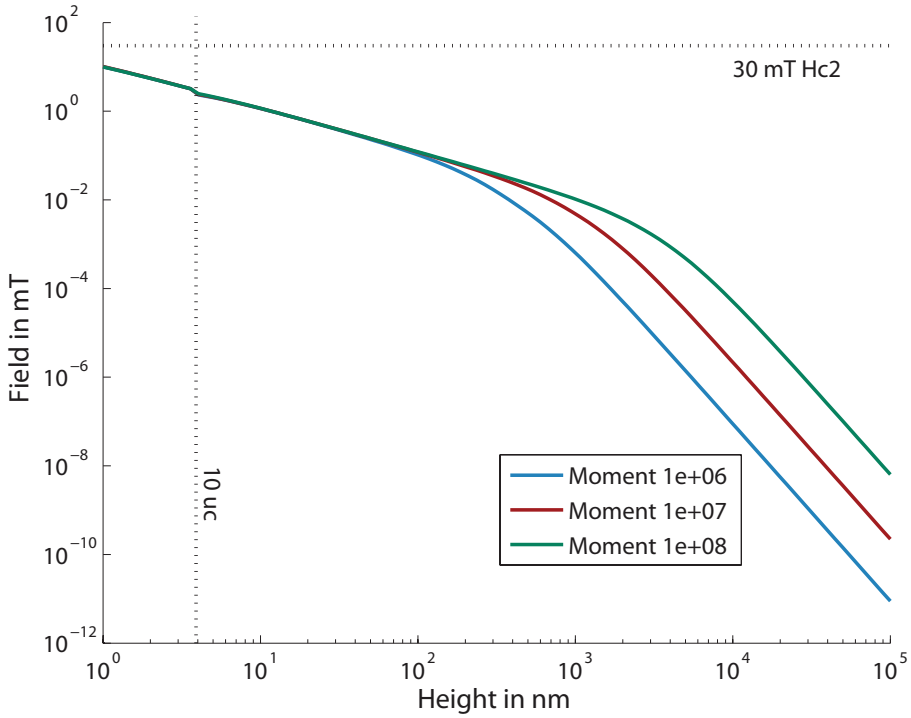

Figure 5.2: Height dependence of the maximum field in the z-direction outside a thin cylindrical dipole.

Figure 5.2 plots the height dependence of the maximum field in the z-direction for three thin cylindrical dipoles, with different total moments oriented in the x-direction. We are most concerned with the field in the z-direction because the perpendicular critical field is much smaller than the parallel critical field for a 2D superconductor. Figure 5.2 shows that for a height, h, much smaller than the radius, R, the dipole radius (determined by the dipole moment) has no influence on the peak field strength. The magnetic patch looks like an infinite plane. As long as the moment density remains $1\,\mu_B$/uc, 10 mT is the largest possible field a 1 uc thick cylindrical dipole can produce. Moving away from the patch the field decays as $1/h$ until a cross-over point

Thickness	T_c	HcII(T=0)	Reference
8 uc	0.20 K	60 mT	Reyren [89]
15 uc	0.10 K	30 mT	Reyren [89]
4 uc	0.20 K	80 mT	Reyren [88]
10 uc	0.13 K	70 mT	Dikin [32]

Table 5.1: Table of critical fields in LAO/STO.

at $h \sim R$ where the patch resembles a point dipole and the field decays as $1/h^3$.

The upper critical field of LAO/STO has been measured by many groups using transport techniques. The results are summarized in Table 5.1. The maximum field we found for 2D magnetic patches, 10 mT, is well below the reported critical fields. Consequently, we do not expect the magnetic patches to significantly suppress the superconductivity. Thus the magnetic patches are not the main source of the inhomogeneity.

Do we see this trend in the data? Figure 5.3(a) shows a magnetometry scan and two susceptibility scans of the same region on a 5 uc LAO/STO heterostructure. The susceptibility image on the left was taken above T_c and the susceptibility image on the right was taken below T_c, $T_c \approx 200$ mK. The largest two dipoles, labeled dipole 1 and dipole 2, are clearly visible in both susceptibility images. However, the visible response is due the paramagnetic signal from each of the dipole moments, not suppression of the superconducting signal by a magnetic dipole field.

Line cuts in x and y from the two susceptibility images reveal the same susceptibility profile in both images, above and below T_c. The paramagnetic response from a ferromagnetic patch is temperature independent and sits on top of the superconductivity. This means that visible suppression of the superconductivity due to the magnetic patch is caused by it's paramagnetism, and not by the dipole's local magnetic field. This observation is consistent with the low dipole fields we expect from the cylindrical dipole configuration. The dipole fields are not influencing the superconductivity.

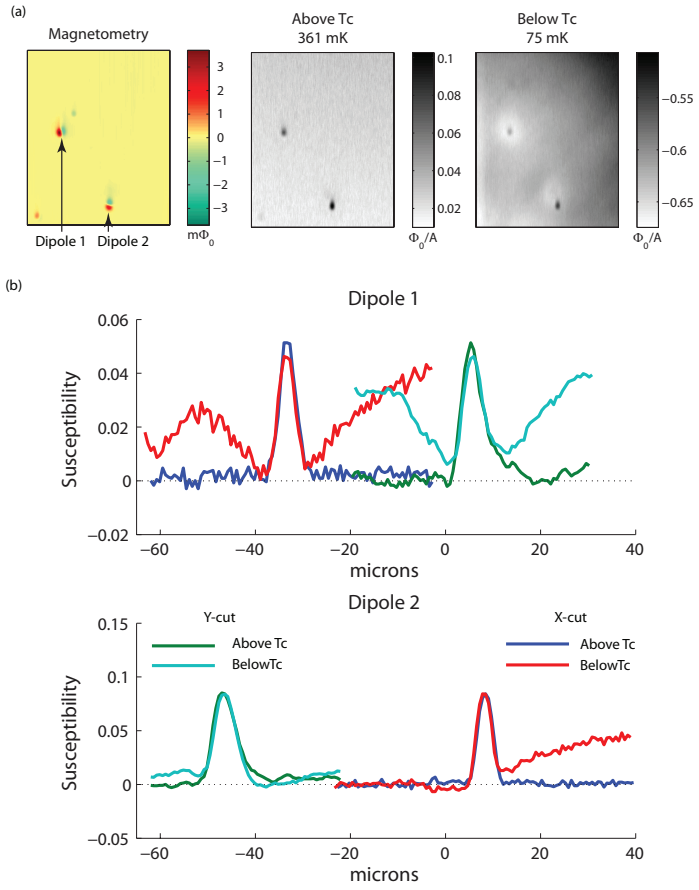

Figure 5.3: (a) Magnetometry and susceptometry images on the same region of a 5 uc LAO/STO heterostructure. (b) Line-cuts in the x and y-direction near each dipole in the two susceptibility images.

5.2 Paramagnetism and superconductivity

It seems unlikely that the magnetic patches are responsible for the inhomogeneity in the superconductivity. The fields generated by the patches are too small to have a significant influence on the superconducting state. Instead, we propose that the inhomogeneity is driven by an underlying paramagnetic landscape of localized spins that are not related to the ferromagnetic patches. This paramagnetic landscape was introduced in the previous chapter as the source of the electrons missing from transport measurements.

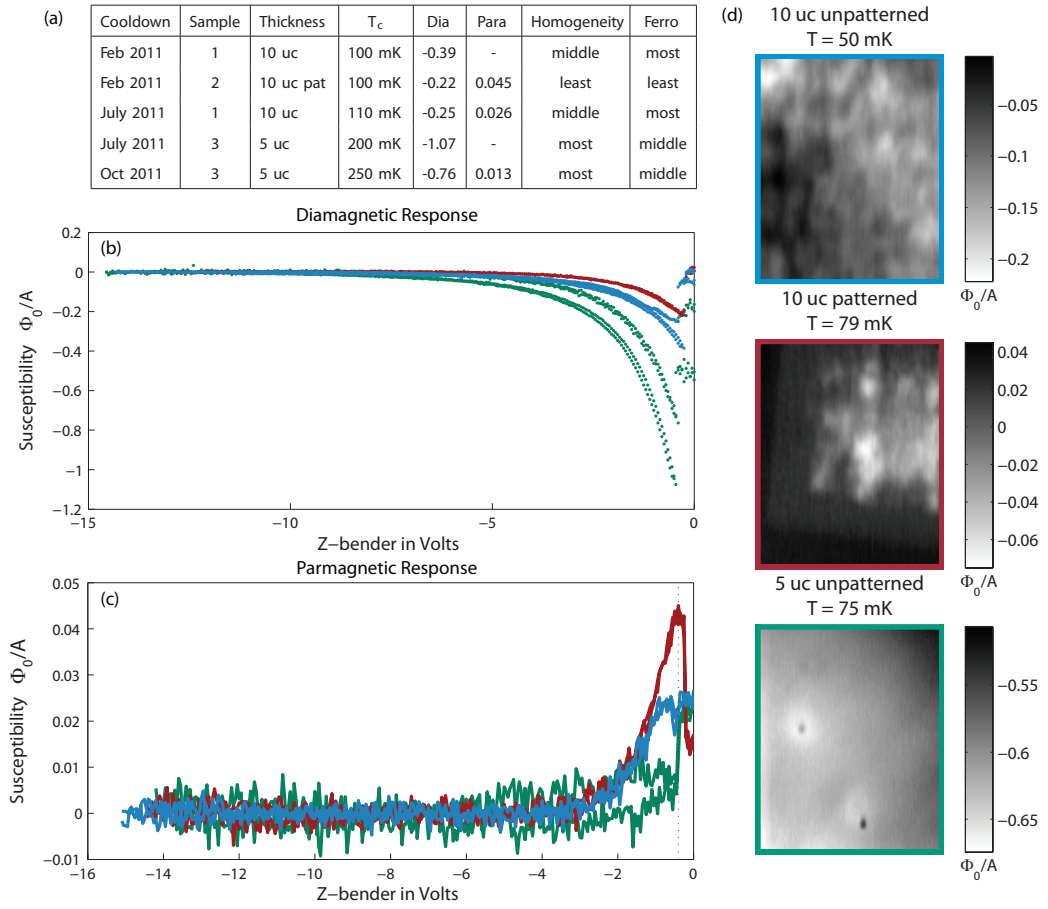

Cooldown	Sample	Thickness	T_c	Dia	Para	Homogeneity	Ferro
Feb 2011	1	10 uc	100 mK	-0.39	-	middle	most
Feb 2011	2	10 uc pat	100 mK	-0.22	0.045	least	least
July 2011	1	10 uc	110 mK	-0.25	0.026	middle	most
July 2011	3	5 uc	200 mK	-1.07	-	most	middle
Oct 2011	3	5 uc	250 mK	-0.76	0.013	most	middle

Figure 5.4: Three samples were measured over the course of three cooldowns. Two of the samples were measured twice and their properties changed between cooldowns. (a) Table of sample properties and how they changed between cooldowns. (b) Low temperature diamagnetic response of the three samples. Samples 1 & 3 were less diamagnetic and had a higher critical temperature the second time they were measured. (c) Low temperature paramagnetic response with the superconductivity suppressed by a gate or patterning. The dotted black line indicates when the SQUID made contact with the sample. Low temperature paramagnetic measurements were not possible in the other two situations because the paramagnetic signal was masked by the superconductor. (d) Susceptibility scans showing varying levels of inhomogeneity.

To fully explore the effect of paramagnetism on the superconductivity we will review data from three different samples measured in three different cooldowns. A summary of the samples is given in Figure 5.4.

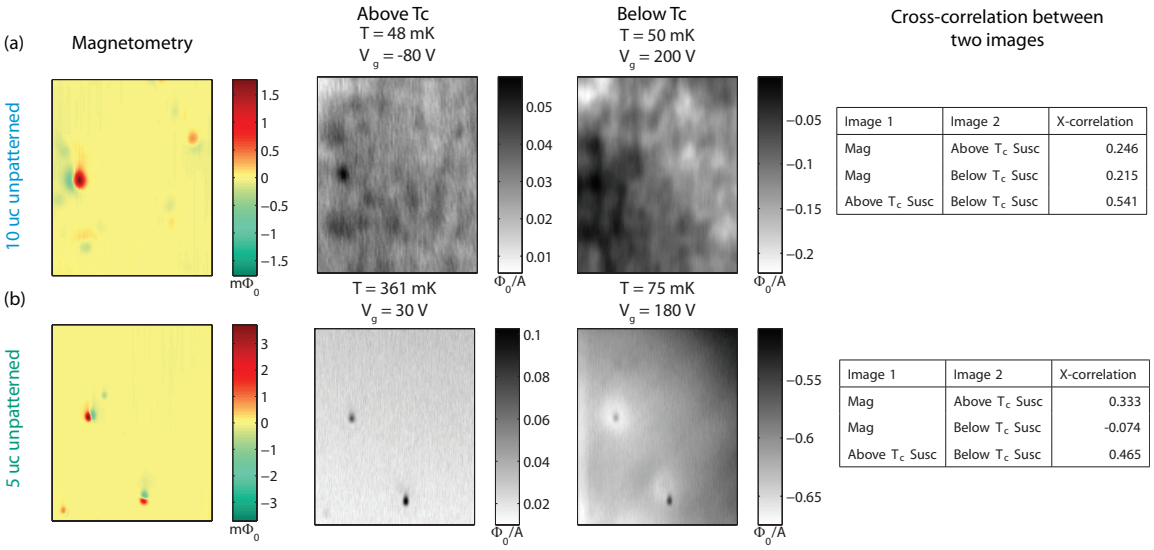

Figure 5.5: Magnetometry and susceptometry scans above and below T_c in the unpatterned 5 and 10 uc samples. The cross-correlation is calculated for each pair of images. (a) The features in the paramagnetic landscape match the diamagnetic landscape. (b) The only the dipole paramagnetism matches.

At this point we have now discussed two different paramagnetic signals. The paramagnetism from individual ferromagnetic patches, which is temperature independent and correlated to individual dipoles and the paramagnetic landscape which has a $1/T$ temperature dependence and is not readily correlated with the ferromagnetic patches. Figure 5.5(a) shows that it is the paramagnetic landscape (visible in the Above T_c image) that is correlated with inhomogeneity in the superconducting state (the Below T_c image). In Figure 5.5(b) the superconductivity is much smoother and the only residual paramagnetism above T_c is correlated with individual dipoles.

We have also calculated the cross-correlation for each pair of images in the set. The cross-correlation number is 1 if the images are identical and -1 if one image is the negative of the other. A 0 value indicates the images are uncorrelated with no shared features. The two susceptibility images in (a) are more correlated with each other than the dipole image.

The data presented in Figure 5.5 is not complete. Ideally we would have 3 susceptometry images: above T_c but still at low T using a large negative gate voltage, above T_c at high T, and below T_c at low T. Such a set would be useful for testing the temperature dependence of the paramagnetic landscape. From touchdown curves plotted in Figure 4.3 we have shown that the paramagnetic signal follows a $1/T$ temperature dependence and is barely detectable above 100 mK.

Missing from Figure 5.5(a) is the high temperature paramagnetic image on the 10 uc sample. At high temperatures, we expect the inhomogeneity to disappear leaving only the paramagnetism from a few temperature independent dipoles. Indeed we observe that the inhomogeneity disappears above T_c at elevated temperatures in a separate set of images taken on the same sample in a different location.

Figure 5.5(b) is missing a low temperature paramagnetic image. We expect that image to be smooth without any inhomogeneity to match the smooth diamagnetic image. In a separate cooldown with a larger back-gate we were able to capture a low temperature image above T_c and found it was homogeneous as expected. (See Figure 6.4(a) in the following chapter).

From these observations, we conclude that the inhomogeneity in the superconducting signal is driven by an underlying inhomogeneous paramagnetic background. Moreover, the superconducting inhomogeneity does not result from adding an inhomogeneous paramagnetic signal on a top of a smooth diamagnetic signal. Unlike the case presented in Figure 5.3, where the dipole paramagnetism was visible on top of the superconductivity signal with no additional interaction, in this case the relative scales of the two signals exclude simple addition. Instead, the presence and density of localized paramagnetic spins is interacting with and suppressing the superconducting signal.

5.3 Other sources of inhomogeneity

We have observed another sources of inhomogeneity that is not related to either the ferromagnetic patches or the paramagnetic landscape. Halo shapes, of similar size to

the SQUID's field coil, appear when scanning at temperatures within $\sim 50\%$ of T_c. Their presence is unrelated to the superfluid density.

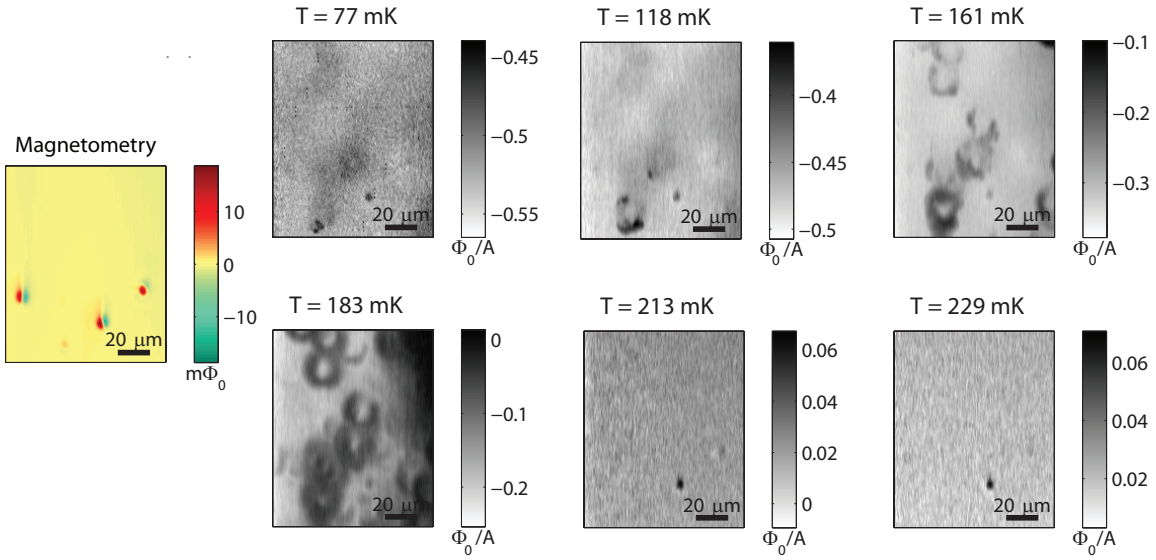

Figure 5.6: A temperature sequence of susceptibility images on the same area of the 5 uc sample. The magnetometry scan on the left shows that the halo defects are not related to the ferromagnetic patches.

Figure 5.6 shows a temperature sequence of susceptibility scans on the same area of the 5 uc sample. The halos are only visible at higher temperatures closer to T_c and disappear above T_c. The size and shape of these features suggests they are are related to the field coil, as demonstrated by Figure 5.7. A defect that responds strongly when the field coil is directly above it will show a ring of suppression the size and shape of the field coil.

5.4 Conclusions

We have identified three mechanisms that affect the inhomogeneity of the superconducting state of LAO/STO. 1) Localized, temperature independent paramagnetism from the ferromagnetic patches which add a paramagnetic bump on top of the superconducting signal. 2) A landscape of paramagnetism generated by localized spins

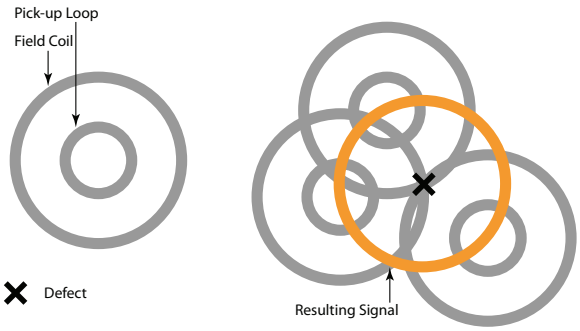

Figure 5.7: A cartoon demonstrating the signal (shown in orange) produced by a point-like defect that interacts strongly with the field coil.

with a 1/T temperature dependence. 3) Point like defects that interact strongly with the field coil to create halos of reduced superfluid density. These halo features only appear at temperatures $> 0.5T_c$.

The paramagnetic landscape has the largest impact on the homogeneity. Samples that were less paramagnetic were also more homogeneous. Further experiments are necessary to elucidate the nature of the interaction between the paramagnetic localized electrons and the superconducting electrons. However, it may be related to the suppression of superconductivity observed along the edges of the patterned sample, Figure 4.3.

Chapter 6

Gate tuned superconductivity

Submitted to PRB.

Julie A. Bert, Katja C. Nowack, Beena Kalisky, Hilary Noad, J ohn R. Kirtley, Chris Bell, Hiroki K. Sato, Masayuki Hosoda, Yasayuki Hikita, Harold Y. Hwang, and Kathryn A. Moler

"Measurements of the gate tuned superfluid density in superconducting $LaAlO_3/SrTiO_3$"

6.1 Abstract

The interface between the insulating oxides $LaAlO_3$ and $SrTiO_3$ exhibits a superconducting two-dimensional electron system that can be modulated by a gate voltage. While gating of the conductivity has been probed extensively and gating of the superconducting critical temperature has been demonstrated, the question whether, and if so how, the gate tunes the superfluid density and superconducting order parameter is unanswered. We present local magnetic susceptibility, related to the superfluid density, as a function of temperature, gate voltage and location. We show that the temperature dependence of the superfluid density at different gate voltages collapse to a single curve characteristic of a full superconducting gap. Further, we show that the spontaneous dipole moments observed in this system are not modulated by the gate voltage.

6.2 Text

Electric field control of conducting channels has allowed great innovation in traditional semiconductor devices [1]. Now heterointerfaces in a new class of materials, the complex oxides, have generated significant interest because of their gate tunable properties. Specifically, the conducting interface formed between the band insulators lanthanum aluminate and TiO_2 terminated 100 strontium titanate (LAO/STO) [79] exhibits many fascinating properties [94] suggesting that an electronic reconstruction triggered by the polar/non-polar interface plays an important role in the inducing the conductivity in the STO [77]. At low temperatures this interface displays two-dimensional superconductivity [89]. Additionally, the high dielectric constant of STO at low temperatures [91] makes applying an electric field with a back-gate especially effective to tune the properties of this superconducting state.

Caviglia *et al*. showed that with increasing gate voltage, V_g, the superconducting critical temperature, T_c, displayed a dome structure and concurrently the normal state resistance monotonically decreased [30]. Later work showed that the electron mobility and carrier density both increased continuously with V_g, with the former dominating the V_g dependence of the conductivity[9]. The evolution of a non-linearity in the Hall resistivity as a function of V_g [9, 11] has been interpreted by Joshua *et al*. as evidence of electrons populating conduction bands with different mobilities [49], implying that the ratio of high and low mobility electrons may be tuned by gating.

Notably, the interface breaks spatial inversion symmetry, opening the possibility for spin orbit coupling to impact the electronic properties of the interface gas. Two groups reported tuning of the Rashba spin orbit coupling (RSOC) inferred from magnetoresistance [28, 36] and measurements of the in-plane critical fields [11]. They found opposite dependencies for tuning the strength of the spin orbit coupling with V_g, making the impact of V_g on the spin orbit coupling unclear, possibly suggesting a peak in the spin orbit coupling.

Moreover, the discovery of magnetic patches coexistent with superconductivity

[15, 66, 32] and the presence of RSOC originating from the noncentrosymmetric nature of the interface have raised the possibility of an unconventional superconducting pairing mechanism or order parameter [75, 70]. However, all previous measurements studying how gating effects the properties of the interface used electronic transport, which gives limited information about the superconducting state. In this Letter, we use local magnetic susceptibility to make the first direct measurements of the superfluid density in LAO/STO and address the question of how the superconducting state evolves with V_g.

Measurements were made on a sample with five unit cells of LAO grown at 800° C and 1.3×10^{-5} mbar oxygen partial pressure on a TiO_2 terminated STO substrate. The growth was followed by a high pressure oxygen anneal, 600° C in 0.4 bar. The sample was silver epoxied to a piece of copper tape, which served as a back-gate. V_g was applied between the copper tape and the interface, which was contacted by aluminum wirebonds. Magnetization and susceptibility measurements were made using a scanning SQUID (Superconducting Quantum Interference Device) [17], with a 3 μm diameter pick-up loop and a concentric field coil for applying a local AC magnetic field. The pick-up loop is sensitive to both the DC static flux and the AC flux resulting from diamagnetic screening currents cancelling the field from the field coil. This setup enables simultaneous measurements of ferromagnetism and superconductivity in the sample [15].

A superconductor will generate screening currents to screen an applied field. The currents extend into a bulk superconductor by the penetration depth, λ. The temperature dependence of λ is a probe of the superconducting state. For a thin superconductor of thickness d, the screening distance is given by the Pearl length $\Lambda = 2\lambda^2/d$ [80]. Using a model by Kogan [56], we extract Λ from measurements of the screening currents as a function of the distance between the sensor and the sample. Λ is related to the superfluid density, $n_s = m^*/\mu_0 e^2 \Lambda$, where e is the elementary charge, μ_0 the permeability of free space, and $m^* = 1.46\, m_e$ the effective electron mass measured by [29] from Shubnikov de Haas on LAO/STO interfaces. We repeat these measurements at multiple temperatures and gate voltages to map out the superconducting state,

Fig. 6.1. We define T_c as the temperature at which the diamagnetic screening drops below our noise level of $0.01\,\Phi_0/\mathrm{A}$, corresponding to a minimum detectable n_s of $2-7\times10^{10}\,\mathrm{cm}^{-2}$. The statistical errors were smaller than systematic errors,outlined in gray in Fig. 6.2a, from imprecise knowledge of our measurement geometry. (See SOM) The systematic errors are fixed for a single cooldown and represent an overall scaling of n_s which would be the same for every measurement.

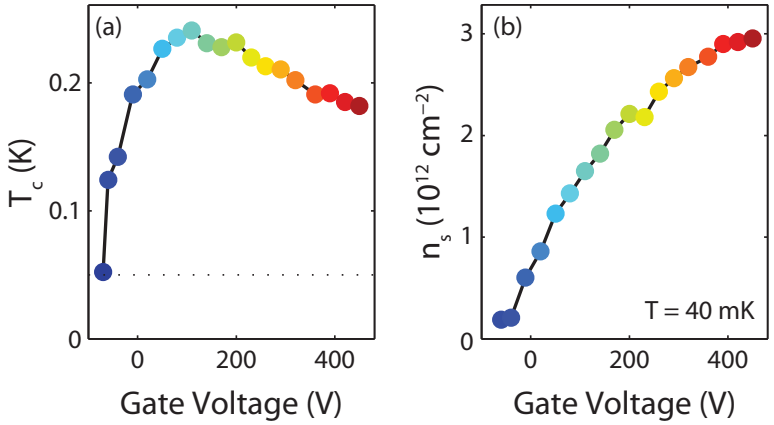

Figure 6.1: a) The critical temperature as a function of gate voltage forms a dome. The dashed line represents our lowest measurement temperature. b) The superfluid density at our lowest temperature as a function of gate voltage. The superfluid density increases monotonically throughout the dome. The color scale represents gate voltage and is repeated in Fig. 2.

T_c vs V_g (Fig. 6.1a) has a maximum $T_c = 240\,\mathrm{mK}$. In the range of applied V_g superconductivity can only be eliminated on the underdoped side of the dome, and n_s grows monotonically with V_g, with $n_s = 1.5\times10^{12}\,\mathrm{cm}^{-2}$ at the largest V_g. (Fig. 6.1b) The carrier density and mobility were measured in a separate cooldown with no back-gate. At 2 K the mobility was $1.02\times10^3\,\mathrm{cm}^2/\mathrm{Vs}$ and the density was $2.05\times10^{13}\,\mathrm{cm}^{-2}$, ten times larger than the largest n_s we observed.

A small ratio of the superfluid density to the normal density is expected in the dirty limit, in which the elastic scattering time, τ, much shorter than the superconducting gap, Δ_0 ($\hbar/\tau \gg \Delta_0$). $\hbar$ is reduced Plank's constant. Above T_c the normal density of electrons n is given by the optical sum rule $n \propto \int_0^\infty \sigma_1(\omega)d\omega$, where σ_1

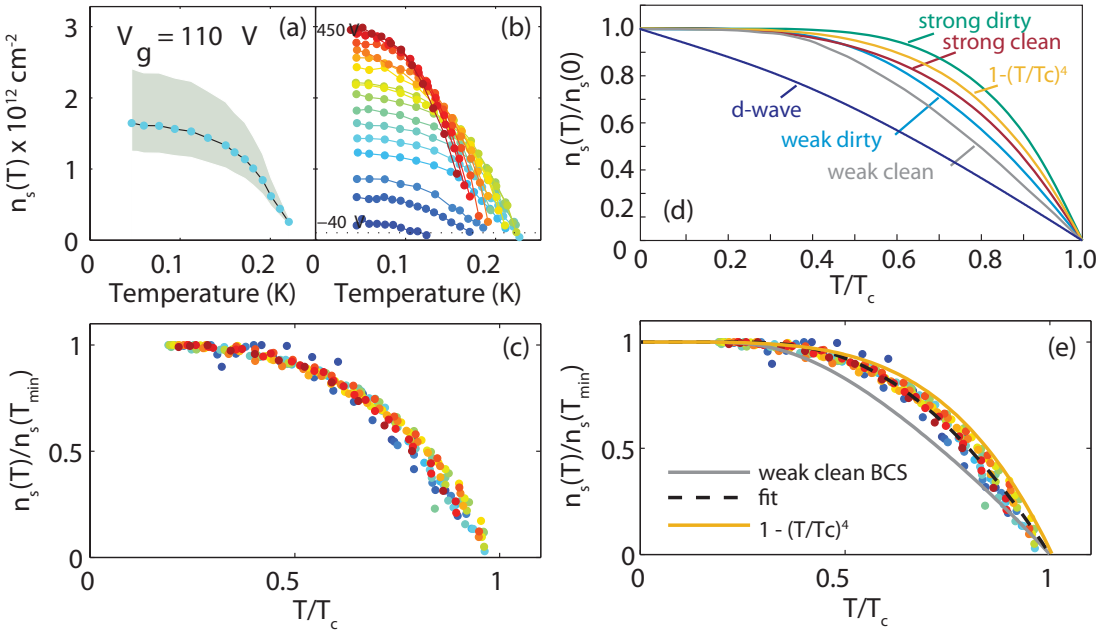

Figure 6.2: a) Superfluid density vs. temperature for $V_g = 110V$, the peak of the superconducting dome. The gray area shows systematic error. b) Superfluid density vs. temperature for every gate voltage. The colors represent the same V_g from Fig. 1. c) Normalized curves from b). d) Theoretical dependece of the superfluid density for a set of BCS models with different interactions, and d-wave superfluid density. Panel adapted from [27]. e) Normalized curves from b) compared to models. The gray line shows the temperature dependence of a weakly interacting clean BCS s-wave superconductor ($\Delta = 1.76$ and $a = 1$). The black dashed line is a fit to the data ($\Delta = 2.2$ and $a = 1.4$).

is the real part of the conductivity and ω the frequency. For a metal σ is sharply peaked near zero frequency, so scattering moves spectral weight to higher frequencies. Below T_c, a gap opens at $\omega = 2\Delta_0/\hbar$ and the spectral weight within that gap collapses to a delta function at the origin whose amplitude is proportional to n_s [43]. Therefore in the dirty limit, only a fraction of carriers enter the superconducting state, $n_s/n = 2\Delta_0/(\hbar/\tau)$. Using the gate tuned mobilities reported by Bell *et al.*, $100 - 1000\,\mathrm{cm}^2/\mathrm{Vs}$ [9], we expect the ratio n_s/n to be $0.01 - 0.1$, consistent with our measured n_s.

We now look at the temperature dependence of the superfluid density. Fig. 6.2b plots n_s vs. T for all V_g across the dome. Strikingly, when normalizing the curves they collapse (See Fig. 6.2c), showing that within our experimental errors there is no change in the superconducting gap structure with electrostatic doping. Furthermore, the collapse is reproducible over multiple positions, sweeps of V_g, and samples.[1]

The temperature dependence of the superfluid density is a direct probe of the superconducting order parameter. It can be used to distinguish BCS superconductors from unconventional superconductivity. We fit the normalized curves to a phenomenological BCS model with two parameters Δ and a [86]. Δ scales the superconducting gap $\Delta_0 = \Delta k_B T_c$. a is a shape parameter that determines how rapidly the gap opens below T_c, $n_s \propto 1 - (T/Tc)^{2a}$ [SOM]. $\Delta = 1.76$ and $a = 1$ for an clean s-wave BCS superconductor with weak coupling [86], plotted as the gray line in Fig. 6.2c. The fit to our data gives $\Delta = 2.2$ and $a = 1.4$. This is consistent with a BCS description with increased coupling or disorder. Both will increase the gap and the a parameter [27].

The flattening at low temperature indicates fully gapped behavior with a gap that is larger than BCS weak-coupling s-wave. Our lowest measurement temperature is 1/6 of $T_c^{\max}$, and n_s remains flat (within 3%) up to 35% of T_c. A full gap indicates the absence of low energy quasiparticle excitations, ruling out order parameters with nodes in the Fermi surface. Furthermore, the steep rise of n_s near T_c and the absence of a kink in the functional form rule out most weak coupling two band models [87], because a second smaller gap will slow the onset of superconductivity near T_c. Two gaps of similar size, both larger than the BSC gap or a dominant single large gap with second smaller amplitude gap, could reproduce the data.

The low n_s in the underdoped region may result in suppression of T_c by thermal phase fluctuations. Such fluctuations would result in a linear temperature dependence of n_s in the underdoped region. Following reference [35], we calculate a phase ordering temperature, $T_\theta^{max} = A\hbar^2 n_s(0)/4m^*$, where $A = 0.9$ in two dimensional systems. Fig. 6.3 shows T_c vs $n_s(40\,\mathrm{mK})$, additionally T_θ^{max} is plotted as a linear function of n_s:

[1] Similar behavior was seen in a separate 10 uc sample.

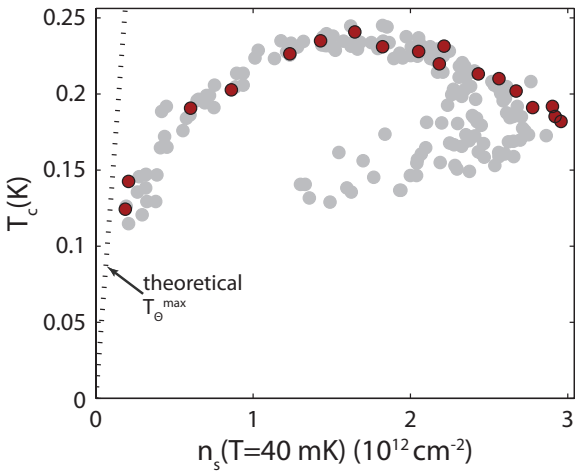

Figure 6.3: Critical temperature vs. the superfluid density at lowest temperature ($T \sim 40\,\mathrm{mK}$). The red points are the data from Figure 1 and the gray dots represent additional data sets. The dotted line is the theoretical phase fluctuation temperature from ref [35], which may be limiting the critical temperature on the underdoped side of the dome. The bimodal distribtion on the overdoped side is due to inhomogenaity that locallys suppresses n_s in different regions of the sample while the T_c remains the same. See also Fig. 6.4.

the line does not suggest a fit to our data. We have insufficient data at the lowest superfluid densities to make any statement about the functional form of $T_c(n_s)$ in the region where phase fluctuations may be limiting T_c. Nevertheless, the proximity of the phase ordering line to the underdoped data suggests that phase fluctuations may drive the abrupt decrease of T_c.

Given the 2D nature of the superconducting system we expect a BKT transition, where unbinding of vortex anti-vortex pairs suppresses superconductivity and results in a discontinuous jump in n_s near T_c. The jump should occur at finite superfluid density $n_s = 2m^*T_c/\pi\hbar^2$ [84]. For the maximum $T_c = 240\,\mathrm{mK}$ a BKT transition should occur at $5 \times 10^{10}\,\mathrm{cm}^{-2}$, which is too close to our measurement threshold to establish a BKT jump in our n_s vs. T curves.

Are our observations consistent with a simple $s-$wave order parameter from doped STO [58] or a two gap mixed state induced by symmetry breaking at the interface? Rashba spin orbit coupling (RSOC), induced by the structural inversion asymmetry, is expected to lift the spin degeneracy and split the energy bands [110]. Additionally, RSOC breaks parity and consequently mixes singlet and triplet states resulting in an $s-$wave component Δ_s mixed with a triplet induced d-vector $\mathbf{d}(\mathbf{k}) = \hat{x}k_y - \hat{y}k_x$ [37, 68]. Mixing results in two gaps, $\Delta = \Delta_s \pm |d_k|$, whose magnitudes depend on the weights of the singlet and triplet components. Varying the relative weights changes the density of states, but always results in two fully gapped Fermi surfaces except for the special case where the s-wave singlet and triplet gaps are the same and accidental line nodes form on one band [68]. Other reports [28, 11] have demonstrated significant tuning of the strength of RSOC with V_g. An open question, of particular importance to testing this two gap picture, is how do the weight of the two components change with V_g. Our results, showing a consistent functional form for n_s vs. T across all V_g, suggest that the superconducting gap structure does not change with V_g. The effect of RSOC on the band structure may depend on the chemical potential which is also tuned by the gate. Therefore the insensitivity of superconductivity to V_g cannot completely rule out a RSOC induced two gap scenario. Yet, our second observation of the fast opening of the gap near T_c and the compatibility of the data with a single

gap BCS model limits two gap models. Both gaps must be larger than the BCS s-wave gap to capture both the fast rise and flat low temperature dependence of the data. (See SOM)

Finally, disorder may play a role in washing out the triplet component. As stated above, the LAO/STO system is a dirty superconductor, with $\hbar/\tau >> \Delta$. Disorder averaging has very little impact on the isotropic s-wave component but may eliminate the triplet component.

In short, our data is most consistent with a single gap. We cannot rule out the presence of two gaps, but our observations limit their size and V_g dependence.

Our scanning SQUID system allows two dimensional mapping of superconductivity and magnetism at different V_g. Fig. 6.4 shows simultaneously imaged susceptometry and magnetometry scans of the same region at 80 mK for four different V_g. The inhomogeneity in the diamagnetic screening is very large in the underdoped region ($V_g = -10\,\mathrm{V}$) and re-enters the image in the overdoped region ($V_g = 390\,\mathrm{V}$). The least inhomogeneity is observed at optimal doping, although it does not disappear. In contrast the ferromagnetic patches are insensitive to V_g with a constant magnitude and orientation for all V_g. This behaviour was also observed on $15, 10$ and 3.3 uc samples, showing the electron density that is modified by V_g does not appear to influence the ferromagnetism.

In conclusion, we presented the first measurements of the superfluid density as a function of temperature at multiple gate voltages throughout the superconducting dome in LAO/STO heterostructures. The temperature dependence of n_s is well described by a fully gapped BCS model. Moreover, the normalized n_s vs. T curves collapse to a single functional form indicating there is no change in the gap structure with V_g. Although we cannot rule out a two gap mixed singlet/triplet model, the insensitivity of the superconducting state to V_g and the large slope near T_c limit two gap scenarios. Specifically, both gaps must be larger than the BCS s-wave gap and their relative size cannot change throughout the dome. A future experiment to distinguish between these two scenarios may be to gate the superconductivity in the presence of an in-plane field, which can change the relative magnitude of triplet

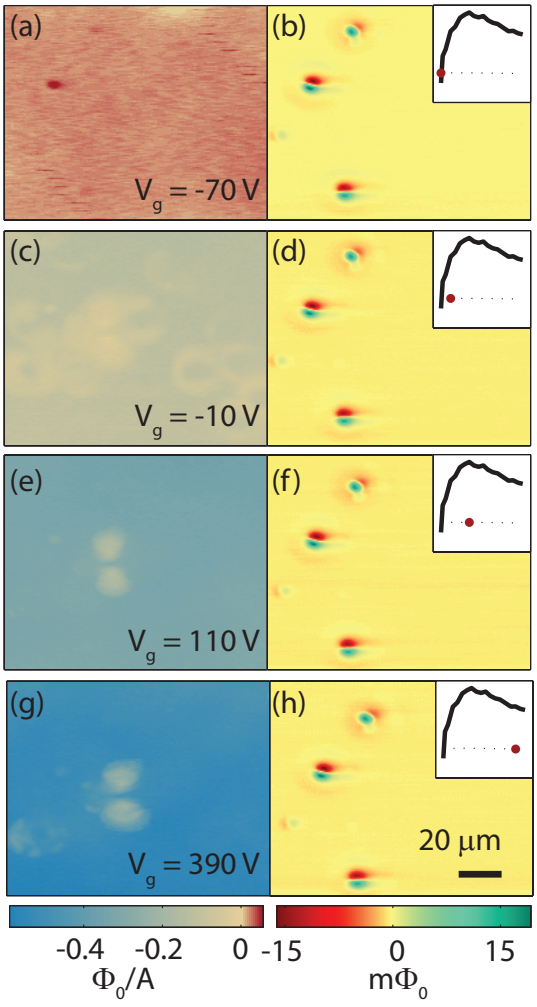

Figure 6.4: Susceptometry (left) and magnetometry (right) at 80 mK at different gate voltages. (Inset) Reproduction of the T_c dome from FIG 1 showing the relative location of V_g in each panel. a-b) The sample is no longer superconducting and has a paramagnetic response. Individual ferromagnetic dipoles are also visible in the paramagnetic image. c-d) Superconductivity appears and the landscape is relatively inhomogeneous. e-f) Peak of the superconducting dome, most inhomogeneity disappears. g-h) Excess inhomogeneity returns on the overdoped side of the dome. The ferromagnetic patches do not change with V_g and remain when superconductivity is gone.

and singlet gaps. Alternatively, samples in the clean limit may reveal a clearer two gap structure. Additionally, we found that the magnitude and orientation of the ferromagnetic patches that coexist with superconductivity are unchanged by V_g, while at the same time n_s goes from zero to $1.5 \times 10^{12}\,\mathrm{cm}^{-2}$. This shows the population of electrons that is modified by the gate is separate from the electrons that contribute to the ferromagnetic order.

6.3 Supplementary materials

6.3.1 Discussion of systematic errors

The accuracy of our superfluid density measurement is dominated by systematic errors which arise from insufficient knowledge of the physical parameters of our SQUID sensor and piezoelectric scanner. Our measurement of the superfluid density, n_s, relies on extracting the Pearl length, Λ, from fits to approach curves.

$$n_s = \frac{m^*}{\mu_0 e^2 \Lambda} \tag{6.1}$$

An approach curve measures the diamagnetic susceptibility as a function of the sensor height above the sample. Our SQUID sensor consists of a pair of concentric current carrying wires called the field coil and pick-up loop.

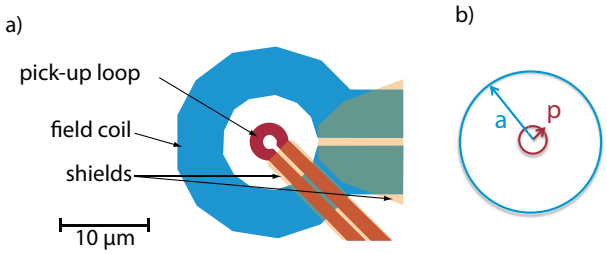

Figure 6.5: a) Actual layout of the SQUID field coil, pick-up loop and shields. b) Approximations to the actual layout used by Kogan [56].

We follow a model developed by Kogan which treats the SQUID's field coil as a

circular current loop of radius, a [56]. When the loop is brought near a superconducting thin film, the Meissner response of the film detected by the pick-up loop can be expressed as

$$\Phi(h) = \mu_0 \pi a p \int_0^\infty dk \frac{1}{1+\Lambda k} e^{-2kh} J_1(ka) J_1(kp), \tag{6.2}$$

where p is the pick-up loop radius, and μ_0 is the magnetic constant. This integral gives a value for the diamagnetic susceptibility, Φ, at a height h above the sample. Six physical parameters enter equation (6.2): the radius of the pick-up loop p, the radius of the field coil a, the piezo calibration from volts to microns V_c, the distance between the pick-up loop and the sample when the SQUID makes contact h_0, the offset of the susceptibility far from the sample Φ_{off}, and a background slope m. We convert the voltage applied to the z- bender, V_z, to a height $h = V_c V_z + h_0$. The susceptibility seen by the SQUID is

$$\Phi_{SQ} = \Phi + \Phi_{off} + mh. \tag{6.3}$$

Consequently, our fits for Λ depend on the accuracy of our knowledge of the other parameters.

We start with estimates of p and a. We can make accurate measurements of the two radii using an optical microscope; however these wire loops have a finite width and leads that deform their magnetic response with respect to the perfectly circular loops in Kogan's model. Using numerical methods, we calculate the source field using the measured dimensions of our non-ideal coils. We find the non-ideal nature of the field coil and pick-up loop results in a 15% error on the fitted value of Λ. This error works out to few hundred microns on our shortest Λ fits.

We now address the errors associated with our bender constant V_c and height offset h_0. We don't have accurate calibrations for these parameters, but we do know that these values should be the same for every touchdown curve. We fit hundreds of approach curves using Λ, V_c, and h_0 as free parameters, and assembled histograms of the fitted V_c and h_0 values. From the histograms we were able to extract a best value

and variance, σ. We then use the error propagation equation to relate the variances in V_c and h_0 to an error in Λ.

$$\sigma_\Lambda^2 \simeq \sigma_{V_c}^2 \left(\frac{\partial \Lambda}{\partial V_c}\right)^2 + \sigma_{h_0}^2 \left(\frac{\partial \Lambda}{\partial h_0}\right)^2 + ... + 2\sigma_{V_c h_0}^2 \left(\frac{\partial \Lambda}{\partial V_c}\right)\left(\frac{\partial \Lambda}{\partial h_0}\right) + ... \tag{6.4}$$

The propagation equation yielded an error of about 1 mm on our shortest Λ fits. This is a systematic error and is the same for every touchdown curve in the cooldown. It may change the overall calibration for n_s, but it will not change the trends in n_s vs V_g or n_s vs T.

We added the systematic errors from the sensor coils, bender calibration and height offset. The total systematic error is show as the gray outline shown in Fig. 6.6a. The error from the bender and offset dominates the error from the non-ideal nature of the pick-up loop and field coil.

6.3.2 Discussion of phenomenological BCS fits

We compare our normalized plots of superfluid density vs. temperature to a phenomenological BCS model with an isotropic s-wave superconducting gap. The normalized superfluid density, $n_s/n_s(T=0)$, was given by Prozorov and Giannetta [86]

$$\frac{n_s}{n_s(T=0)} = 1 - \frac{1}{2T}\int_0^\infty \cosh^{-2}\left(\frac{\sqrt{\epsilon^2 + \Delta^2(T)}}{2T}\right) d\epsilon, \tag{6.5}$$

where T is the temperature and $\Delta(T)$ is the superconducting gap function. The gap can be written [39] as

$$\Delta_0(T) = \Delta_0(0)\tanh\left(\frac{\pi T_c}{\Delta_0(0)}\sqrt{a\left(\frac{T_c}{T} - 1\right)}\right). \tag{6.6}$$

$\Delta_0(0)$ is the zero temperature energy gap and a is a shape parameter which determines how fast the gap opens. Near the critical temperature the superfluid density can be approximated as $n_s = 1 - (T/T_c)^{2a}$. For an isotropic s-wave gap $\Delta_0(0) = 1.76 k_B T_c$

and $a = 1$. We use equations (6.5) and (6.6) to fit our data and find $\Delta_0(0) = 2.2k_BT_c$ and $a = 1.4$. This is the dashed line plotted with the data in Fig. 6.2c of the main text.

6.3.3 Discussion of two gaps in BCS

We can use equations (6.5) and (6.6) to generate a phenomenological two-gap expression [71].

$$n_s(T) = pn_{s1}(T) + (1-p)n_{s2}(T) \tag{6.7}$$

Fig. 6.6 shows plots of the superfluid density for two gaps of equal weight ($p = .5$) with different physical parameters. The only combination that can support a

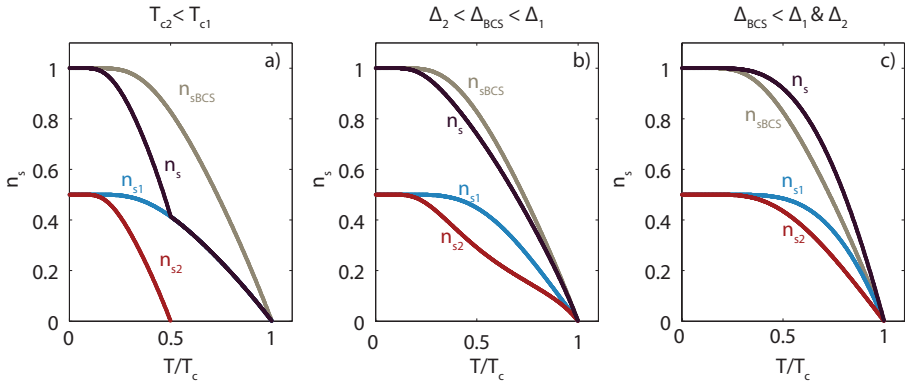

Figure 6.6: Comparison of a two-gap superfluid desnity n_s with a single gap BCS superfluid density $n_{s\mathrm{BCS}}$. In all three plots $n_{s1} = pn_{s1}$ and $n_s2 = pn_{s2}$ with a) Plots of two gaps with $\Delta_1 = \Delta_2 = 1.76$ and $a_1 = a_2 = 1$ but two different critical temperatures. b) Plots of two gaps with $\Delta_1 = 2.2$, $\Delta_2 = 1.1$, and $a_1 = a_2 = 1$. c) Plots of two gaps with with $\Delta_1 = 3$, $\Delta_2 = 2$, $a_1 = 1.8$ and $a_2 = 1$. Only in c) where both gaps are larger than $\Delta_{\mathrm{BCS}} = 1.76$ can we generate a total superfluid density that opens faster than BCS.

superfluid density function that rises faster than BCS near Tc has two gaps that are larger than the BCS gap.

Chapter 7

δ-doped STO

"Temperature dependence of the superfluid density of the two dimensional complex oxide superconductor δ-doped Strontium Titanate"

Complex oxides heterostructures have generated significant excitement as a toolbox for creating and controlling new two dimensional states. Often these structures exhibit properties that are not possible in bulk materials. One specific system, delta-doped strontinum titanate (δ-doped STO), confines Nb dopants in a thin layer of a strontinum titanate (STO) heterostrucure [62]. Undoped STO is an insulator with a large band gap. The Nb dopants contribute electrons to the STO conduction band, creating a two dimensional conduction layer which is a superconductor below 300 mK. The dopant layer thickness can be smaller than the electron mean free path. Such a setup allows the electron wave function to spread into undoped regions consequently enhancing the electron mobility [62]. The result is a two-dimensional superconducting layer with low carrier density [47] and high mobility that is electrostatically tunable [105].

Superconductivity in bulk (3D) doped STO is well established [95, 83, 58]. Careful analysis has been done to determine the dependence of the critical temperature (T_c) on the normal state carrier concentration. Koonce *et al*. found a dome structure with a maximum T_c of 300 mK at a concentration of $9 \times 10^{19}\,\mathrm{cm}^{-3}$ [58]. Early tunneling experiments showed evidence for two gap behavior at higher electron densities [16].

Recent advances in deposition techniques have allowed for the confinement of dopants into essentially 2D STO structures [113]. Superconductivity in these 2D structure is particularly interesting for many reasons. STO's perovskite crystal structure makes it a lattice matched substrate for growing other complex oxides. Layered complex oxides provide an opportunity for generating new physical phenomena. For example, an electric field can be used with a heterostructure of δ-doped STO and ferro-electric $Pb(Zr,Ti)O_3$ (PZT) to switch the superconducting state in the δ-doped STO layer at a fixed temperature [101]. Additionally, the bandstructure of δ-doped STO is similar to the bandstructure of the superconducting heterointerface between $LaAlO_3$ and STO [89]. Better understanding of superconductivity in δ-doped STO may provide insights into the origins of superconductivity at the LAO/STO interface.

The normal state properties of the electrons confined in δ-doped STO have been studied by transport. Quantum oscillations have been observed demonstrating high mobilities in the 2D system [62, 53]. Moreover, measurements on a series of samples with different thicknesses revealed an evolution of the beating pattern of the oscillations [53]. This evolution is consistent with the degeneracy of the 3D conduction band being lifted by confinement in the thinner samples, explicitly revealing the 2D nature of these structures.

This paper presents two different measurements of the magnetic penetration depth in δ-doped STO. We are interested in measuring the penetration depth because examining its temperature dependence gives insight into the symmetry of the superconducting order parameter [86]. In section 7.1 we present measurements of the Pearl length extracted from the diamagnetic susceptibility response of the δ-doped STO. We include a detailed description of the systematic errors that impact our measurement. Section 7.2 details extracting the penetration depth from the profile of Pearl vortices. We find that the superconductivity in δ-doped STO is well describes by a BCS model with a single full gap.

7.1 Measurement: Diamagnetic susceptibility

The superconducting penetration depth, λ, is the distance a magnetic field penetrates into a superconductor before it is fully screened by internal currents. This screening effect is known as the Meissner response. In a thin superconductor with a thickness, d, that is much smaller than λ the screening currents are distributed over a smaller cross-sectional area. Consequently the effective penetration depth, also called the Pearl length, Λ, is rescaled by d [80].

$$\Lambda = \frac{2\lambda^2}{d} \tag{7.1}$$

We use a scanning Superconducting QUantum Interference Device (SQUID) with an integrated field-coil source to map the Meissner response of a superconducting sample. The SQUID's 3 μm pick-up loop is sensitive to magnetic flux, and it's small size enables measurements on a local length scale. In addition the SQUID has a field coil, concentric with the pick-up loop. Driving an AC current in the field coil results in an AC local field. Using a lock-in technique, the pick-up loop is sensitive to the sample's response to the field applied by the field coil.

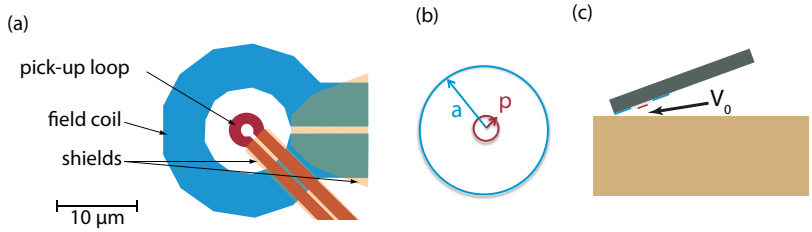

Figure 7.1: (a) Actual layout of the SQUID tip with field coil, pick-up loop and shields. (b) Approximation to the actual layout used by Kogan [56] and Kirtley [54]. (c) Cartoon showing the alignment angle between the sensor and sample. The pick-up loop (shown in red) has a finite offset from the sample even when the sensor is in contact. Adapted from [54].

We extract a value for Λ from the height dependence of the Meissner response to the field generated by the field coil. In thin weakly superconducting samples, like

δ-doped STO, Λ is much longer than the pick-up loop diameter. The SQUID acts a local probe, able to detect variations in the local value of Λ. In this limit, Kogan approximated our SQUID's coils as infinitely thin current loops (Fig. 7.1b), and derived an expression for the diamagnetic susceptibility as a function of Λ and the sensor height [56]. We use this expression to fit touchdown curves, Fig. 7.2. In a touchdown curve, we drive the SQUID toward the sample and measure diamagnetic susceptibility as a function of sensor height.

$$\Phi(h) = \mu_0 \pi a p \int_0^\infty dk \frac{1}{1+\Lambda k} e^{-2kh} J_1(ka) J_1(kp), \tag{7.2}$$

As indicated in Fig. 7.1b, a is the field coil radius, p is the pick-up loop radius, μ_0 is the magnetic constant, and J_1 are Bessel functions of the first kind. Extending Kogan's work, Kirtley found that in the limit of very long Λ equation (7.2) reduces to a simple analytical expression [54] with Λ directly proportional to the measured susceptibility.

$$\Phi(z) = M \frac{a}{\Lambda} \left(1 - \frac{2z}{\sqrt{1+4z^2}} \right) \tag{7.3}$$

$$z = \frac{h}{a} = \frac{V_c}{a}(V - V_0) \tag{7.4}$$

M is the mutual inductance between the SQUID's field coil and pick-up loop. z is the sensor height, h, normalized by the field coil radius. The sensor height changes in proportion to the voltage applied to the cantilever piezo that the SQUID sits on. V_c is the calibration constant in μm/V. Due to our finite alignment angle, when the sensor makes contact with the sample the pick-up loop is still a finite distance away, (see Fig. 7.1c). V_0 is the distance, in volts, between the pick-up loop and sample when the sensor is in contact. The full fitting expression includes additional terms for a vertical (susceptibility) offset and linear background. We fix the linear background by taking an approach curve above T_c and find the slope when there is no diamagnetic response from the sample.

Besides being a simpler expression, an additional benefit of using Kirtley's expression (7.4) is that we have two less fitting parameter. We replace p, which is difficult to accurately measure or model, with M. M is directly measurable. We find $M = 0.8\,\Phi_0/\mathrm{A}$ for our SQUIDs. Additionally, in Kirtley's expression all the length parameters are scaled by a, so a is no longer a fitting parameter. We only reintroduce a as a scaling parameter at the very end to generate physical values. The remaining fit parameters are Λ/a, V_c/a, V_0, and an offset in susceptibility.

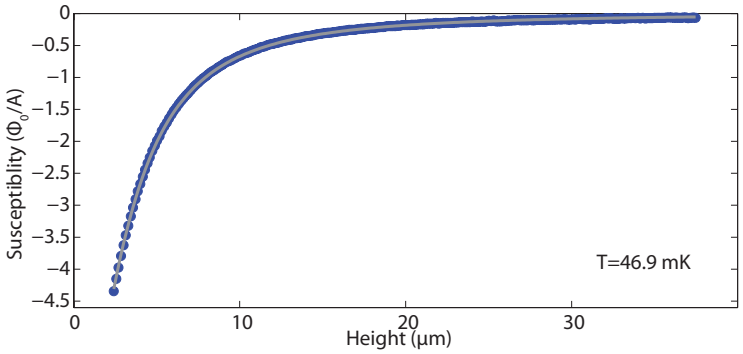

Figure 7.2: A single touchdown curve plotting the susceptibility vs. sensor height. The gray line is a fit to equation (7.4).

Fig. 7.2 shows a touchdown curve and the corresponding fit to equation (7.4). The optimal values for the four free parameters are $\Lambda/a = 97.15$, $V_c/a = 0.0175\,V^{-1}$, $V_0 = -0.7274\,\mathrm{V}$, and $\Phi_0 = -7.1 \times 10^{-2}\,\Phi_0/\mathrm{A}$. We fixed $M = 0.8\,\Phi_0/\mathrm{A}$ and slope=$3.507 \times 10^{-3}\,\Phi_0/\mathrm{A}$. Using the numerical calculations of Brandt and Clem [21], we model the distribution of supercurrents in a wire of finite width, employing optically measured field coil dimensions. We find an effective field coil radius, $a = 8.4\,\mu\mathrm{m}$. By multiplying Λ/a by a we get a physical value for Λ. The Pearl length extracted from the touchdown curve in Fig. 7.2 is $\Lambda = 816\,\mu\mathrm{m}$.

7.1.1 Systematic errors

Our fit parameters are not independent and therefore introduce systematic errors. To find the confidence level for our fits we vary two parameters systematically and

fit the other two parameters. We plot the chi-squared error, $\Xi^2 = \sum_n (\Phi(n) - \Phi_{\text{fit}}))^2$, normalized by the best error Ξ^2_{min} as contours in Fig. 7.3. The colorscale in Fig. 7.3 is cut off where the chi-squared error doubles. That contour is also the 65% confidence interval.

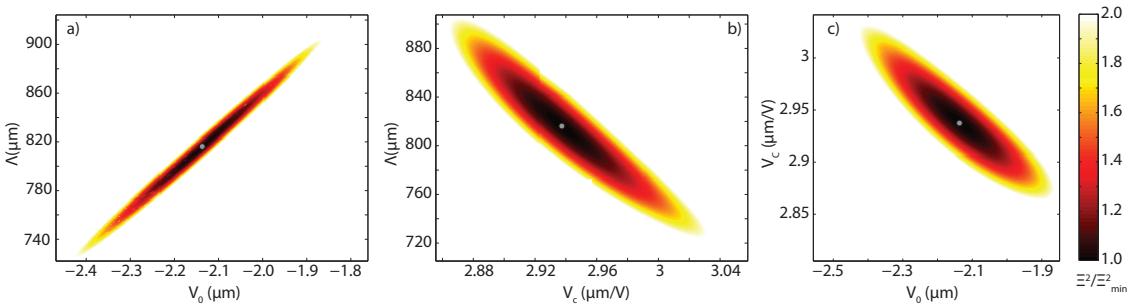

Figure 7.3: Plot of the error squared divided by the global minimum Ξ^2/Ξ^2_{min}. The colored area shows the contour where the error doubles. a) Fix Λ and V_0 with V_c and the vertical offset free. b) Fix V_c and Λ with V_0 and the vertical offset free. c) Fix V_0 and V_c with Λ and the vertical offset free.

We use the 65% confidence interval to define the systematic error given in Table 7.1.

Parameter	Best Fit	Lower Bound 65% CI	Upper Bound 65% CI
Λ	$816.06\,\mu$m	715	894
V_c	$2.94\,\mu$m/V	2.85	3.05
V_0	$-0.727\,$V	-0.87	-0.60

Table 7.1: Best fit and systematic error values for the fit shown in Fig. 7.2

Both V_c and V_0 depend on a physical parameters in the scanner. Neither of these values should change for different touchdown curves. Consequently we fit them only at the lowest temperatures when the superconducting response is largest. From the confidence ellipse in Fig. 7.3c we find the covariance between V_c and V_0. We use the error propagation equation, equation 7.5, to find the variance of Λ.

$$\sigma_\Lambda{}^2 \simeq \sigma_{V_c}{}^2 \left(\frac{d\Phi}{dV_c}\right)^2 + \sigma_{V_0}{}^2 \left(\frac{d\Phi}{dV_0}\right)^2 + 2\sigma_{V_cV_0}{}^2 \left(\frac{d\Phi}{dV_c}\right)\left(\frac{d\Phi}{dV_0}\right) \tag{7.5}$$

The σ^2 terms are the terms of the covariance matrix. We find $\sigma_\Lambda = 172\,\mu$m, which is almost the same as the variance reported in table 7.1.

7.1.2 Temperature dependence

We examine the temperature dependence of the Pearl length by taking a touchdown curve at multiple temperatures between our base temperature and T_c. A temperature sequence of touchdown curves is plotted in Fig. 7.4a. The gray lines are fits to equation (7.4). Only Λ/a and the vertical offset were allowed to vary in these fits. The normalized bender calibration $V_c = 0.0175\,\mathrm{V}^{-1}$, and voltage offset $-0.727\,$V, were fixed to the values found in the lowest temperature fit. The temperature dependence of Λ is plotted in Fig. 7.4b.

We can use our measurement of the Pearl lenght to extract the superfluid density. Λ is inversely proportional to the superfluid density, n_s.

$$n_s = \frac{2m^*}{\mu_0 e^2 \Lambda} \tag{7.6}$$

e is the elementary charge and μ_0 is the magnetic constant. Shubnikov-de Haas measurements have yielded an effective mass of $m^* = 1.26m_e$ in δ-doped STO [62]. We use this value to find n_s, which is plotted as a function of temperature in Fig. 7.4c.

We compare our superfluid density vs. temperature data to a phenomenological BCS model with parameters Δ and a [86].

$$n_s = n_s(T=0)\left(1 - \frac{1}{2T}\int_0^\infty \cosh^{-2}\left(\frac{\sqrt{\epsilon^2 + \Delta^2(T)}}{2T}\right) d\epsilon\right) \tag{7.7}$$

$$\Delta_0(T) = \Delta_0(0)\tanh\left(\frac{\pi T_c}{\Delta_0(0)}\sqrt{a\left(\frac{T_c}{T} - 1\right)}\right). \tag{7.8}$$

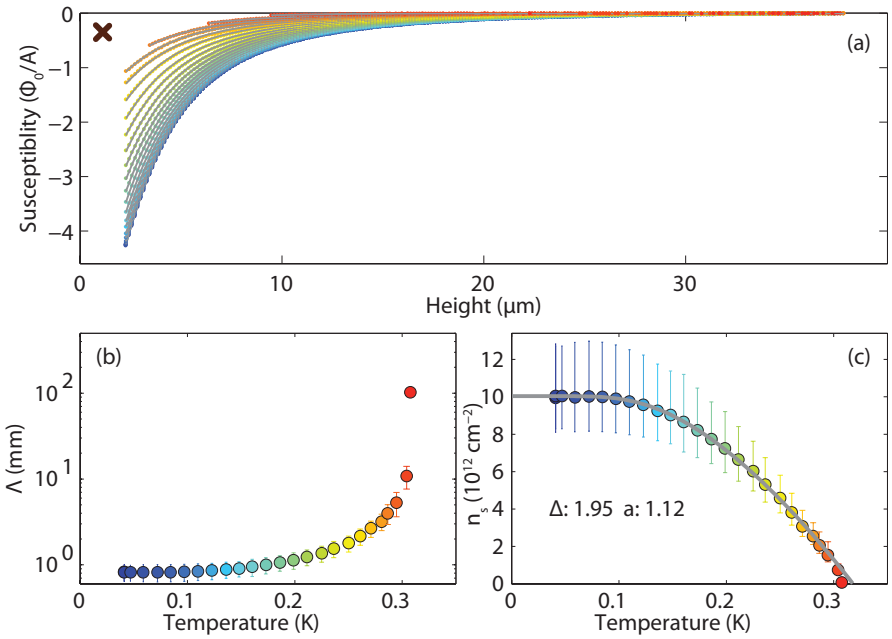

Figure 7.4: a) Set of touchdowns curves at different temperatures. Base temperature is 40 mK (shown in blue) and the temperature increases to the critical temperature of 310 mK (shown in red). The gray lines are fits to equation (7.4). b) Pearl length vs. temperature. Λ is extracted from each touchdown curve. The color points correspond to the same colored touchdown curve in a). c) Superfluid density vs. temperature. We use the Λ value with equation (7.6) to find the superfluid density. The colors of the points correspond to a colored touchdown curve in a). The gray line is a fit to a phenomenological BCS model with fitting parameters Δ and a shown on the plot.

This s-wave BCS model assumes a fully gapped and isotropic Fermi surface. Δ is related to the superconducting gap $\Delta_0 = \Delta k_B T_c$ and a is a shape parameter. In the s-wave clean weakly interacting limit $\Delta = 1.76$ and $a = 1$. Adding disorder or strong interactions to the system will increase both Δ and a [27]. Our fitted values of $\Delta = 1.95$ and $a = 1.12$ show good agreement with a single gapped BCS model.

7.1.3 Variation in the penetration depth

The scanning setup allows us to make a two-dimensional map of the superfluid density. Fig. 7.5 shows two scans of the same area of the sample at two different temperatures. The approach curves from Fig. 7.4 were taken at the point indicated by the brown x in Fig. 7.5.

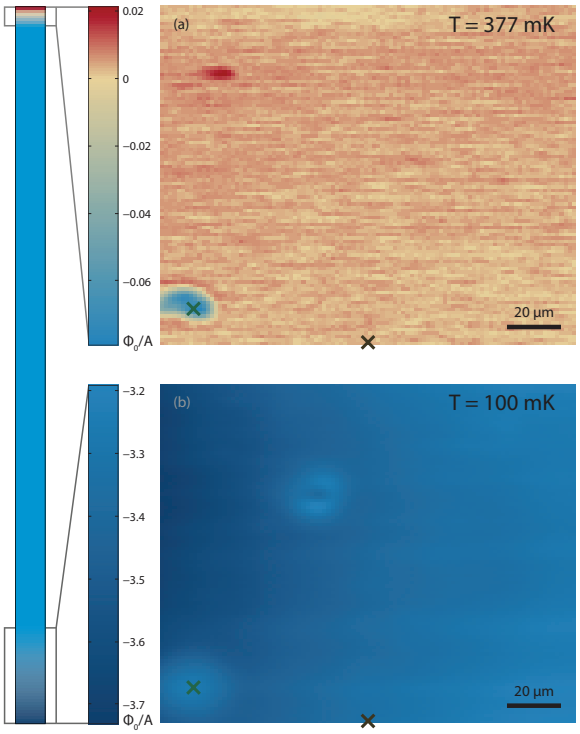

Figure 7.5: Area susceptometry scan at (a)100 mK and (b)377 mK. A defect in the lower left corner is visible in both images. In (a) this region has a lower susceptibility compared to the surroundings and in (b) this region remains superconducting when the surroundings are normal. The total span of the superconductivity is represented by the color bar on the far left. The brown x shows the location of the touchdown curves from Fig. 7.4. The green x shows the location of the touchdown curves from Fig. 7.6.

At low temperature two defects are visible in Fig. 7.5a. These defects have a suppressed diamagnetic response compared to their surroundings. Surprisingly, above the bulk T_c, Fig. 7.5b, the defect in the lower left corner is still superconducting.

We repeat our analysis of the penetration depth as a function of temperature on this defect in the position indicated by the green x.

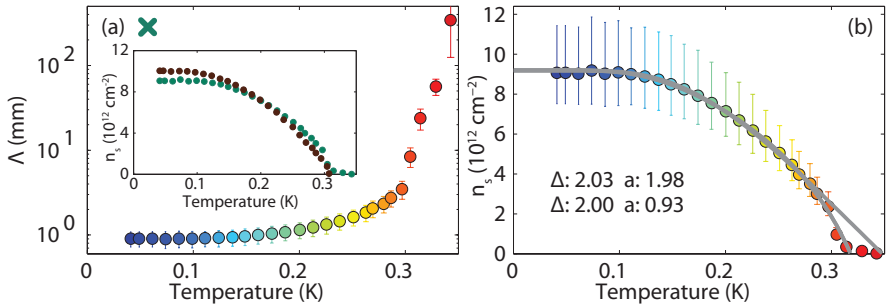

Figure 7.6: (a) Pearl Length vs. temperature. Λ is extracted from each touchdown curve. The color points correspond to the same colored touchdown curve in a). Inset superfluid density vs. temperature for the two positions indicated by the green and brown x in Fig. 7.5. (b) Superfluid density vs. temperature. We use the Λ value with equation (7.6) to find the superfluid density. The gray line is a fit to a phenomenological BCS model with fitting parameters Δ and a shown on the plot.

On the defect, the temperature dependence of both Λ and the superfluid density show strange behavior at high temperatures. The deviation from expected behavior onsets at $T = 318\,\mathrm{mK}$, which is also the bulk T_c. Below that temperature the majority of the diamagnetism likely comes from the surrounding region. Above that temperature only the small island contributes to the diamagnetic response.

We repeat the BCS fitting twice with two different T_c values. We find $\Delta = 2.03$ and $a = 1.98$ for $T_c = 318\,\mathrm{mK}$ and $\Delta = 2.00$ and $a = 0.93\,\mathrm{mK}$ for $T_c = 348\,\mathrm{mK}$. Clearly neither of these two models describe the data over all the temperatures. This is likely caused by the presence of a second order parameter with a different critical temperature in the island.

7.2 Penetration depth from vortices

Vortices in thin superconductors, called Pearl vortices, differ from Abrikosov vortices found in bulk type II superconductors. Specifically, the magnetic fields generated by

the vortex perpendicular to the superconductor diverge as $1/r$ at distances $r \ll \Lambda$, which is much faster than the $\ln(r/\lambda)$ divergence of the fields near Abrikosov vortices [57]. This makes the field profile of pearl vortices very sharp with most of the weight near $r = 0$. Consequently, their signal is visible even though Λ is many millimeters in length. Additionally, Pearl vortices interact over a much longer length scale than Abrikosov vortices. For Pearl vortices the long range interaction potential is $V_{\text{int}} \sim \Lambda/r$ for $r \gg \Lambda$, while close range integrations go as $\ln(\Lambda/r)$ for $r \ll \Lambda$ [80]. It is the logarithmic close range interaction which, at temperatures where Λ approaches the sample size, drives a BKT transition in two-dimensional superconductors.

We are interested in using the profile of a Pearl vortex, as an alternative method of for measuring the Pearl length in 2D superconductors [100]. The flux profile of a Pearl vortex imaged with our SQUID's pick-up loop is

$$\Phi(r, z) = p \int_0^\infty \frac{1}{1 + k\Lambda} J_0(kr) J_1(kp) e^{(-kz)} dk. \tag{7.9}$$

The flux, Φ is given in units of the superconducting flux quantum $\Phi_0 = h/2e$ as a function of the scan height, z, and the radial distance from the vortex center, r. p is the radius of the pick-up loop and J are Bessel functions of the zeroth and first kind.

Figure 7.7(a) shows a magnetometry scan with many pearl vortices. The scan was taken at a scan height of $z = 2\,\mu$m and a temperature of 80 mK. The vortices were not strongly pinned, which is not surprising considering the cleanliness of the δ-doped interface. The two vortices on the far right side of the image were dragged during the scan, leaving only a portion of their profile in the image.

Figure 7.7(b) shows line cuts in gray dots in the x and y-directions of the vortex indicated in Figure 7.7(a). By fixing $p = 2\,\mu$m and $z = 2\,\mu$m, Λ is the only free parameter in equation (7.9). We then us a look-up table to extract the Pearl length that corresponds to the peak of the cross-section. The result is $\Lambda = 918.5\,\mu$m for the vortex in Figure 7.7(b), and the corresponding cross section is shown as the solid line.

This approach provides a second method for measuring the temperature dependence of the Pearl length and consequently the superfluid density. We took magnetometry scans at a series of temperatures between our base scanning temperature of 80 mK and T_c. Using the profiles of each vortex in each image we found a series of Λ values as a function of temperature.

We find general agreement between the temperature dependence of the Pearl length extracted from vortices (Figure 7.8) and from susceptibility approach curves (Figure 7.4). There is a difference between the zero temperature limit of Λ for the two techniques. $\Lambda(T = 0) = 816\,\mu$m for the first touchdown position, $\Lambda(T = 0) = 909\,\mu$m for the second touchdown position, and $\Lambda(T = 0) = 963\,\mu$m for the vortex profile. This difference is likely due to the systematic uncertainties related to the pick-up loop image kernel and scan height. We have not done a careful analysis of the systematic errors associated with fitting the vortex profile. However, a comparison of the temperature dependence of the superfluid density extracted from vortex profiles provides a nice confirmation of our measurement of the superfluid from susceptibility touchdowns.

7.3 Conclusions

Using a local magnetic imaging technique we have measured the Pearl length in the two dimensional interface superconductor δ-doped STO. We measured this quantity in two different ways: fitting the shape of susceptibility approach curves, and fitting the profile of Pearl vortices. We find agreement between the two techniques. Additionally, our measurement of the Pearl length is related to the local superfluid density. The temperature dependence of the superfluid density show that δ-doped STO is most likely a BCS superconductor with a single gap.

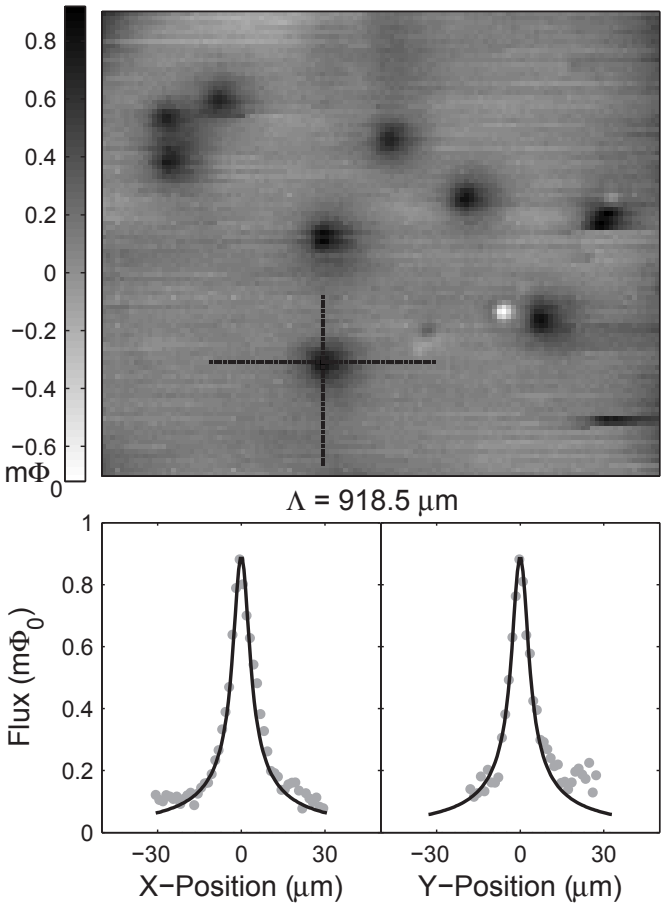

Figure 7.7: (a) Magnetometry scan of vortices at 80 mK. (b) Profile along x and y axes of the vortex indicated in (a). The Pearl length at this temperature is 918 μm. The data is shown as gray dots and the solid line is a fit to equation (7.9) with fixed parameters $z = 2\,\mu$m and $p = 2\,\mu$m. The Pearl length extracted from the fit is $\Lambda = 918.5\,\mu$m.

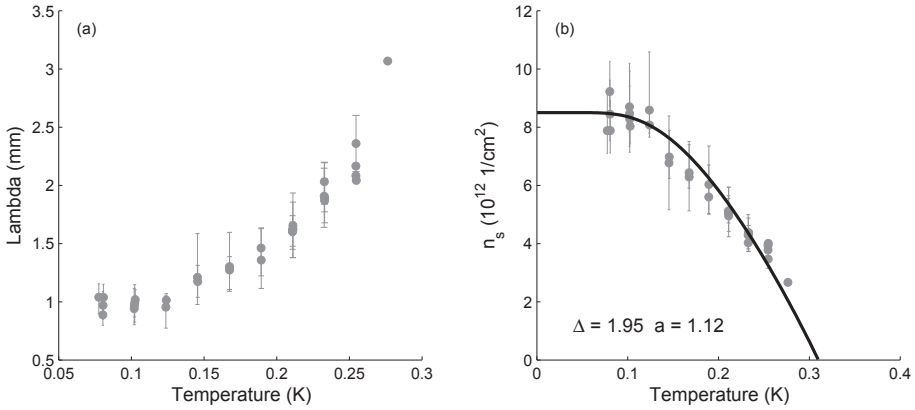

Figure 7.8: (a) Λ vs. temperature extracted from vortex profiles. The point is the average Λ value calculated from all vortices in the image. The error-bar indicate the extrema of Λ represented by vortices in a single image. (b) The corresponding superfluid density vs. temperature. The black curve is not a fit, but a reproduction of the BCS model from Figure 7.4.

Bibliography

[1] C. H. Ahn, A. Bhattacharya, M. Di Ventra, J. N. Eckstein, C. D. Frisbie, M. E. Gershenson, A. M. Goldman, I. H. Inoue, J. Mannhart, A. J. Millis, A. F. Morpurgo, D. Natelson and J. Triscone. *Reviews of Modern Physics*, **78**, 1185 (2006).

[2] V. Ambegaokar and U. Eckern. *Europhysics Letters*, **13**, 733 (1990).

[3] V. Ambegaokar and U. Eckern. *Physical Review B*, **44**, 10358 (1991).

[4] D. Aoki, A. Huxley, E. Ressouche, D. Braithwaite, J. Flouquet, J. Brison, E. Lhotel and C. Paulsen. *Nature*, **413**, 613 (2001).

[5] Ariando, X. Wang, G. Baskaran, Z. Q. Liu, J. Huijben, J. B. Yi, A. Annadi, A. R. Barman, A. Rusydi, S. Dhar, Y. P. Feng, J. Ding, H. Hilgenkamp and T. Venkatesan. *Nature Communications*, **2**, 188 (2011).

[6] K. Arutyunov, D. Golubev and A. Zaikin. *Physics Reports*, **464**, 1 (2008).

[7] B. J. Baelus, F. M. Peeters and V. A. Schweigert. *Physical Review B*, **61**, 9734 (2000).

[8] M. R. Beasley, J. E. Mooij and T. P. Orlando. *Physical Review Letters*, **42**, 1165 (1979).

[9] C. Bell, S. Harashima, Y. Kozuka, M. Kim, B. G. Kim, Y. Hikita and H. Y. Hwang. *Physical Review Letters*, **103**, 226802 (2009).

[10] S. Bell. *Journal of Physics B: Atomic, Molecular and Optical Physics*, **3**, 745 (1979).

[11] M. Ben Shalom, M. Sachs, D. Rakhmilevitch, A. Palevski and Y. Dagan. *Physical Review Letters*, **104**, 126802 (2010).

[12] K. H. Bennemann and J. B. Ketterson (eds.). *The Physics of Superconductors*, volume 2 (Springer, 2004).

[13] J. Berger. *Physical Review B*, **67**, 014531 (2003).

[14] J. Berger and J. Rubinstein. *Physical Review B*, **56**, 5124 (1997).

[15] J. A. Bert, B. Kalisky, C. Bell, M. Kim, Y. Hikita, H. Y. Hwang and K. A. Moler. *Nature Physics*, **7**, 767 (2011).

[16] G. Binnig, A. Baratoff, H. E. Hoenig and J. G. Bednorz. *Physical Review Letters*, **45**, 1352 (1980).

[17] P. G. Björnsson, B. W. Gardner, J. R. Kirtley and K. A. Moler. *Review of Scientific Instruments*, **72**, 4153 (2001).

[18] H. Bluhm, J. A. Bert, N. C. Koshnick, M. E. Huber and K. A. Moler. *Physical Review Letters*, **103**, 026805 (2009).

[19] H. Bluhm, N. C. Koshnick, M. E. Huber and K. A. Moler. *Physical Review Letters*, **97**, 237002 (2006).

[20] H. Bluhm, N. C. Koshnick, M. E. Huber and K. A. Moler. *arXiv.org:0709.1175* (2007).

[21] E. H. Brandt and J. R. Clem. *Physical Review B*, **69**, 184509 (2004).

[22] A. Brinkman, M. Huijben, M. v. Zalk, J. Huijben, U. Zeitler, J. C. Maan, W. G. v. d. Wiel, G. Rijnders, D. H. A. Blank and H. Hilgenkamp. *Nature Materials*, **6**, 493 (2007).

[23] V. Bruyndoncx, L. Van Look, M. Verschuere and V. V. Moshchalkov. *Physical Review B*, **60**, 10468 (1999).

[24] L. Bulaevskii, A. Buzdin, M. Kulić and S. Panjukov. *Advances in Physics*, **34**, 175 (1985).

[25] A. I. Buzdin. *Reviews of Modern Physics*, **77**, 935 (2005).

[26] N. Byers and C. N. Yang. *Physical Review Letters*, **7**, 46 (1961).

[27] J. P. Carbotte. *Reviews of Modern Physics*, **62**, 1027 (1990).

[28] A. D. Caviglia, M. Gabay, S. Gariglio, N. Reyren, C. Cancellieri and J. M. Triscone. *Physical Review Letters*, **104**, 126803 (2010).

[29] A. D. Caviglia, S. Gariglio, C. Cancellieri, B. Sacćpé, A. Fête, N. Reyren, M. Gabay, A. F. Morpurgo and J. M. Triscone. *Physical Review Letters*, **105**, 236802 (2010).

[30] A. D. Caviglia, S. Gariglio, N. Reyren, D. Jaccard, T. Schneider, M. Gabay, S. Thiel, G. Hammerl, J. Mannhart and J. M. Triscone. *Nature*, **456**, 624 (2008).

[31] C. Cen, S. Thiel, G. Hammerl, C. W. Schneider, K. E. Andersen, C. S. Hellberg, J. Mannhart and J. Levy. *Nature Materials*, **7**, 298 (2008).

[32] D. A. Dikin, M. Mehta, C. W. Bark, C. M. Folkman, C. B. Eom and V. Chandrasekhar. *Physical Review Letters*, **107**, 056802 (2011).

[33] Y. Dubi, Y. Meir and Y. Avishai. *Nature*, **449**, 876 (2007).

[34] V. Emery and S. Kivelson. *Nature*, **374**, 434 (1995).

[35] V. J. Emery and S. A. Kivelson. *Nature*, **374**, 434 (1995).

[36] A. Fête, S. Gariglio, A. D. Caviglia, J. M. Triscone and M. Gabay. *arXiv:1203.5239* (2012).

[37] P. A. Frigeri, D. F. Agterberg, A. Koga and M. Sigrist. *Physical Review Letters*, **92**, 097001 (2004).

[38] N. Giordano. *Physical Review Letters*, **61**, 2137 (1988).

[39] F. Gross, B. S. Chandrasekhar, D. Einzel, K. Andres, P. J. Hirschfeld, H. R. Ott, J. Beuers, Z. Fisk and J. L. Smith. *Zeitschrift fr Physik B Condensed Matter*, **64**, 175 (1986).

[40] J. J. Hauser. *Journal of Low Temperature Physics*, **7**, 335 (1972).

[41] A. D. Hernández, B. J. Baelus, D. Domínguez and F. M. Peeters. *Physical Review B*, **71**, 214524 (2005).

[42] C. W. Hicks, T. M. Lippman, M. E. Huber, J. G. Analytis, J. Chu, A. S. Erickson, I. R. Fisher and K. A. Moler. *Physical Review Letters*, **103**, 127003 (2009).

[43] C. C. Homes, S. V. Dordevic, D. A. Bonn, R. Liang and W. N. Hardy. *Physical Review B*, **69**, 024514 (2004).

[44] M. E. Huber, N. C. Koshnick, H. Bluhm, L. J. Archuleta, T. Azua, P. G. Björnsson, B. W. Gardner, S. T. Halloran, E. A. Lucero and K. A. Moler. *Review of Scientific Instruments*, **79**, 053704 (2008).

[45] M. E. Huber, P. A. Neil, R. G. Benson, D. A. Burns, A. F. Corey, C. S. Flynn, Y. Kitaygorodskaya, O. Massihzadeh, J. M. Martinis and G. C. Hilton. *Applied Superconductivity, IEEE Transactions on*, **11**, 4048 (2001).

[46] M. Huijben, A. Brinkman, G. Koster, G. Rijnders, H. Hilgenkamp and D. H. A. Blank. *Advanced Materials*, **21**, 1665 (2009).

[47] J. Hulm, M. Ashkin, D. Deis, C. Jones and C. Gorter. In *Progress in Low Temperature Physics* (Elsevier, 1970), volume Volume 6, 205–242.

[48] L. D. Jackel, W. W. Webb, J. E. Lukens and S. S. Pei. *Physical Review B*, **9**, 115 (1974).

[49] A. Joshua, S. Pecker, J. Ruhman, E. Altman and S. Ilani. *arXiv:1110.2184* (2011).

[50] B. Kalisky, J. A. Bert, B. B. Klopfer, C. Bell, H. K. Sato, M. Hosoda, Y. Hikita, H. Y. Hwang and K. A. Moler. *Nature Communications*, **3**, 922 (2012).

[51] B. Kalisky, J. R. Kirtley, J. G. Analytis, J. Chu, A. Vailionis, I. R. Fisher and K. A. Moler. *Physical Review B*, **81**, 184513 (2010).

[52] A. Kanda, B. J. Baelus, D. Y. Vodolazov, J. Berger, R. Furugen, Y. Ootuka and F. M. Peeters. *Physical Review B*, **76**, 094519 (2007).

[53] M. Kim, C. Bell, Y. Kozuka, M. Kurita, Y. Hikita and H. Y. Hwang. *Physical Review Letters*, **107**, 106801 (2011).

[54] J. R. Kirtley, B. Kalisky, J. A. Bert, C. Bell, M. Kim, Y. Hikita, H. Y. Hwang, J. H. Ngai, Y. Segal, F. J. Walker, C. H. Ahn and K. A. Moler. *Physical Review B*, **85**, 224518 (2012).

[55] J. R. Kirtley, C. C. Tsuei, V. G. Kogan, J. R. Clem, H. Raffy and Z. Z. Li. *Physical Review B*, **68**, 214505 (2003).

[56] V. G. Kogan. *Physical Review B*, **68**, 104511 (2003).

[57] V. G. Kogan, V. V. Dobrovitski, J. R. Clem, Y. Mawatari and R. G. Mints. *Physical Review B*, **63**, 144501 (2001).

[58] C. S. Koonce, M. L. Cohen, J. F. Schooley, W. R. Hosler and E. R. Pfeiffer. *Physical Review*, **163**, 380 (1967).

[59] N. C. Koshnick. *Nano-SQUID Susceptometry and Fluctuation Effects in Superconducting Rings*. Ph.D. thesis, Stanford University (2009).

[60] N. C. Koshnick, H. Bluhm, M. E. Huber and K. A. Moler. *Science*, **318**, 1440 (2007).

[61] J. M. Kosterlitz and D. J. Thouless. *Journal of Physics C: Solid State Physics*, **6**, 1181 (1973).

[62] Y. Kozuka, M. Kim, C. Bell, B. G. Kim, Y. Hikita and H. Y. Hwang. *Nature*, **462**, 487 (2009).

[63] L. D. Landau and E. M. Lifshitz. *Statistical Physics*, volume 5 (1980), 3rd edition.

[64] J. S. Langer and V. Ambegaokar. *Physical Review*, **164**, 498 (1967).

[65] C. N. Lau, N. Markovic, M. Bockrath, A. Bezryadin and M. Tinkham. *Physical Review Letters*, **87**, 217003 (2001).

[66] L. Li, C. Richter, J. Mannhart and R. C. Ashoori. *Nature Physics*, **7**, 762 (2011).

[67] W. A. Little. *Physical Review*, **156**, 396 (1967).

[68] B. Liu and X. Hu. *Physical Review B*, **81**, 144504 (2010).

[69] Y. Liu, K. A. McGreer, B. Nease, D. B. Haviland, G. Martinez, J. W. Halley and A. M. Goldman. *Physical Review Letters*, **67**, 2068 (1991).

[70] F. Loder, A. Kampf and T. Kopp. *arXiv:1206.1816* (2012).

[71] L. Luan, T. M. Lippman, C. W. Hicks, J. A. Bert, O. M. Auslaender, J. Chu, J. G. Analytis, I. R. Fisher and K. A. Moler. *Physical Review Letters*, **106**, 067001 (2011).

[72] J. E. Lukens and J. M. Goodkind. *Physical Review Letters*, **20**, 1363 (1968).

[73] K. A. Matveev, A. I. Larkin and L. I. Glazman. *Physical Review Letters*, **89**, 096802 (2002).

[74] D. E. McCumber and B. I. Halperin. *Physical Review B*, **1**, 1054 (1970).

[75] K. Michaeli, A. C. Potter and P. A. Lee. *Physical Review Letters*, **108**, 117003 (2012).

[76] M. Morelle, D. c. v. S. Golubović and V. V. Moshchalkov. *Physical Review B*, **70**, 144528 (2004).

[77] N. Nakagawa, H. Y. Hwang and D. A. Muller. *Nature Materials*, **5**, 204 (2006).

[78] R. S. Newbower, M. R. Beasley and M. Tinkham. *Physical Review B*, **5**, 864 (1972).

[79] A. Ohtomo and H. Y. Hwang. *Nature*, **427**, 423 (2004).

[80] J. Pearl. *Applied Physics Letters*, **5**, 65 (1964).

[81] S. Pedersen, G. R. Kofod, J. C. Hollingbery, C. B. Sørensen and P. E. Lindelof. *Physical Review B*, **64**, 104522 (2001).

[82] R. Pentcheva and W. E. Pickett. *Physical Review B*, **74**, 035112 (2006).

[83] E. Pfeiffer and J. Schooley. *Physics Letters A*, **29**, 589 (1969).

[84] V. L. Pokrovskii. *JETP Letters*, **47**, 629 (1988).

[85] Z. S. Popović, S. Satpathy and R. M. Martin. *Physical Review Letters*, **101**, 256801 (2008).

[86] R. Prozorov and R. W. Giannetta. *Superconductor Science and Technology*, **19**, R41 (2006).

[87] R. Prozorov and V. G. Kogan. *Reports on Progress in Physics*, **74**, 124505 (2011).

[88] N. Reyren, S. Gariglio, A. D. Caviglia, D. Jaccard, T. Schneider and J.-M. Triscone. *Applied Phyiscs Letters*, **94** (2009).

[89] N. Reyren, S. Thiel, A. D. Caviglia, L. F. Kourkoutis, G. Hammerl, C. Richter, C. W. Schneider, T. Kopp, A. S. Rüetschi, D. Jaccard, M. Gabay, D. A. Muller, J. M. Triscone and J. Mannhart. *Science*, **317**, 1196 (2007).

[90] T. M. Rice. *Physical Review*, **140**, A1889 (1965).

[91] T. Sakudo and H. Unoki. *Physical Review Letters*, **26**, 851 (1971).

[92] S. S. Saxena, P. Agarwal, K. Ahilan, F. M. Grosche, R. K. W. Haselwimmer, M. J. Steiner, E. Pugh, I. R. Walker, S. R. Julian, P. Monthoux, G. G. Lonzarich, A. Huxley, I. Sheikin, D. Braithwaite and J. Flouquet. *Nature*, **406**, 587 (2000).

[93] D. J. Scalapino, M. Sears and R. A. Ferrell. *Physical Review B*, **6**, 3409 (1972).

[94] D. G. Schlom and J. Mannhart. *Nature Materials*, **10**, 168 (2011).

[95] J. F. Schooley, W. R. Hosler and M. L. Cohen. *Physical Review Letters*, **12**, 474 (1964).

[96] G. Schwiete and Y. Oreg. *Physical Review Letters*, **103**, 037001 (2009).

[97] S. Seri and L. Klein. *Physical Review B*, **80**, 180410 (2009).

[98] M. Sing, G. Berner, K. Go, A. Müller, A. Ruff, A. Wetscherek, S. Thiel, J. Mannhart, S. A. Pauli, C. W. Schneider, P. R. Willmott, M. Gorgoi, F. Schäfers and R. Claessen. *Physical Review Letters*, **102**, 176805 (2009).

[99] W. Skocpol and M. Tinkham. *Reports on Progress in Physics*, **38**, 1049 (1975).

[100] F. Tafuri, J. R. Kirtley, P. G. Medaglia, P. Orgiani and G. Balestrino. *Physical Review Letters*, **92**, 157006 (2004).

[101] K. S. Takahashi, M. Gabay, D. Jaccard, K. Shibuya, T. Ohnishi, M. Lippmaa and J. Triscone. *Nature*, **441**, 195 (2006).

[102] J. Tallon, C. Bernhard, M. Bowden, P. Gilberd, T. Stoto and D. Pringle. *IEEE Transactions on Applied Superconductivity*, **9**, 1696 (1999).

[103] S. Thiel, G. Hammerl, A. Schmehl, C. W. Schneider and J. Mannhart. *Science*, **313**, 1942 (2006).

[104] M. Tinkham. *Introduction to superconductivity* (Courier Dover Publications, 2004).

[105] K. Ueno, S. Nakamura, H. Shimotani, A. Ohtomo, N. Kimura, T. Nojima, H. Aoki, Y. Iwasa and M. Kawasaki. *Nature Materials*, **7**, 855 (2008).

[106] D. Y. Vodolazov, B. J. Baelus and F. M. Peeters. *Physical Review B*, **66**, 054531 (2002).

[107] D. Y. Vodolazov, F. M. Peeters, S. V. Dubonos and A. K. Geim. *Physical Review B*, **67**, 054506 (2003).

[108] D. Y. Vodolazov, F. M. Peeters, T. T. Hongisto and K. Y. Arutyunov. *Europhysics Letters*, **75**, 315 (2006).

[109] F. von Oppen and E. K. Riedel. *Physical Review B*, **46**, 3203 (1992).

[110] R. Winkler. *Spin-orbit coupling effects in two-dimensional electron and hole systems* (Springer, Berlin; New York, 2003).

[111] X. Zhang. *SQUID Microsusceptometry of Mesoscopic Superconducting Rings*. Ph.D. thesis, University of Colorado (1996).

[112] X. Zhang and J. C. Price. *Physical Review B*, **55**, 3128 (1997).

[113] P. Zubko, S. Gariglio, M. Gabay, P. Ghosez and J. Triscone. *Annual Review of Condensed Matter Physics*, **2**, 141 (2011).